NASA Contractor Report 187126

Investigation of Advanced Counterrotation Blade Configuration Concepts for High Speed Turboprop Systems

Task 5 – Unsteady Counterrotation Ducted Propfan Analysis
Final Report

Edward J. Hall and Robert A. Delaney
Allison Gas Turbine Division of General Motors
Indianapolis, Indiana

January 1993

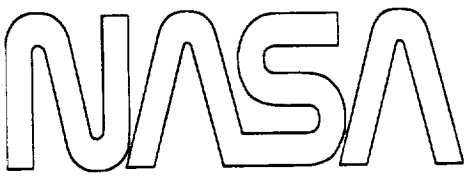

Prepared for
Lewis Research Center
Under Contract NAS3–25270

Preface

This report was prepared by Edward J. Hall and Robert A. Delaney of the Allison Gas Turbine Division, General Motors Corporation, Indianapolis, IN. The work was performed under NASA Contract NAS3-25270 from April, 1991 to September, 1992. The flow code theory, and programming modifications necessary for the aerodynamic analysis were performed by Edward J. Hall. The Allison program manager for this contract was Robert A. Delaney. The NASA project manager for this contract was Christopher J. Miller.

Acknowledgements

The authors would like to express their appreciation to the following NASA personnel who contributed to this program:

Dr. John. J. Adamczyk for the many helpful technical discussions concerning the development of the computer codes,

Dr. Christopher J. Miller for his suggestions and critical review of the program,

Dr. Andrea Arnone and Dr. Charles Swanson for their assistance during the development of the multigrid algorithm.

The services of the NASA Numerical Aerodynamic Simulation (NAS) facilities and personnel are gratefully acknowledged.

TABLE OF CONTENTS

LIST OF FIGURES

NOTATION

A list of the symbols used throughout this document and their definitions is provided below for convenience. Parameter values are shown in parentheses.

Roman Symbols

a ... speed of sound

c ... airfoil chord

c_p ... specific heat at constant pressure

c_v ... specific heat at constant volume

e ... internal energy

i ... first grid index of numerical solution

j ... second grid index of numerical solution

k ... third grid index of numerical solution or thermal conductivity

k_r ... reduced frequency $k_r = \omega c/(2V)$

l ... turbulence model damping function

n ... time step index of numerical solution or rotational speed (revolutions/sec)

$\vec{n}$ ... outward unit normal vector

p ... pressure

r ... radius or cylindrical radial coordinate

t ... time

v ... velocity

x ... first Cartesian coordinate

y ... second Cartesian coordinate

z ... cylindrical axial coordinate or third Cartesian coordinate

A ... surface area

A^+ ... turbulence model parameter

B ... number of propeller blades

C_p ... power coefficient ($C_p = P/\rho n^3 D^5$)

C_t ... thrust coefficient ($C_t = T/\rho n^2 D^4$)

C_{cp} ... turbulence model parameter

C_{kleb} ... turbulence model parameter

C_{wake} ... turbulence model parameter

D ... dissipation flux vector, turbulent damping parameter, or diameter

F ... flux vector in cylindrical coordinate z direction or turbulence model function

G ... flux vector in cylindrical coordinate r direction

H ... flux vector in cylindrical coordinate θ direction

H_t ... total enthalpy

J ... advance ratio ($J = U/nD$)

K ... source term flux vector or turbulence model parameter

L ... length

M ... Mach number

P ... power

Pr ... Prandtl number

$Pr_{turbulent}$ ... turbulent Prandtl number

Q ... vector of dependent variables

R ... gas constant or residual or maximum radius

S ... arc length or pertaining to surface area normal

T ... temperature or torque

U ... freestream velocity

V ... volume

Greek Symbols

α ... time-stepping factor

ϵ^2 ... modified second-order damping coefficient

ϵ^4 ... modified fourth-order damping coefficient

ρ ... density

κ^2 ... second-order damping coefficient

κ^4 ... fourth-order damping coefficient

γ ... specific heat ratio

δ ... spatial second-order central difference operator

λ ... blockage factor

λ_v ... second coefficient of viscosity $(= -\frac{2}{3}\mu)$

μ ... coefficient of viscosity

η ... radial transformed variable

ω ... oscillation frequency (normally radians/sec)

ξ ... axial transformed variable

ζ ... circumferential transformed variable

ν ... damping factor

Υ ... boundary layer dissipation factor

Δ ... increment of change

Special Symbols

∇ ... spatial vector gradient operator

$\triangle$ ... spatial forward difference operator $(\triangle_i \phi = \phi_{i+1} - \phi_i)$

$\bigtriangledown$ ... spatial backward difference operator $(\bigtriangledown_i \phi = \phi_i - \phi_{i-1})$

Superscripts

$[\overline{\ }]$ ... averaged variable

$[\tilde{\ }]$ ... dimensional variable

$[\hat{\ }]$ ... implicitly smoothed variable

$[\vec{\ }]$ ... vector variable

$[\ ]^*$ ... intermediate variable

$[\ ]^n$ ... time step index of variable

Subscripts

$[\ ]_{effective}$ ... effective flow value

$[\ ]_{i,j,k}$ ... grid point index of variable

$[\ ]_{laminar}$ ... laminar flow value

$[\ ]_{max}$ ... maximum value

$[\,]_{min}$ ... minimum value

$[\,]_{p}$ ... related to pressure

$[\,]_{ps}$ ... pressure (high pressure) surface

$[\,]_{ss}$ ... suction (low pressure) surface

$[\,]_{t}$ ... total quantity

$[\,]_{z}$ ... derivative or value with respect to z

$[\,]_{r}$ ... derivative or value with respect to r

$[\,]_{\theta}$ ... derivative or value with respect to θ

$[\,]_{stable}$ ... related to stability

$[\,]_{turbulent}$ ... turbulent flow value

$[\,]_{\infty}$ ... freestream value

$[\,]_{ref}$ ... reference value

$[\,]_{kleb}$ ... Klebanoff intermittency factor

$[\,]_{wake}$ ... turbulent flow wake parameter

$[\,]_{2}$ ... second-order value

$[\,]_{4}$ ... fourth-order value

ABBREVIATIONS

A list of the abbreviations used throughout this document and their definitions is provided below for convenience.

ADPAC ... Advanced Ducted Propfan Analysis Codes

AOACR ... Angle of Attack/Coupled Row aerodynamic analysis code

ASCII ... American Standard Code for Information Interchange

CFL ... Courant-Freidrichs-Levy number ($\Delta t/\Delta t_{max,stable}$)

MAKEADGRID ... *ADPAC-AOACR* multiple-block grid construction program

ROTGRID ... Ducted propfan full rotor grid construction program

SDBLIB ... Scientific DataBase Library (binary file formats)

SETUP ... *ADPAC-AOACR* Standard Configuration Setup Program

1. SUMMARY

The primary objective of this study was the development of a time-marching three-dimensional Euler/Navier-Stokes aerodynamic analysis to predict steady and unsteady compressible transonic flows about ducted and unducted propfan propulsion systems employing multiple blade rows. The computer codes resulting from this study are referred to as *ADPAC-AOACR* (Advanced Ducted Propfan Analysis Codes-Angle of Attack Coupled Row). This document is the Final Report describing the theoretical basis and analytical results from the *ADPAC-AOACR* codes developed under Task 5 of NASA Contract NAS3-25270, Unsteady Counterrotating Ducted Propfan Analysis.

The *ADPAC-AOACR* program is based on a flexible multiple blocked grid discretization scheme permitting coupled 2-D/3-D mesh block solutions with application to a wide variety of geometries. For convenience, several standard mesh block structures are described for turbomachinery applications. Aerodynamic calculations are based on a four-stage Runge-Kutta time-marching finite volume solution technique with added numerical dissipation. Steady flow predictions are accelerated by a multigrid procedure. Numerical calculations are compared with experimental data for several test cases to demonstrate the utility of this approach for predicting the aerodynamics of modern turbomachinery configurations employing multiple blade rows.

2. INTRODUCTION

Fuel efficient aircraft propulsion systems based on ultra high bypass design technologies (propfans, ducted propfans) show great promise for reducing life cycle and direct operating costs for both commercial and military transport aircraft. The integration of this technology in production aircraft requires extensive aerodynamic and structural analyses to verify and optimize designs, and to minimize the deficiencies associated with the ultra high bypass concept. Fan noise, blade flutter, and composite material behavior are examples of areas which require investigation to lend confidence to the ultra high bypass concept. In addition to the above, the overall drag due to the large diameter cowl, and potential problems associated with engine placement and mounting apparatus, may also be of significant importance. An illustration of the aerodynamic characteristics associated with the ultra high bypass propulsion concept is given in Fig. 2.1. In these cases, the fan design is typically based on relatively large, close coupled counterrotating airfoils operating in a high airflow velocity environment. Such configurations are highly susceptible to aerodynamic losses attributable to the interaction between the neighboring blade rows and/or mounting hardware, and accurate assessment of the magnitude and influence of such losses is crucial in establishing an efficient design.

Advances in individual component aerodynamic performance in aircraft gas turbine engine propulsion systems over the past decade has resulted, in part, due to the availability of improved computational fluid dynamics (CFD) aerodynamic tools for design analysis. Detailed, three-dimensional aerodynamic analyses for isolated turbomachinery blade rows have been presented by Weber and Delaney [1], and Chima [2], among others. One deficiency with the isolated blade row approach is that the interactions between adjacent blade rows in multistage turbomachinery are not properly accounted for. These interactions often lead to performance degradation through

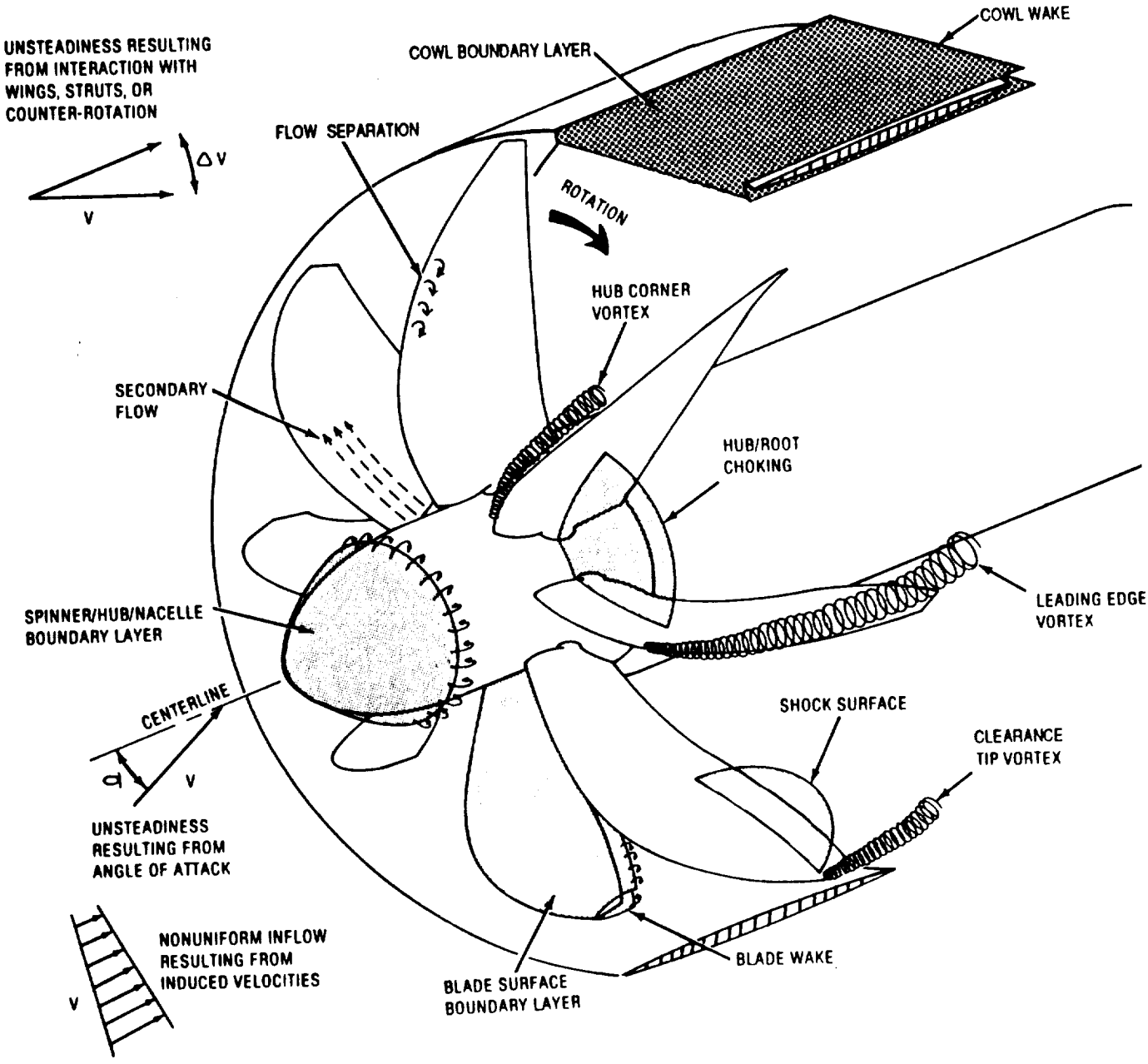

Figure 2.1: Ultra High Bypass Propulsor aerodynamic characteristics

incidence swings, hysteresis, and stage mismatching.

Historically, the prediction of three-dimensional flows through multistage turbomachinery has been based on one of three solution schemes. These schemes are briefly illustrated and described in Figure 2.2. The first scheme involves predicting the time-resolved unsteady aerodynamics resulting from the interactions occurring between relatively rotating blade rows. Examples of this type of calculation are given by Rao and Delaney [39], Jorgensen and Chima [38], and Rai [4]. This approach requires ether the simulation of multiple blade passages per blade row, or the incorporation of a phase-lagged boundary condition to account for the differences in spatial periodicity for blade rows with dissimilar blade counts. Calculations of this type are typically computationally expensive, and are presently impractical for machines with more than 2-3 blade rows.

The second solution technique is based on the average-passage equation system developed by Adamczyk [5]. In this approach, separate 3-D solution domains are defined for each blade row which encompass the overall domain for the entire turbomachine. The individual solution domains are specific to a particular blade row, although all blade row domains share a common axisymmetric flow. In the solution for the flow through a specific blade passage, adjacent blade rows are represented by their time and space-averaged blockage, body force, and energy source contributions to the overall flow. A correlation model is used to represent the time and space-averaged flow fluctuations representing the interactions between blade rows. The advantage of the average-passage approach is that the temporally and spatially averaged equation system reduce the solution to a steady flow environment; and, within the accuracy of the correlation model, the solution is representative of the average aerodynamic condition experienced by a given blade row under the influence of all other blade rows in the machine. The disadvantage of the average-passage approach is that the solution complexity and cost grow rapidly as the number of blade passages increases, and the validity of the correlation model is as yet unverified.

The third approach for the prediction of flow through multistage turbomachinery is based on the mixing plane concept. A mixing plane is an arbitrarily imposed boundary inserted between adjacent blade rows across which the flow is "mixed out" circumferentially. This circumferential mixing approximates the time-averaged condi-

Multiple Blade Row Numerical Solution Concepts

3-D Rotor/Stator Interaction

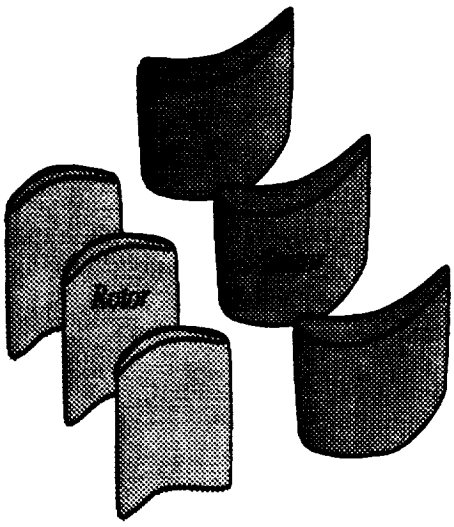

3-D time-dependent Navier-Stokes equations

Multiple blade passages for each blade row or phase-lagged boundaries

Time-dependent coupling of individual blade passage domains

Computationally expensive
Multiple blade passages per blade row

Average-Passage Simulation

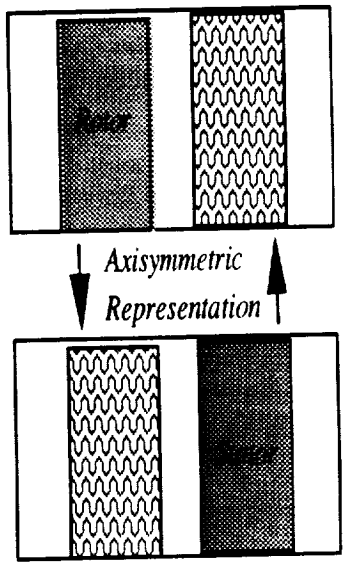

Average-passage equation system

3-D steady solution of entire domain for each blade row

Adjacent blade rows represented by blockage/body forces in 3-D solution

Solutions have common axisymmetric flowfield

Correlation model for mixing terms

Computational cost still rather high

Circumferential Mixing Plane

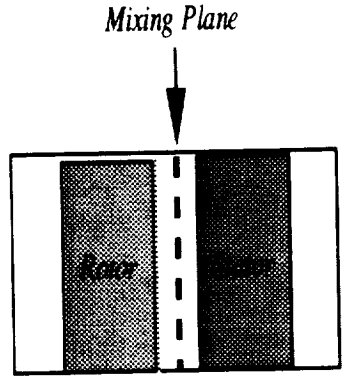

Steady Navier Stokes solution

Computational domain limited to near blade region

Circumferential mixing plane provides inter-blade row communication

Lower computational cost

Figure 2.2: Computational Schemes for Multiple Blade Row Turbomachinery

tion at the mixing plane and allows the aerodynamic solution for each blade passage to be performed in a steady flow environment. The mixing plane concept was recently applied to realistic turbofan engine configurations by Goyal and Dawes [6]. Flow variables on either side of the mixing plane are circumferentially averaged and passed to the neighboring blade row as a means of smearing out the circumferential nonuniformities resulting from dissimilar blade counts. The mixing plane concept is a much more cost-effective approach computationally because the flow is steady, and the individual blade passage domains are limited to a near-blade region. Unfortunately, the accuracy of this approach is clearly questionable under some circumstances because of the placement of the mixing plane and the loss of spatial information resulting from the circumferential averaging operator. For example, consider a flow field with a region of concentrated axial vorticity (such as that resulting from a tip leakage vortex). Application of the circumferential averaging operator would remove the local structure of the vortex in favor of a circumferentially smeared flowfield with equivalant global properties, resulting in a loss of information concerning the structure of the leakage vortex.

This document contains the Final Report for the *ADPAC-AOACR* (Advanced Ducted Propfan Analysis Codes - Angle of Attack/Coupled Row) 3D Euler/Navier-Stokes aerodynamic analysis developed by the Allison Gas Turbine Division of the General Motors Corporation under Task V of NASA Contract NAS3-25270. The primary objective behind this study was the development of a computational method to accurately assess the aerodynamic characteristics of high bypass turbofan engine designs employing multiple blade rows. The motivation behind this objective lies in the performance potential offered by high bypass ratio turbofan engine designs, and the observed effects of aerodynamic interaction occurring between relatively rotating adjacent blade rows.

The *ADPAC-AOACR* program possesses many features which permit multiple blade row solutions using either the time-dependent interaction approach or the mixing plane concept described above. Average-passage simulations for realistic turbofan engine configurations were recently reported under Task 4 of this contract, and further details on this approach can be found in Reference [8].

The *ADPAC-AOACR* program is based on an explicit Runge-Kutta time-marching algorithm employing a finite volume, multiple blocked grid discretization. The code is constructed such that the algorithm may be applied to multiple blocked grid mesh systems with common grid interface (non-overlapping) boundaries. (For a description of multiple-blocked mesh solution schemes, see Section 3.4.) Several convergence enhancements are added for the prediction of steady state flows including local time stepping, implicit residual smoothing, and multigrid (See Chapter 3 for further details).

A systematic approach to utilize the *ADPAC-AOACR* code for the analysis of ducted and unducted fan propulsion systems was derived by developing a series of standard blocked mesh configurations for various analytical problems of interest. These standard configurations are discussed in detail in the companion report describing the actual code operation (Computer Program Users Manual) [9]. Several of the standard configurations are demonstrated and verified in the discussion of results given in Chapter 4.0.

Separate sections are provided in the chapters which follow to describe the theoretical basis of the *ADPAC-AOACR* code, and summarize the predicted results and verification studies performed to validate the accuracy of the analysis.

It is worthwhile mentioning that the development and application of the codes described in this manual were performed on UNIX-based computers. All files are stored in machine-independent format. Small files utilize standard ASCII format, while larger files, which benefit from some type of binary storage, are written in a machine-independent format through the Scientific DataBase Library (SDBLIB) routines [24] The SDBLIB format utilizes machine-dependent input/output routines which permit machine independence of the binary data file. The SDBLIB routines are under development at the NASA Lewis Research Center.

Most of the plotting and graphical postprocessing of the solutions was performed on graphics workstations. Presently, the *PLOT3D* [25], *SURF* [26], and *FAST* [27] graphics software packages developed at the NASA Ames Research Center are being extensively used for this purpose, and plot output has been tailored for this software. In addition, due to the increasing popularity of the *PostScript* page description lan-

guage, and the variety of devices which can display *PostScript*-based output, a number of plotting procedures included in the *ADPAC* package utilize standard *PostScript* routines.

3. 3D EULER/NAVIER-STOKES NUMERICAL ALGORITHM

In this chapter, the mathematical and computational basis for the *ADPAC-AOACR* time-dependent multiple-grid block Euler/Navier-Stokes analysis is described. The definitions of the pertinent variables used in this chapter may be found in the Nomenclature.

3.1 Nondimensionalization

To simplify the implementation of the numerical solution, all variables are nondimensionalized by reference values as follows:

$$z = \frac{\tilde{z}}{L_{ref}}, \quad r = \frac{\tilde{r}}{L_{ref}}, \quad v_z = \frac{\tilde{v}_z}{v_{ref}}, \quad v_r = \frac{\tilde{v}_r}{v_{ref}}, \quad v_\theta = \frac{\tilde{v}_\theta}{v_{ref}}$$

$$p = \frac{\tilde{p}}{p_{ref}}, \quad \mu = \frac{\tilde{\mu}}{\mu_{ref}}, \quad cp = \frac{\tilde{c}p}{R_{ref}}, \quad cv = \frac{\tilde{c}v}{R_{ref}}, \quad k = \frac{\tilde{k}}{k_{ref}}$$

$$T = \frac{\tilde{T}}{T_{ref}}, \quad \rho = \frac{\tilde{\rho}}{\rho_{ref}}, \quad \omega = \frac{\tilde{\omega} L_{ref}}{v_{ref}} \tag{3.1}$$

The reference quantities are defined as follows:

L_{ref} is the maximum diameter of the propfan blade

p_{ref} is the freestream total pressure

ρ_{ref} is the freestream total density

a_{ref} is determined from the freestream total conditions
$= \sqrt{\gamma p_{ref}/\rho_{ref}}$

v_{ref} is determined from the freestream total acoustic velocity as

$$v_{ref} = \frac{a_{ref}}{\sqrt{\gamma}}$$

μ_{ref} is determined from the other factors as:

$$\mu_{ref} = \rho_{ref} v_{ref} L_{ref}$$

k_{ref} is the freestream thermal conductivity

R_{ref} is the freestream gas constant

T_{ref} is the freestream total temperature

3.2 3-D Navier-Stokes Equations

The numerical solution procedure is based on an integral representation of the strong conservation law form of the Navier-Stokes equations expressed in a cylindrical coordinate system. The Euler equations may be derived as a subset of the Navier-Stokes equations by neglecting viscous dissipation and thermal conductivity terms (i.e. - μ and $k = 0$).

Integration of the differential form of the Navier-Stokes equations over a rotating finite control volume yields the following equation:

$$\int \frac{\partial}{\partial t}(Q)dV + L_{inv}(Q) = \int K dV + L_{vis}(Q) \tag{3.2}$$

where:

$$L_{inv}(Q) = \int_{dA} \left[\bar{F}_{inv} dA_z + \bar{G}_{inv} dA_r + (\bar{H}_{inv} - r\omega\bar{Q}) dA_\theta\right] \tag{3.3}$$

and:

$$L_{vis}(Q) = \int_{dA} \left[\bar{F}_{vis} dA_z + \bar{G}_{vis} dA_r + \bar{H}_{vis} dA_\theta\right] \tag{3.4}$$

The inviscid (convective) and viscous (diffusive) flux contributions are expressed separately by the operators L_{inv} and L_{vis}, respectively.

The vector of dependent variables Q is defined as:

$$Q = \begin{bmatrix} \rho \\ \rho v_z \\ \rho v_r \\ \rho v_\theta \\ \rho e_t \end{bmatrix} \tag{3.5}$$

where the velocity components v_z, v_r, and v_θ are the absolute velocity components in the axial, radial, and circumferential directions relative to the cylindrical coordinate system, respectively (see e.g. - Fig. 3.1). The total internal energy is defined as:

$$e_t = \frac{p}{(\gamma - 1)\rho} + \frac{1}{2}(v_z^2 + v_r^2 + v_\theta^2) \tag{3.6}$$

The individual flux functions are defined as:

$$F_{inv} = \begin{bmatrix} \rho v_z \\ \rho v_z^2 + p \\ \rho v_z v_r \\ \rho v_z v_\theta \\ \rho v_z H \end{bmatrix}, \quad G_{inv} = \begin{bmatrix} \rho v_r \\ \rho v_z v_r \\ \rho v_r^2 + p \\ \rho v_r v_\theta \\ \rho v_r H \end{bmatrix}, \quad H_{inv} = \begin{bmatrix} \rho v_\theta \\ \rho v_z v_\theta \\ \rho v_r v_\theta \\ (\rho v_\theta^2 + p) \\ \rho v_\theta H \end{bmatrix} \tag{3.7}$$

$$F_{vis} = \begin{bmatrix} 0 \\ \tau_{zz} \\ \tau_{zr} \\ \tau_{z\theta} \\ q_z \end{bmatrix}, \quad G_{vis} = \begin{bmatrix} 0 \\ \tau_{rz} \\ \tau_{rr} \\ \tau_{r\theta} \\ q_r \end{bmatrix}, \quad H_{vis} = \begin{bmatrix} 0 \\ \tau_{\theta z} \\ \tau_{\theta r} \\ \tau_{\theta\theta} \\ q_\theta \end{bmatrix}, \tag{3.8}$$

$$\bar{F} = F(\bar{Q}), \qquad \bar{G} = G(\bar{Q}), \qquad \bar{H} = H(\bar{Q})$$

$$\bar{F}_v = F_v(\bar{Q}), \qquad \bar{G}_v = G_v(\bar{Q}), \qquad \bar{H}_v = H_v(\bar{Q}) \tag{3.9}$$

ADPAC–AOACR Coordinate System Reference

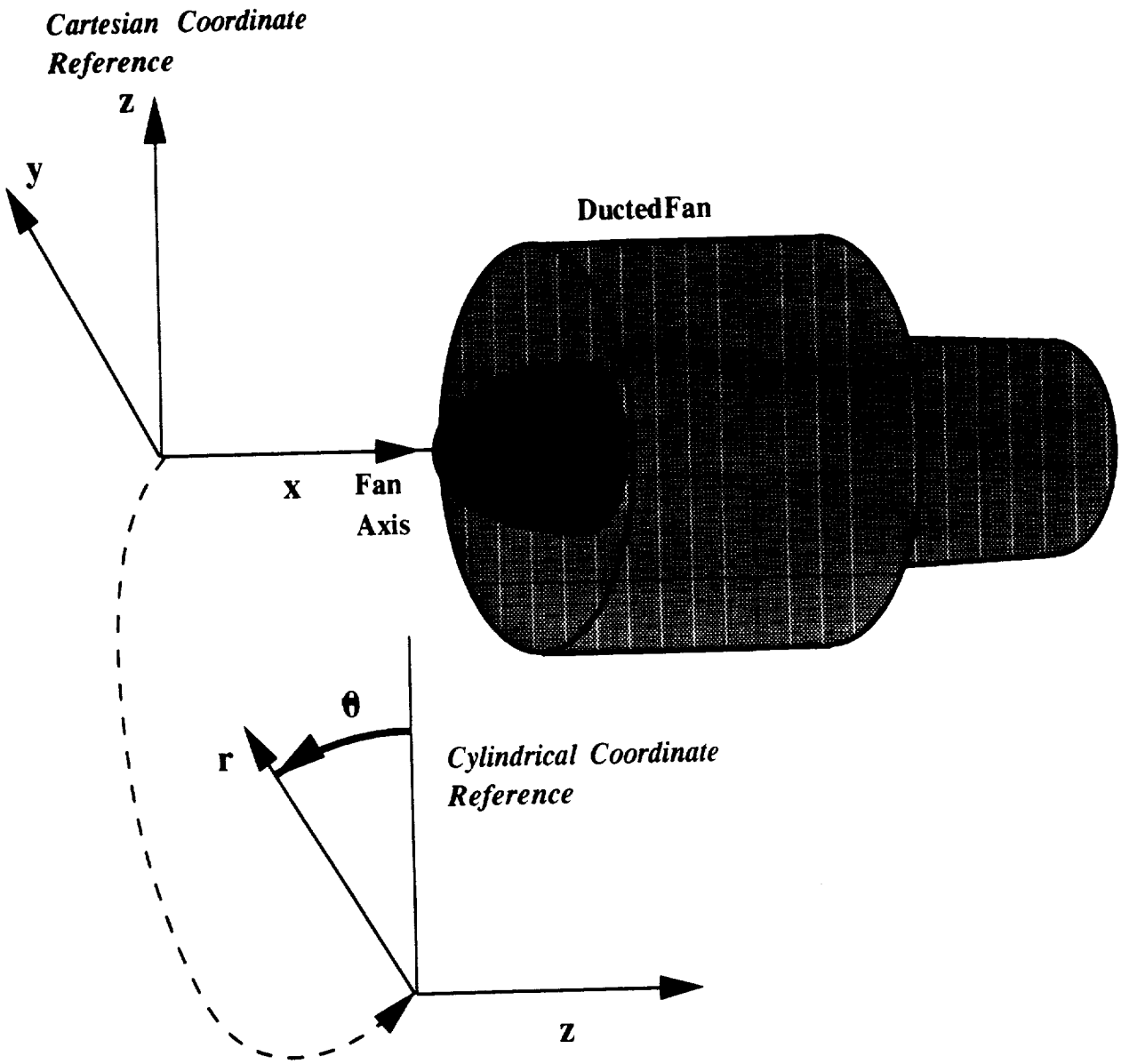

Figure 3.1: *ADPAC-AOACR* Cylindrical Coordinate System Reference

Finally, the cylindrical coordinate system source term is:

$$K = \begin{bmatrix} 0 \\ 0 \\ \frac{\rho v_\theta^2 + p}{r} - \tau_{\theta\theta} \\ 0 \\ 0 \end{bmatrix} \tag{3.10}$$

It should be noted that in the numerical algorithm, the radius used in the cylindrical source term K must be carefully formulated to guarantee numerical conservation for the radial momentum equation. That is, for a uniform flow, the radius in the radial momentum equation is chosen such that both sides of the radial momentum equation are equal. This ensures that small geometric errors do not corrupt the conservative nature of the numerical scheme. The total enthalpy, H, is related to the total energy by:

$$H = e_t + \frac{p}{\rho} \tag{3.11}$$

The viscous stress terms may be expressed as:

$$\tau_{zz} = 2\mu \left(\frac{\partial v_z}{\partial z} \right) + \lambda_v \nabla \cdot \vec{V}, \tag{3.12}$$

$$\tau_{zr} = \mu \left[\left(\frac{\partial v_r}{\partial z} \right) + \left(\frac{\partial v_z}{\partial r} \right) \right], \tag{3.13}$$

$$\tau_{z\theta} = 2\mu \left[\left(\frac{1}{r} \frac{\partial v_r}{\partial \theta} \right) + \left(\frac{\partial v_\theta}{\partial z} \right) \right], \tag{3.14}$$

$$\tau_{rr} = 2\mu \left(\frac{\partial v_r}{\partial r} \right) + \lambda_v \nabla \cdot \vec{V}, \tag{3.15}$$

$$\tau_{r\theta} = 2\mu \left[\left(\frac{1}{r} \frac{\partial v_r}{\partial z} \right) + \left(\frac{\partial v_\theta}{\partial r} \right) - \left(\frac{v_\theta}{r} \right) \right], \tag{3.16}$$

$$\tau_{\theta\theta} = 2\mu \left(\frac{1}{r} \frac{\partial v_\theta}{\partial \theta} + \frac{\partial v_r}{r} \right) + \lambda_v \nabla \cdot \vec{V}, \tag{3.17}$$

$$q_z = v_z \tau_{zz} + v_r \tau_{zr} + v_\theta \tau_{z\theta} + k \frac{\partial T}{\partial z}, \tag{3.18}$$

$$q_r = v_z \tau_{rz} + v_r \tau_{rr} + v_\theta \tau_{r\theta} + k \frac{\partial T}{\partial r}, \tag{3.19}$$

$$q_\theta = v_z \tau_{\theta z} + v_r \tau_{\theta r} + v_\theta \tau_{\theta\theta} + k \frac{\partial T}{\partial \theta}, \tag{3.20}$$

where μ is the first coefficient of viscosity, λ_v is the second coefficient of viscosity, and:

$$\nabla \cdot \vec{V} = \frac{\partial u_z}{\partial z} + \frac{\partial u_r}{\partial r} + \frac{1}{r}\frac{\partial u_\theta}{\partial \theta} + \frac{u_r}{r} \tag{3.21}$$

The remaining viscous stress terms are defined through the identities:

$$\tau_{rz} = \tau_{zr}, \tag{3.22}$$

$$\tau_{\theta r} = \tau_{r\theta}, \tag{3.23}$$

$$\tau_{\theta z} = \tau_{z\theta}, \tag{3.24}$$

3.3 2-D Navier-Stokes Equations with Embedded Blade Row Body Forces

In order to permit a simplified analysis of two-dimensional flows in axisymmetric passages with turbomachinery blade rows, a reduced (axisymmetric) form of the 3-D Navier-Stokes equations given in the previous section is derived for 2-D flows with embedded blade rows represented by axisymmetric blockage and body forces.

Integration of the differential form of the Navier-Stokes equations for an axisymmetric flow yields the following equations:

$$\int \frac{\partial}{\partial t}(\lambda Q) dV + L_{inv}(\lambda Q) = \int \lambda S dV + \int \lambda K dV + L_{vis}(\lambda Q) \tag{3.25}$$

where:

$$L_{inv}(\lambda Q) = \int_{dA} \left[\lambda \bar{F}_{inv} dA_z + \lambda \bar{G}_{inv} dA_r \right] \tag{3.26}$$

and:

$$L_{vis}(\lambda Q) = \int_{dA} \left[\lambda \bar{F}_{vis} dA_z + \lambda \bar{G}_{vis} dA_r \right] \tag{3.27}$$

The term λ represents a circumferential blockage factor the value of which may range from 0.0 to 1.0. This factor represents the relative circumferential blockage imposed by the thickness of the embedded blade row and is calculated as

$$\lambda = 1.0 - \frac{\Delta\theta_{blade}}{\frac{2\pi}{N}} \tag{3.28}$$

The inviscid (convective) and viscous (diffusive) flux contributions have been expressed separately by the operators L_{inv} and L_{vis}, respectively.

The vector of dependent variables Q is again defined as:

$$Q = \begin{bmatrix} \rho \\ \rho v_z \\ \rho v_r \\ \rho v_\theta \\ \rho e_t \end{bmatrix} \tag{3.29}$$

where the velocity components v_z, v_r, and v_θ are the absolute velocity components in the axial, radial, and circumferential directions relative to the cylindrical coordinate system, respectively (see e.g. - Fig. 3.1). The total internal energy is defined as:

$$e_t = \frac{p}{(\gamma - 1)\rho} + \frac{1}{2}(v_z^2 + v_r^2 + v_\theta^2) \tag{3.30}$$

The vector S contains the body forces and energy sources associated with the axisymmetric influence of an embedded blade row.

The individual flux functions and viscous stresses are as defined in the previous section.

The similarity between the 3-D Navier-Stokes equations and the 2-D axisymmetric equations described here is obvious. As a result, the numerical implementation of each scheme (described in the next section) is essentially the same, and in most cases, unless a specific requirement for the 2-D scheme must be described, only the 3-D numerical scheme details are given.

3.4 Numerical Formulation

The discrete numerical solution is developed from the integral governing equations derived in the previous two sections by employing a finite volume solution procedure. This procedure closely follows the basic scheme described by Jameson [35]. In order to appreciate and utilize the features of the *ADPAC-AOACR* solution system, the concept of a multiple blocked grid system must be fully understood. It is expected that the reader possesses at least some understanding of the concepts of computational fluid dynamics (CFD), so the use of a numerical grid to discretize a flow domain should not be foreign. Many CFD analyses rely on a single structured ordering of grid points upon which the numerical solution is performed (the authors are aware of a growing number of unstructured grid solution techniques as well, but resist the temptation to mention them in this discussion). Multiple blocked grid systems are different only in that several structured grid systems are used in harmony to generate the numerical solution. The domain of interest is subdivided into one or more structured arrays of hexahedral cells. Each array of cells is referred to as a "block", and the overall scheme is referred to as a multiple blocked mesh solver as a result of the ability to manage more than one block. This concept is illustrated graphically in two dimensions for the flow through a nozzle in Figures 3.2-3.4.

The grid system in Figure 3.2 employs a single structured ordering, resulting in a single computational space to contend with. The mesh system in Figure 3.3 is comprised of two, separate structured grid blocks, and consequently, the numerical solution consists of two unique computational domains. In theory, the nozzle flowpath could be subdivided into any number of domains employing structured grid blocks resulting in an identical number of computational domains to contend with, as shown in the 20 block decomposition illustrated in Figure 3.4. The complicating factor in this domain decomposition approach is that the numerical solution must provide a means for the isolated computational domains to communicate with each other in order to satisfy the conservation laws governing the desired aerodynamic solution. Hence, as the number of subdomains used to complete the aerodynamic solution grows larger, the number of inter-domain communication paths increases in a corresponding manner. (It should be noted that this domain decomposition/communication overhead

ADPAC–AOACR 2–D Single Block Mesh Structure Illustration

Physical Domain

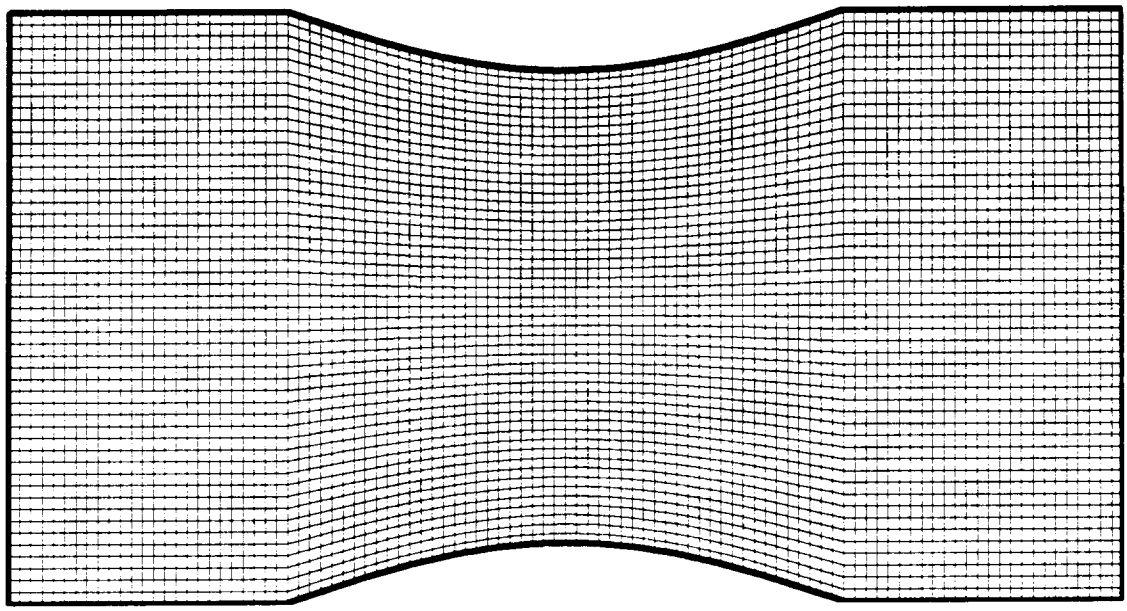

Computational Domain

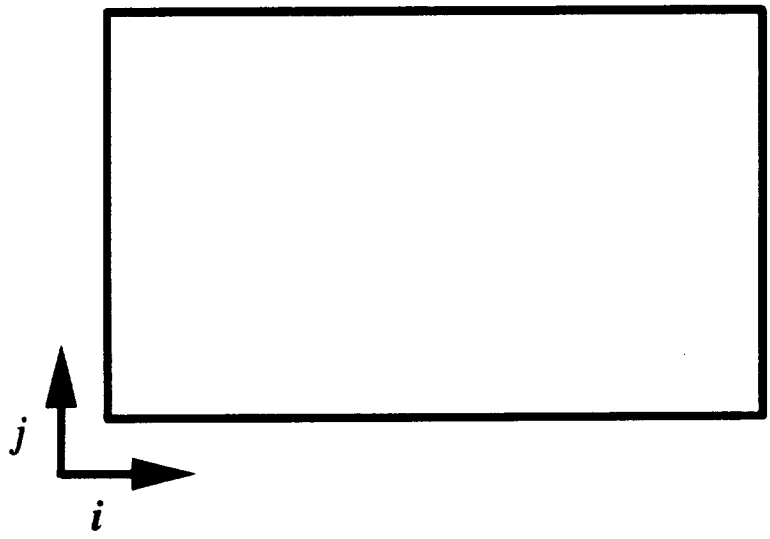

Figure 3.2: *ADPAC-AOACR* 2-D Single Block Mesh Structure Illustration

ADPAC–AOACR 2–D Two Block Mesh Structure Illustration

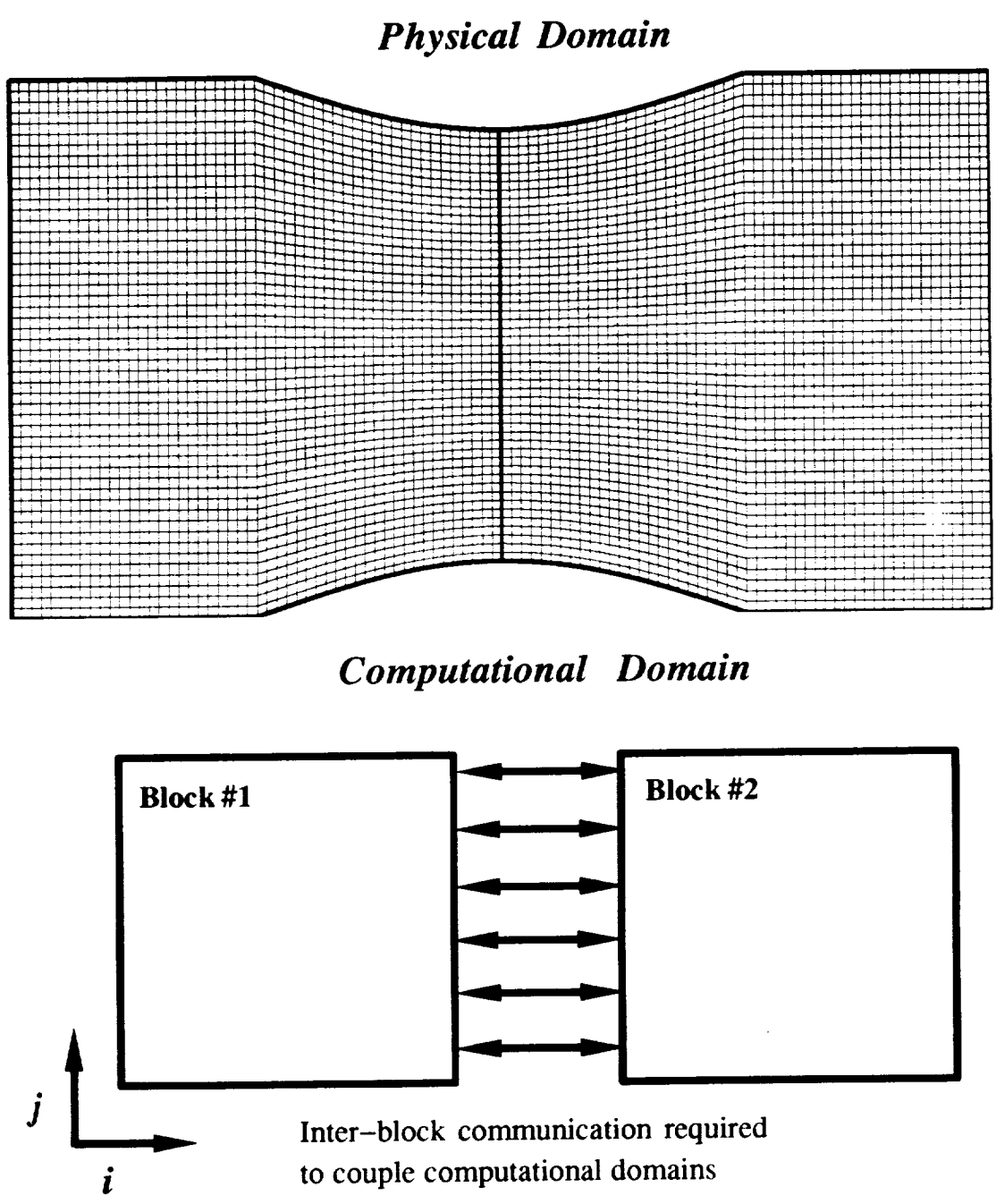

Figure 3.3: *ADPAC-AOACR* 2-D Two Block Mesh Structure Illustration

ADPAC–AOACR 2–D Multiple Block Mesh Structure Illustration

Physical Domain

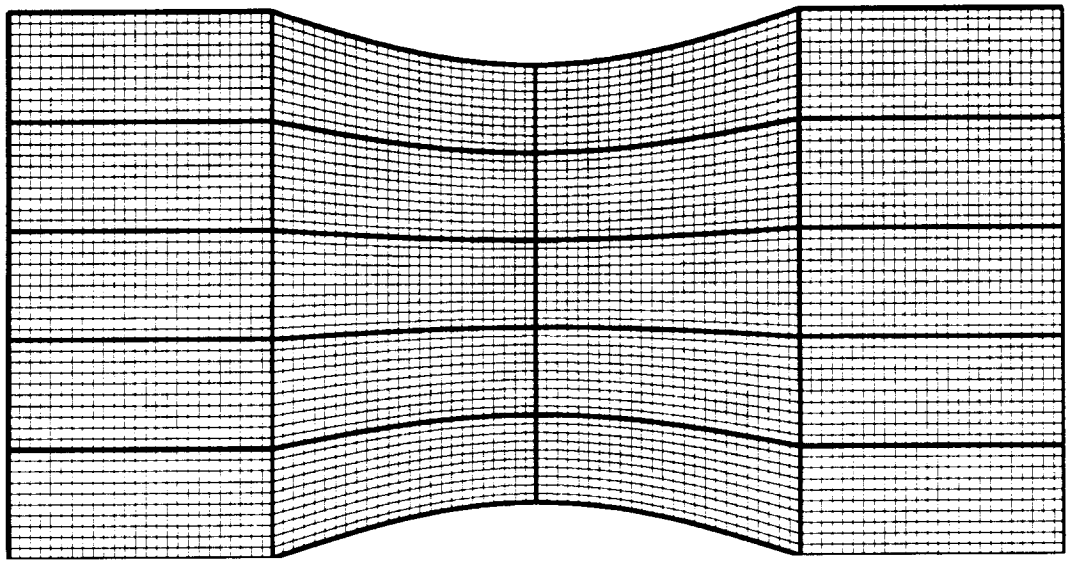

Computational Domain

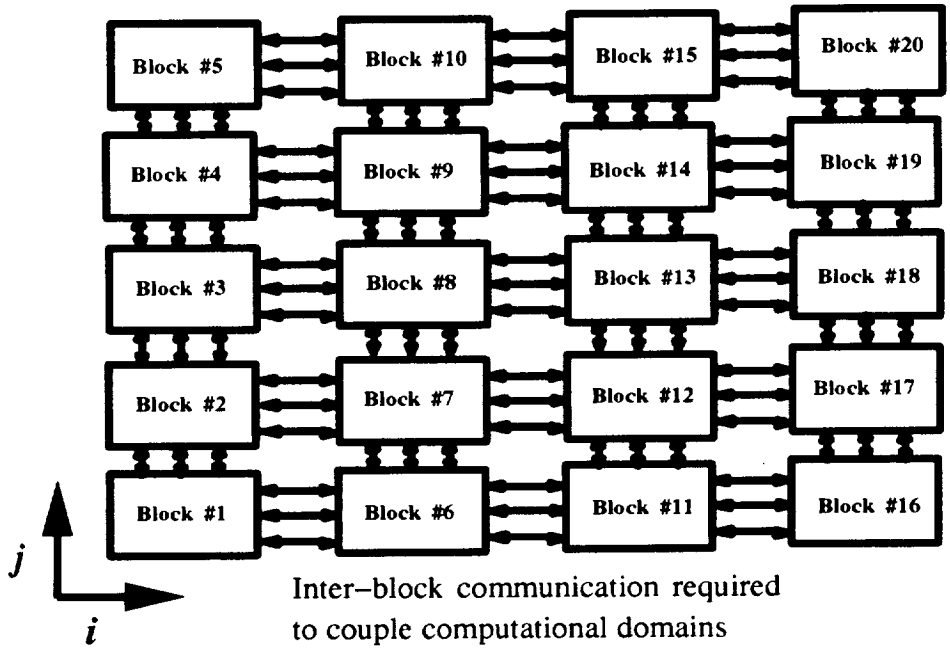

Figure 3.4: *ADPAC-AOACR* 2-D Multiple Block Mesh Structure Illustration

relationship is also a key concept in parallel processing for large scale computations, and thus, the *ADPAC-AOACR* code appears to be a viable candidate for parallelization via the natural domain decomposition division afforded by the multiple-blocked grid data structure.) Clearly, it is often not possible to generate a single structured grid to encompass the domain of interest without sacrificing grid quality, and therefore, a multiple blocked grid system has significant advantages.

The *ADPAC-AOACR* code was developed to utilize the multiple blocked grid concept to full extent by permitting an arbitrary number of structured grid blocks with user specifiable communication paths between blocks. The inter-block communication paths are implemented as a series of boundary conditions on each block which, in some cases, communicate flow information from one block to another. The advantages of the multiple-block solution concept are exploited in the calculations presented in Chapter 4 as a means of treating complicated geometries with multiple blade rows of varying blade number, and to exploit computational enhancements such as multigrid.

The solution for each mesh block in a multiple-blocked grid is computed identically, and therefore the numerical approach is described for a single mesh block. In any given mesh block, the numerical grid is used to define a set of hexahedral cells, the vertices of which are defined by the eight surrounding mesh points. This construction is illustrated in Figure 3.5.

The cell face surface area normal vector components dA_z, dA_r, and dA_θ are calculated using the cross product of the diagonals defined by the four vertices of the given face, and the cell volume is determined by a procedure outlined by Hung and Kordulla [33] for generalized nonorthogonal cells. The integral relations expressed by the governing equations are determined for each cell by approximating the area-integrated convective and diffusive fluxes with a representative value along each cell face, and by approximating the volume-integrated terms with a representative cell volume weighted value. The discrete numerical approximation to the governing equation then becomes

$$Vol\frac{Q^{n+1}_{i,j,k} - Q^{n}_{i,j,k}}{\Delta t} = (F_{inv}(\bar{Q})_{i+1,j,k} - F_{inv}(\bar{Q})_{i,j,k} \tag{3.31}$$

$$+G_{inv}(\bar{Q})_{i,j+1,k} - G_{inv}(\bar{Q})_{i,j,k}$$

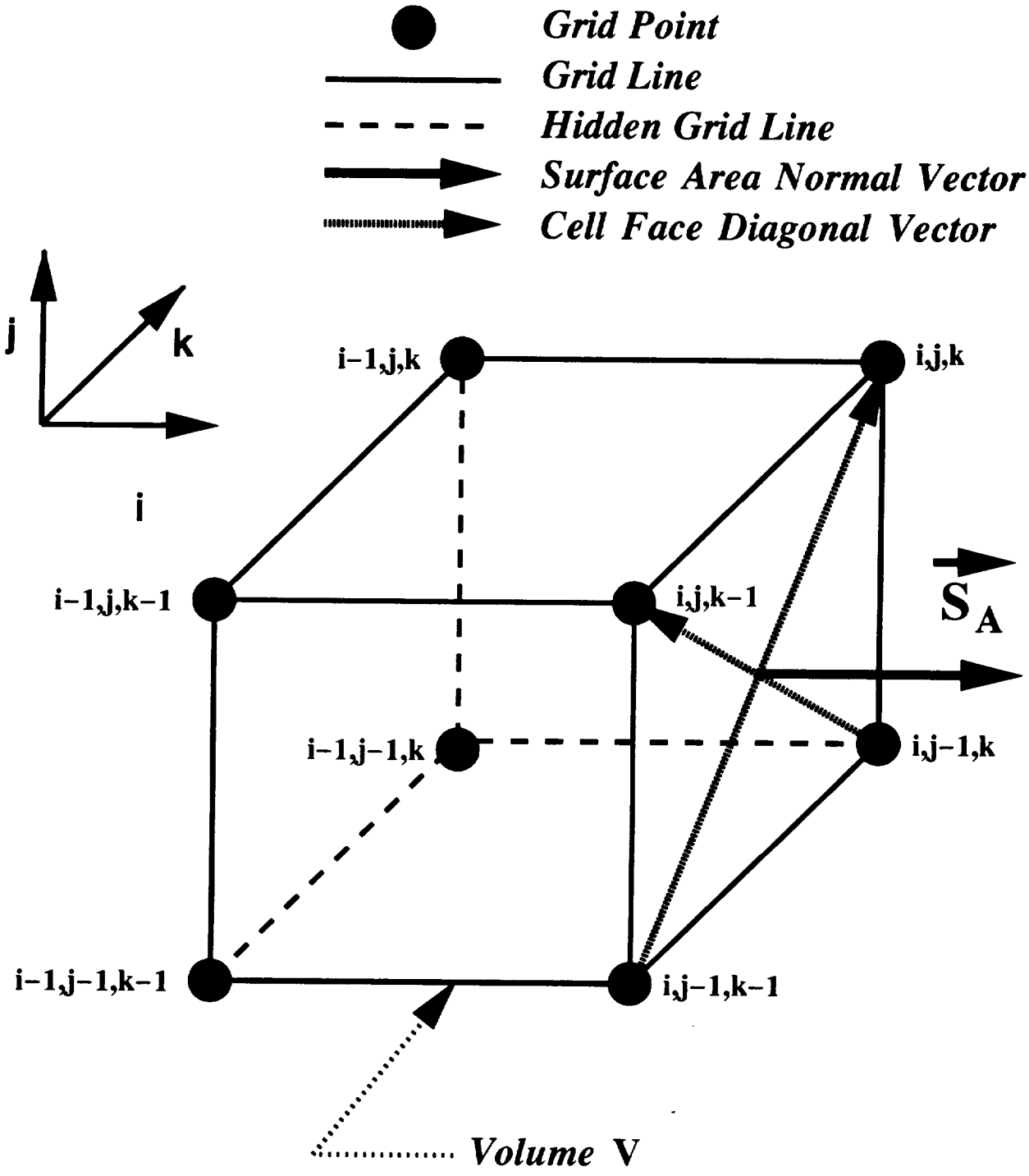

Figure 3.5: Three-dimensional finite volume cell

$$
\begin{aligned}
&+H_{inv}(\bar{Q})_{i,j,k+1} - H_{inv}(\bar{Q})_{i,j,k} \\
&+F_{vis}(\bar{Q})_{i+1,j,k} - F_{vis}(\bar{Q})_{i,j,k} \\
&+G_{vis}(\bar{Q})_{i,j+1,k} - G_{vis}(\bar{Q})_{i,j,k} \\
&+H_{vis}(\bar{Q})_{i,j,k+1} - H_{vis}(\bar{Q})_{i,j,k}) \\
&+VolK + D_{i,j,k}(\bar{Q})
\end{aligned}
$$

Here, i, j, k represents the local cell indices in the structured cell array, Vol is the local cell volume, Δt is the calculation time interval, and $D_{i,j,k}$ is an artificial numerical dissipation function which is added to the governing equations to aid numerical stability, and to eliminate spurious numerical oscillations in the vicinity of flow discontinuities such as shock waves. Following the algorithm defined by Jameson [35], it is convenient to store the flow variables as a representative value for the interior of each cell, and thus the scheme is referred to as cell-centered. The discrete convective fluxes are constructed by using a representative value of the flow variables $\bar{Q}$ which is determined by an algebraic average of the values of Q in the cells lying on either side of the local cell face. Viscous stress terms and thermal conduction terms are constructed by applying a generalized coordinate transformation to the governing equations as follows:

$$
\xi = \xi(z, r, \theta), \qquad \eta = \eta(z, r, \theta), \qquad \zeta = \zeta(z, r, \theta) \tag{3.32}
$$

The chain rule may then be used to expand the various derivatives in the viscous stresses as:

$$
\frac{\partial}{\partial x} = \frac{\partial \xi}{\partial x}\frac{\partial}{\partial \xi} + \frac{\partial \eta}{\partial x}\frac{\partial}{\partial \eta} + \frac{\partial \zeta}{\partial x}\frac{\partial}{\partial \zeta}, \tag{3.33}
$$

$$
\frac{\partial}{\partial r} = \frac{\partial \xi}{\partial r}\frac{\partial}{\partial \xi} + \frac{\partial \eta}{\partial r}\frac{\partial}{\partial \eta} + \frac{\partial \zeta}{\partial r}\frac{\partial}{\partial \zeta}, \tag{3.34}
$$

$$
\frac{\partial}{\partial \theta} = \frac{\partial \xi}{\partial \theta}\frac{\partial}{\partial \xi} + \frac{\partial \eta}{\partial \theta}\frac{\partial}{\partial \eta} + \frac{\partial \zeta}{\partial \theta}\frac{\partial}{\partial \zeta}, \tag{3.35}
$$

The transformed derivatives may now be easily calculated by differencing the variables in computational space (i corresponds to the ξ direction, j corresponds to the η direction, and k corresponds to the ζ direction), and utilizing the appropriate identities for the metric differences (see e.g. [32]).

3.5 Runge-Kutta Time Integration

The time-stepping scheme used to advance the discrete numerical representation of the governing equations is a multistage Runge-Kutta integration. An m stage Runge-Kutta integration for the discretized equations is expressed as:

$$Q_1 = Q^n - \alpha_1 \Delta t[L(Q^n) + D(Q^n)],$$

$$Q_2 = Q^n - \alpha_2 \Delta t[L(Q_1) + D(Q^n)],$$

$$Q_3 = Q^n - \alpha_3 \Delta t[L(Q_2) + D(Q^n)],$$

$$Q_4 = Q^n - \alpha_4 \Delta t[L(Q_3) + D(Q^n)],$$

....

....

$$Q_m = Q^n - \alpha_m \Delta t[L(Q_{m-1}) + D(Q^n)],$$

$$Q^{n+1} = Q_m \tag{3.36}$$

where:

$$L(Q) = L_{inv}(Q) - L_{vis}(Q) \tag{3.37}$$

For simplicity, viscous flux contributions to the discretized equations are only calculated for the first stage, and the values are frozen for the remaining stages. This reduces the overall computational effort and does not appear to significantly alter the solution for unsteady flows (there is no difference for steady state flows). It is also generally not necessary to recompute the added numerical dissipation terms during each stage. In this study, three different multistage Runge-Kutta schemes (2 four-stage schemes, and 1 five-stage scheme) were investigated. The differences between the schemes will be described in more detail in a later section.

A linear stability analysis of the four and five-stage Runge-Kutta time-stepping schemes utilized during this study indicate that the schemes are stable for all calculation time increments δt which satisfy the stability criteria $CFL \leq 2\sqrt{2}$ (four stage)

or $CFL \leq 3.75$ (five stage). Based on convection constraints alone, the CFL number may be defined in a one-dimensional manner as:

$$CFL = \frac{\Delta t}{\frac{|u|+a}{\Delta z}} \tag{3.38}$$

In practice, the calculation time interval must also include restrictions resulting from diffusion phenomena. The time step used in the numerical calculation results from both convective and diffusive considerations and is calculated as:

$$\Delta t = CFL \left(\frac{1.0}{\lambda_i + \lambda_j + \lambda_k + \nu_i + \nu_j + \nu_k} \right) \tag{3.39}$$

where the convective and diffusive coordinate wave speeds (λ and ν, repsectively) are defined as:

$$\lambda_i = Vol/(\vec{V} \cdot \vec{S}_i + a) \tag{3.40}$$

$$\nu_i = \frac{\rho Vol^2}{C_{\Delta t}(S^2)\mu} \tag{3.41}$$

The factor $C_{\Delta t}$ is a "safety factor" of sorts, which must be imposed as a result of the limitations of the linear stability constraints for a set of equations which are truly nonlinear. This factor was determined through numerical experimentation and is normally chosen to be 4.0.

For steady state flow calculations, an acceleration technique known as local time stepping is used to enhance convergence to the steady-state solution. Local time stepping utilizes the maximum allowable time increment at each point during the course of the solution. While this destroys the physical nature of the transient solution, the steady-state solution is unaffected and can be obtained in fewer iterations of the time-stepping scheme. For unsteady flow calculations, of course, a uniform value of the time step Δt must be used at every grid point to maintain the time-accuracy of the solution. Other convergence enhancements such as implicit residual smoothing and multigrid (described in later sections) are also applied for steady flow calculations.

3.6 Fluid Properties

The working fluid is assumed to be air acting as a perfect gas, thus the ideal gas equation of state has been used. Fluid properties such as specific heats, specific heat ratio, and Prandtl number are assumed to be constant. The fluid viscosity is either specified as a constant, or derived from the Sutherland (see e.g. [32]) formula:

$$\mu = C_1 \frac{(T)^{\frac{3}{2}}}{T + C_2} \tag{3.42}$$

The so-called second coefficient of viscosity λ_v is fixed according to:

$$\lambda_v = -\frac{2}{3}\mu \tag{3.43}$$

The thermal conductivity is determined from the viscosity and the definition of the Prandtl number as:

$$k = \frac{cp\mu}{Pr} \tag{3.44}$$

3.7 Dissipation Function

In order to prevent odd-even decoupling of the numerical solution, nonphysical oscillations near shock waves, and to obtain rapid convergence for steady state solutions, artificial dissipative terms are added to the discrete numerical representation of the governing equations. The added dissipation model is based on the combined works of Jameson et al. [35], Martinelli [10], and Swanson et al. [36]. A blend of fourth and second differences is used to provide a third order background dissipation in smooth flow regions and first order dissipation near discontinuities. The discrete equation dissipative function is given by:

$$D_{i,j,k}(Q) = (D_i^2 - D_i^4 + D_j^2 - D_j^4 + D_k^2 - D_k^4)Q_{i,j,k} \tag{3.45}$$

The second and fourth order dissipation operators are determined by

$$D_\xi^2 Q_{i,j,k} = \nabla_\xi((\bar{\lambda}_\xi)_{i+\frac{1}{2}} \epsilon^2_{i+\frac{1}{2},j,k}) \triangle_\xi Q_{i,j,k} \tag{3.46}$$

$$D_\xi^4 Q_{i,j,k} = \nabla_\xi((\bar{\lambda}_\xi)_{i+\frac{1}{2}} \epsilon^4_{i+\frac{1}{2},j,k}) \triangle_\xi \nabla_\xi \triangle_\xi Q_{i,j,k} \tag{3.47}$$

where $\triangle_\xi$ and ∇_ξ are forward and backward difference operators in the ξ direction. In order to avoid excessively large levels of dissipation for cells with large aspect ratios, and to maintain the damping properties of the scheme, a variable scaling of the dissipative terms is employed which is an extension of the two dimensional scheme given by Martinelli [10]. The scaling factor is defined as a function of the spectral radius of the Jacobian matrices associated with the ξ, η, and ζ directions and provides a scaling mechanism for varying cell aspect ratios through the following scheme:

$$(\bar{\lambda}_\xi)_{i+\frac{1}{2},j,k} = (\lambda_\xi)_{i+\frac{1}{2},j,k} \Phi_{i+\frac{1}{2},j,k} \tag{3.48}$$

The function Φ controls the relative importance of dissipation in the three coordinate directions as:

$$\Phi_{i+\frac{1}{2},j,k} = 1 + max\left((\frac{(\lambda_\eta)_{i+\frac{1}{2},j,k}}{(\lambda_\xi)_{i+\frac{1}{2},j,k}})^\alpha, (\frac{(\lambda_\zeta)_{i+\frac{1}{2},j,k}}{(\lambda_\xi)_{i+\frac{1}{2},j,k}})^\alpha \right) \tag{3.49}$$

The directional eigenvalue scaling functions are defined by:

$$(\lambda_\xi)_{i+\frac{1}{2},j,k} = U_{i+\frac{1}{2},j,k} (S_\xi)_{i+\frac{1}{2},j,k} + c(S_\xi)_{i+\frac{1}{2},j,k} \tag{3.50}$$

$$(\lambda_\eta)_{i+\frac{1}{2},j,k} = U_{i+\frac{1}{2},j,k} (S_\eta)_{i+\frac{1}{2},j,k} + c(S_\eta)_{i+\frac{1}{2},j,k} \tag{3.51}$$

$$(\lambda_\zeta)_{i+\frac{1}{2},j,k} = U_{i+\frac{1}{2},j,k} (S_\zeta)_{i+\frac{1}{2},j,k} + c(S_\zeta)_{i+\frac{1}{2},j,k} \tag{3.52}$$

The use of the maximum function in the definition of Φ is important for grids where λ_η/λ_ξ and $\lambda_\zeta/\lambda_\xi$ are very large and of the same order of magnitude. In this case, if these ratios are summed rather than taking the maximum, the dissipation can become too large, resulting in degraded solution accuracy and poor convergence. Because three-dimensional solution grids tend to exhibit large variations in the cell aspect ratio, there is less freedom in the choice of the parameter α for this scheme, and a value of 0.5 was found to provide a robust scheme.

The coefficients in the dissipation operator use the solution pressure as a sensor for the presence of shock waves in the solution and are defined as:

$$\epsilon^2_{i+\frac{1}{2},j,k} = \kappa^2 max(\nu_{i-1,j,k}, \nu i, j, k, \nu_{i+1,j,k}, \nu_{i+2,j,k}) \tag{3.53}$$

$$\nu_{i,j,k} = \frac{|(p_{i-1,j,k} - 2p_{i,j,k} + p_{i+1,j,k})|}{(p_{i-1,j,k} + 2p_{i,j,k} + p_{i+1,j,k})} \tag{3.54}$$

$$\epsilon^4_{i+\frac{1}{2},j,k} = max(0, \kappa^4 - \epsilon^2_{i+\frac{1}{2},j,k}) \tag{3.55}$$

where κ^2, κ^4 are user-defined constants. Typical values for these variables are

$$\kappa^2 = \frac{1}{2} \qquad \kappa^4 = \frac{1}{64} \tag{3.56}$$

The dissipation operators in the η and ζ directions are defined in a similar manner.

3.8 Implicit Residual Smoothing

The stability range of the basic time-stepping scheme can be extended using implicit smoothing of the residuals. This technique was described by Hollanders et al. [37] for the Lax-Wendroff scheme and later developed by Jameson [35] for the Runge-Kutta scheme. Since an unsteady flow calculation for a given geometry and grid is likely to be computationally more expensive than a similar steady flow calculation, it would be advantageous to utilize this acceleration technique for time-dependent flow calculations as well. In recent calculations for two dimensional unsteady flows, Jorgensen and Chima [38] demonstrated that a variant of the implicit residual smoothing technique could be incorporated into a time-accurate explicit method to permit the use of larger calculation time increments without adversely affecting the results of the unsteady calculation. The implementation of this residual smoothing scheme reduced the CPU time for their calculation by a factor of five. This so-called time-accurate implicit residual smoothing operator was then also demonstrated by Rao and Delaney [39] for a similar two-dimensional unsteady calculation. Although this "time-accurate" implicit residual smoothing scheme is not

developed theoretically to accurately provide the unsteady solution, it can be demonstrated that errors introduced through this residual smoothing process are very local in nature, and are generally not greater than the discretization error.

The standard implicit residual smoothing operator can be written as:

$$(1 - \epsilon_\xi \triangle_\xi \nabla_\xi)(1 - \epsilon_\eta \triangle_\eta \nabla\eta)(1 - \epsilon_\zeta \triangle_\zeta \nabla_\zeta)\bar{R}m = Rm \tag{3.57}$$

where the residual Rm is defined as:

$$Rm = \alpha m \frac{\Delta t}{V}(Qm - Dm), \quad m = 1, mstages \tag{3.58}$$

for each of the m stages in the Runge-Kutta multistage scheme. Here Qm is the sum of the convective and diffusive terms, Dm the total dissipation at stage m, and $\bar{R}m$ the final (smoothed) residual at stage m.

The smoothing reduction is applied sequentially in each coordinate direction as:

$$\begin{aligned} R_m^* &= (1 - \epsilon_\xi \triangle_\xi \nabla_\xi)^{-1} Rm \\ R_m^{**} &= (1 - \epsilon_\eta \triangle_\eta \nabla\eta)^{-1} R_m^* \\ R_m^{***} &= (1 - \epsilon_\zeta \triangle_\zeta \nabla_\zeta)^{-1} R_m^{**} \\ \bar{R}m &= R_m^{***} \end{aligned} \tag{3.59}$$

where each of the first three steps above requires the inversion of a scalar tridiagonal matrix. The application of the residual smoothing operator varies with the type of Runge-Kutta time marching scheme selected. The full four and five stage time-marching schemes utilize residual smoothing at each stage of the Runge-Kutta integration. The reduced four stage scheme employs residual smoothing at the second and fourth stages only.

The use of constant coefficients (ϵ) in the implicit treatment has proven to be useful, even for meshes with high aspect ratio cells, provided additional support such as enthalpy damping (see [35]) is introduced. Unfortunately, the use of enthalpy damping, which assumes a constant total enthalpy throughout the flowfield, cannot be used for an unsteady flow, and many steady flows where the total enthalpy may vary. It has been shown that the need for enthalpy damping can be eliminated by using

variable coefficients in the implicit treatment which account for the variation of the cell aspect ratio. Martinelli [10] derived a functional form for the variable coefficients for two-dimensional flows which are functions of characteristic wave speeds. In this study, the three-dimensional extension described by Radespiel et al. [36] is utilized, and is expressed as:

$$\epsilon_\xi = max\left(0, \frac{1}{4}[\frac{CFL}{CFL_{max}}\frac{1+max(r^\alpha_{\eta\xi}r^\alpha_{\zeta\xi})}{1+max(r_{\eta\xi}r_{\zeta\xi})}]^2 - 1\right) \tag{3.60}$$

$$\epsilon_\eta = max\left(0, \frac{1}{4}[\frac{CFL}{CFL_{max}}\frac{1+max(r^\alpha_{\xi\eta}r^\alpha_{\eta\zeta})}{1+max(r_{\xi\eta}r_{\zeta\eta})}]^2 - 1\right) \tag{3.61}$$

$$\epsilon_\zeta = max\left(0, \frac{1}{4}[\frac{CFL}{CFL_{max}}\frac{1+max(r^\alpha_{\eta\zeta}r^\alpha_{\xi\zeta})}{1+max(r_{\eta\zeta}r_{\xi\zeta})}]^2 - 1\right) \tag{3.62}$$

CFL represents the local value of the CFL number based on the calculation time increment Δt, and CFL_{max} represents the maximum stable value of the CFL number permitted by the unmodified scheme (normally, in practice, this is chosen as 2.5 for a four stage scheme and 3.5 for a five stage scheme, although linear stability analysis suggests that $2\sqrt{2}$, and 3.75 are the theoretical limits for the four and five stage schemes, respectively). From this formulation it is obvious then that the residual smoothing operator is only applied in those regions where the local CFL number exceeds the stability-limited value. In this approach, the residual operator coefficient becomes zero at points where the local CFL number is less than that required by stability, and the influence of the smoothing is only locally applied to those regions exceeding the stability limit. Practical experience involving unsteady flow calculations suggests that for a constant time increment, the majority of the flowfield utilizes CFL numbers less than the stability-limited value to maintain a reasonable level of accuracy. Local smoothing is therefore typically required only in regions of small grid spacing, where the stability-limited time step is very small. Numerical tests both with and without the time-accurate implicit residual smoothing operator for the flows of interest in this study were found to produce essentially identical results, while the time-accurate residual smoothing resulted in a decrease in CPU time by a factor of 2-3. In practice, the actual limit on the calculation CFL number were determined to be roughly twice the values specified for CFL_{max}, above.

3.9 Turbulence Model

As a result of computer limitations regarding storage and execution speed, the effects of turbulence are introduced through an appropriate turbulence model and solutions are performed on a numerical grid designed to capture the macroscopic (rather than the microscopic) behavior of the flow. A relatively standard version of the Baldwin-Lomax [34] turbulence model was adopted for this analysis. This model is computationally efficient, and has been successfully applied to a wide range of geometries and flow conditions.

The effects of turbulence are introduced into the numerical scheme by utilizing the Boussinesq approximation (see e.g. [32]), resulting in an effective calculation viscosity defined as:

$$\mu_{effective} = \mu_{laminar} + \mu_{turbulent} \tag{3.63}$$

The simulation is therefore performed using an effective viscosity which combines the effects of the physical (laminar) viscosity and the effects of turbulence through the turbulence model and the turbulent viscosity $\mu_{turbulent}$.

The Baldwin-Lomax model specifies that the turbulent viscosity be based on an inner and outer layer of the boundary layer flow region as:

$$\mu_{turbulent} = \begin{cases} (\mu_{turbulent})_{inner}, & y \leq y_{crossover} \\ (\mu_{turbulent})_{outer}, & y > y_{crossover} \end{cases} \tag{3.64}$$

where y is the normal distance to the nearest wall, and $y_{crossover}$ is the smallest value of y at which values from the inner and outer models are equal. The inner and outer model turbulent viscosities are defined as:

$$(\mu_{turb})_{inner} = \rho l^2 |\omega| \tag{3.65}$$

$$(\mu_{turb})_{outer} = KC_{cp}\rho F_{wake} F_{kleb} y \tag{3.66}$$

Here, the term l is the Van Driest damping factor

$$l = ky(1 - e^{(-y^+/A^+)}) \tag{3.67}$$

ω is the vorticity magnitude, F_{wake} is defined as:

$$F_{wake} = y_{max} F_{max} \tag{3.68}$$

where the quantities y_{max}, F_{max} are determined from the function

$$F(y) = y|\omega|[1 - e^{(-y^+/A^+)}] \tag{3.69}$$

The term y^+ is defined as

$$y\sqrt{\frac{\rho|\omega|}{\mu_{laminar}}} \tag{3.70}$$

The quantity F_{MAX} is the maximum value of $F(y)$ that occurs in a profile, and y_{MAX} is the value of y at which it occurs. The determination of F_{MAX} and y_{MAX} is perhaps the most difficult aspect of this model for three-dimensional flows. The profile of $F(y)$ versus y can have several local maximums, and it is often difficult to establish which values should be used. In this case, F_{MAX} is taken as the maximum value of $F(y)$ between a y^+ value of 350.0 and 1000.0. The function F_{kleb} is the Klebanoff intermittency factor given by

$$F_{kleb}(y) = [1 + 5.5(\frac{C_{kleb}y}{y_{max}})^6]^{-1} \tag{3.71}$$

and the remainder of the terms are constants defined as:

$$\begin{aligned} A^+ &= 26, \\ C_{cp} &= 1.6, \\ C_{kleb} &= 0.3, \\ k &= 0.4, \\ K &= 0.0168 \end{aligned} \tag{3.72}$$

In practice, the turbulent viscosity is limited such that it never exceeds 1000.0 times the laminar viscosity.

The turbulent flow thermal conductivity term is also treated as the combination of a laminar and turbulent quantity as:

$$k_{effective} = k_{laminar} + k_{turbulent} \tag{3.73}$$

For turbulent flows, the turbulent thermal conductivity $k_{turbulent}$ is determined from a turbulent Prandtl number $Pr_{turbulent}$ such that

$$Pr_{turbulent} = \frac{c_p \mu_{turbulent}}{k_{turbulent}} \tag{3.74}$$

The turbulent Prandtl number is normally chosen to have a value of 0.9.

In order to properly utilize this turbulence model, a fairly large number of grid cells must be present in the boundary layer flow region, and, perhaps of greater importance, the spacing of the first grid cell off of a wall should be small enough to accurately account for the inner "law of the wall" turbulent boundary layer profile region. Unfortunately, this constraint is typically not satisfied due to grid-induced problems or excessive computational costs, especially for time-dependent flow calculations. A convenient technique to suppress this problem is the use of wall functions to replace the inner turbulent model function, and solve for the flow on a somewhat coarser grid. The wall function technique has been successfully demonstrated [29] for computer programs based on a numerical algorithm similar to the *ADPAC-AOACR* solution scheme. Unfortunately, this technique has not been implemented or tested for the current application. It appears that the use of wall functions is a reasonable area for future research.

Practical applications of the Baldwin-Lomax model for three-dimensional viscous flow must be made with the limitations of the model in mind. The Baldwin-Lomax model was designed for the prediction of wall bounded turbulent shear layers, and is not likely to be well suited for flows with massive separations or large vortical structures. There are, unfortunately, a number of applications for ducted and unducted propfans where this model is likely to be invalid. This is also likely to be an area requiring improvement in the future.

3.10 Multigrid Convergence Acceleration

Multigrid (not to be confused with a multiple blocked grid!) is a numerical solution technique which attempts to accelerate the convergence of an iterative process (such as a steady flow prediction using a time-marching scheme) by computing corrections to the solution on coarser meshes and propagating these changes to the fine

mesh through interpolation. This operation may be recursively applied to several coarsenings of the original mesh to effectively enhance the overall convergence. In the present multigrid application, coarse meshes are derived from the preceding finer mesh by eliminating every other mesh line in each coordinate direction as shown in Figure 3.6. As a result, the number of multigrid levels (coarse mesh divisions) is controlled by the mesh size, and, in the case of the *ADPAC-AOACR* code, also by the indices of the embedded mesh boundaries (such as blade leading and trailing edges, etc.) (see Figure 3.6). These restrictions suggest that mesh blocks should be constructed such that the internal boundaries and overall size coincide with numbers which are compatible with the multigrid solution procedure (i.e., the mesh size should be 1 greater than any number which can be divided by 2 several times and remain whole numbers: e.g. 9, 17, 33, 65 etc.)

The multigrid procedure is applied in a V-cycle as shown in Figure 3.7, whereby the fine mesh solution is initially "injected" into the next coarser mesh, the appropriate forcing functions are then calculated based on the differences between the calculated coarse mesh residual and the residual which results from a summation of the fine mesh residuals for the coarse mesh cell, and the solution is advanced on the coarse mesh. This sequence is repeated on each successively coarser mesh until the coarsest mesh is reached. At this point, the correction to the solution $(Q^{n+1}_{i,j,k} - Q^{n}_{i,j,k})$ is interpolated to the next finer mesh, a new solution is defined on that mesh, and the interpolation of corrections is applied sequentially until the finest mesh is reached. Following a concept suggested by Swanson et al. [36], it is sometimes desirable to smooth the final corrections on the finest mesh to reduce the effects of oscillations induced by the interpolation process. A constant coefficient implementation of the implicit residual smoothing scheme described in Section 3.5 is used for this purpose. The value of the smoothing constant is normally taken to be 0.2.

A second multigrid concept which should be discussed is the so-called "full" multigrid startup procedure. The "full" multigrid method is used to initialize a solution by first computing the flow on a coarse mesh, performing several time-marching iterations on that mesh (which, by the way could be multigrid iterations if successively coarser meshes are available), and then interpolating the solution at that point to the next finer mesh, and repeating the entire process until the finest mesh level

Multigrid Algorithm Mesh Level Description

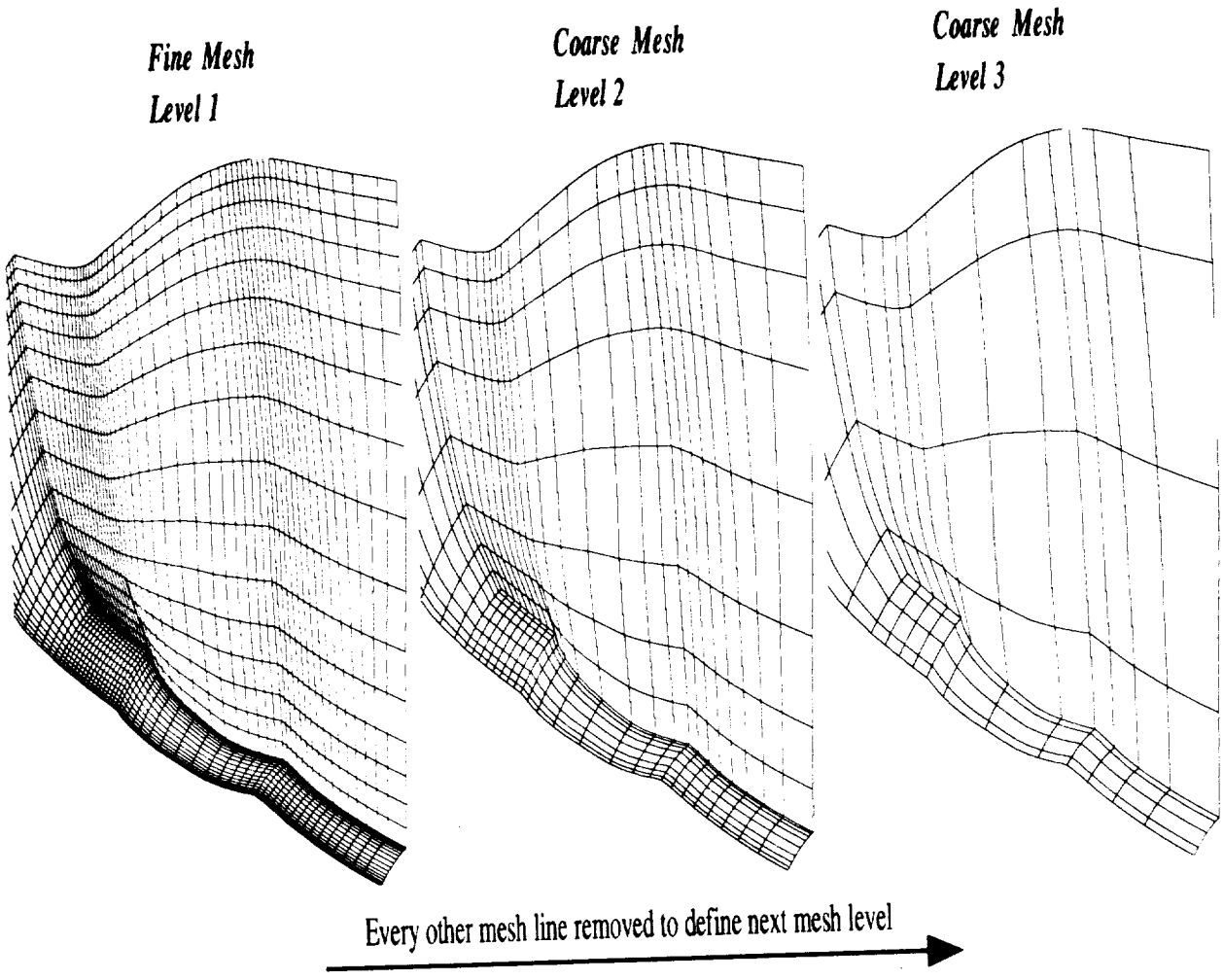

Grid lines defining mesh boundaries and internal boundaries (blade leading edges, trailing edges, etc.) must be consistent with the mesh coarsening process (cannot remove a mesh line defining a boundary for the given coordinate direction)

Figure 3.6: Multigrid Mesh Coarsening Strategy and Mesh Index Relation

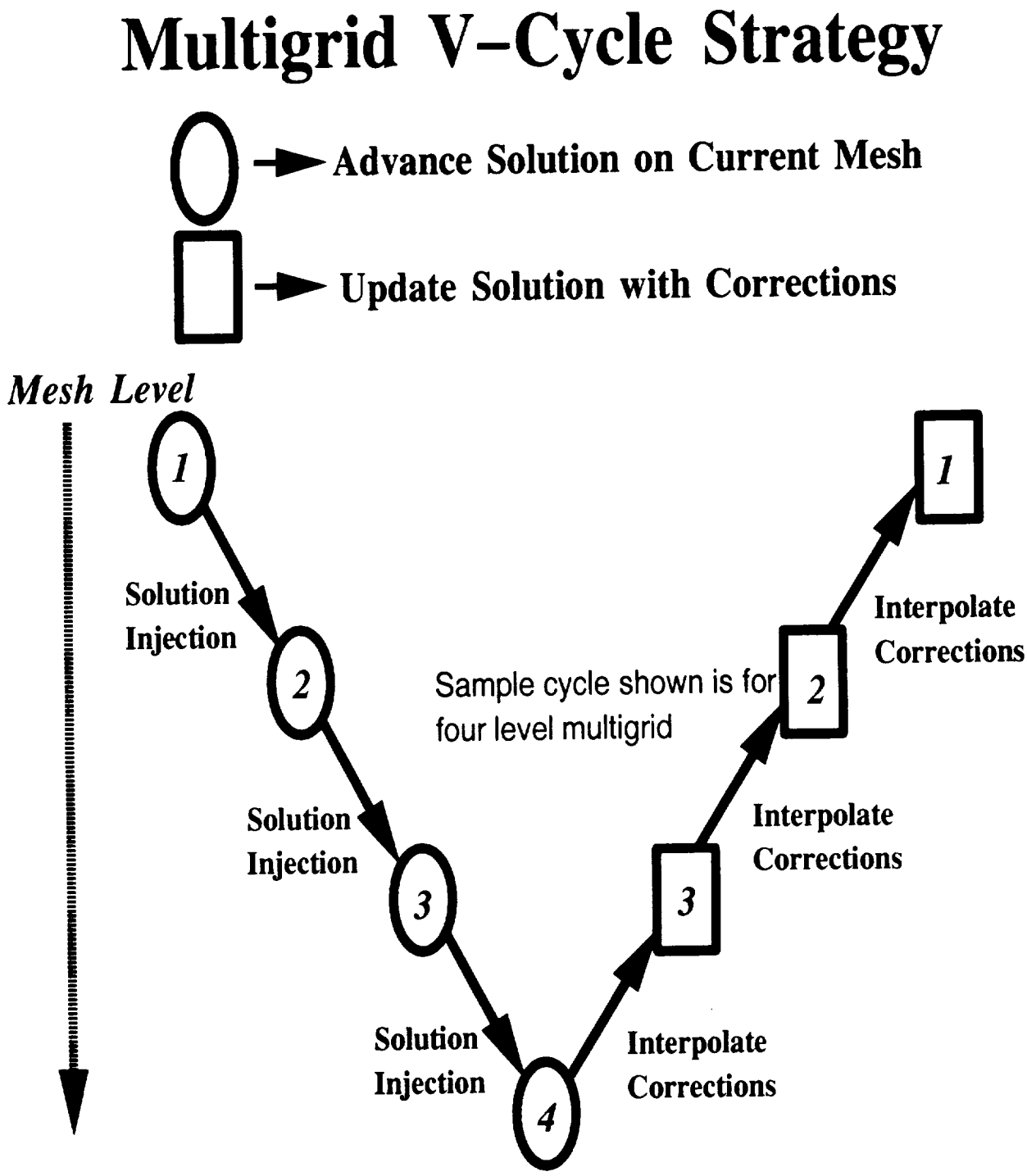

Figure 3.7: Multigrid V Cycle Strategy

is reached. The intent here is to generate a reasonably approximate solution on the coarser meshes before undergoing the expense of the fine mesh multigrid cycles. Again, the "full" multigrid technique only applies to starting up a solution.

3.11 Single Block Boundary Conditions

In this section, the various boundary conditions which are available as part of the *ADPAC-AOACR* code pertaining to a single mesh block are described. Before describing the individual boundary conditions, it may be useful to describe how the boundary conditions are imposed in the discrete numerical solution. Finite volume solution algorithms such as the *ADPAC-AOACR* program typically employ the concept of a phantom cell to impose boundary conditions on the external faces of a particular mesh block. This concept is illustrated graphically for a 2-D mesh representation in Figure 3.8.

A phantom cell is a fictitious neighboring cell located outside the extent of a mesh which is utilized in the application of boundary conditions on the outer boundaries of a mesh block. Since flow variables cannot be directly specified at a mesh surface in a finite volume solution (the flow variables are calculated and stored at cell centers), the boundary data specified in the phantom cells are utilized to control the flux condition at the cell faces of the outer boundary of the mesh block, and, in turn, satisfy a particular boundary condition. All *ADPAC-AOACR* boundary condition specifications provide data values for phantom cells to implement a particular mathematical boundary condition on the mesh. Another advantage of the phantom cell approach is that it permits unmodified application of the interior point scheme at near boundary cells.

Inflow and exit boundary conditions are applied numerically using characteristic theory. A one-dimensional isentropic system of equations is utilized to derive the following characteristic equations at an axial inflow/outflow boundary:

$$\frac{\partial C^-}{\partial t} - (v_z - a)\frac{\partial C^-}{\partial z} = 0, \tag{3.75}$$

$$\frac{\partial C^+}{\partial t} + (v_z + a)\frac{\partial C^+}{\partial z} = 0 \tag{3.76}$$

2–D Mesh Block Phantom Cell Representation

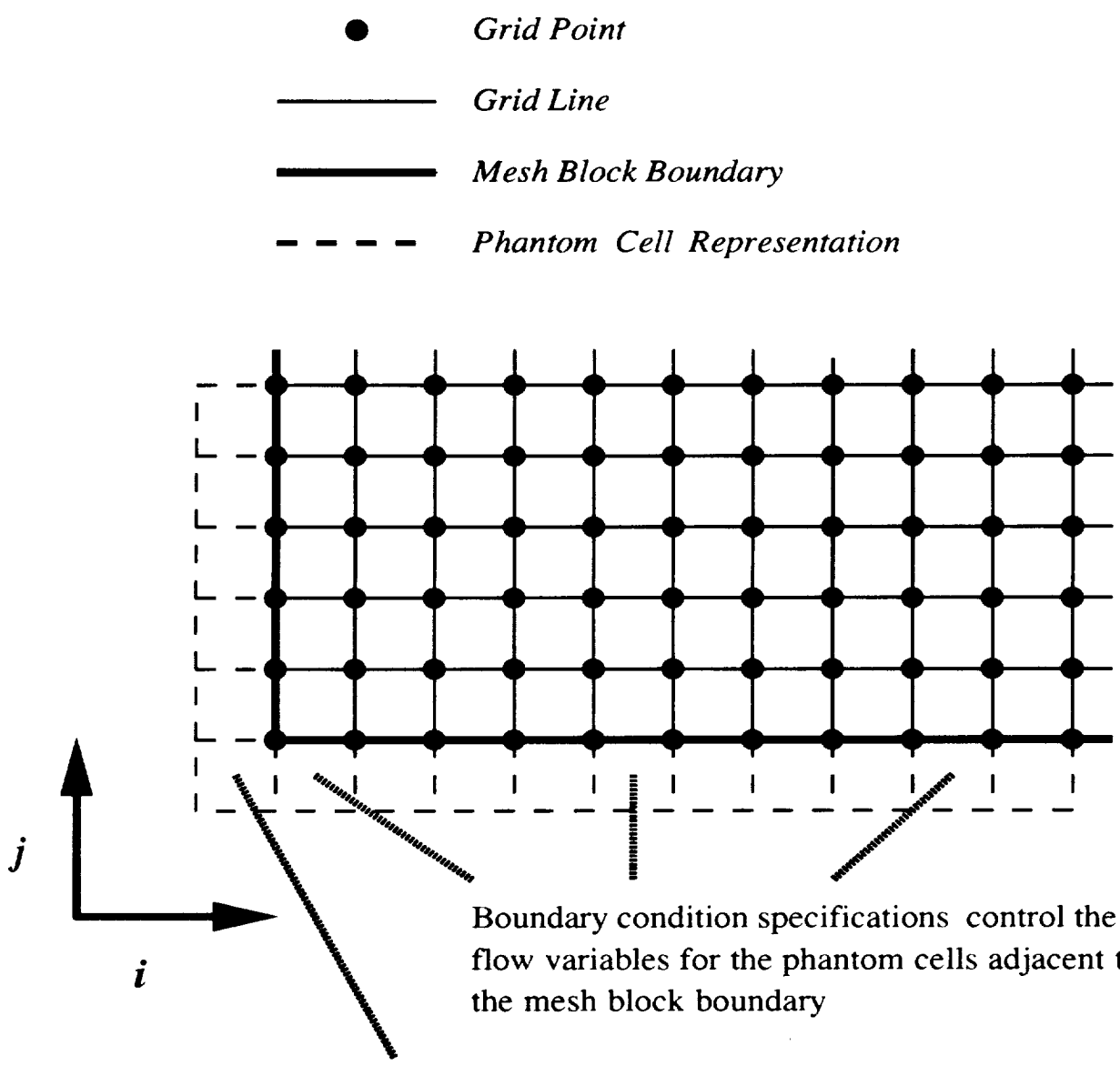

Figure 3.8: 2-D Mesh Block Phantom Cell Representation

where:

$$C^- = v_z - \frac{2a}{\gamma - 1}, \qquad C^+ = v_z + \frac{2a}{\gamma - 1} \tag{3.77}$$

For subsonic normal inflow, the upstream running invariant C^- is extrapolated to the inlet, and along with the equation of state, specified total pressure, total temperature, and flow angle (used to specify the angle of attack), the flow variables at the boundary may be determined. Inlet boundaries also require the specification of a flow direction. This is accomplished in one of two different manners. For turbomachinery based flow calculations, it is typical to specify a radial and circumferential (swirl) flow angle. For external flow calculations (such as angle of attack flow analysis) a Cartesian based flow angle is prescribed. It should be mentioned that the effective inflow angle in this case may vary for a given block as it rotates about the axis, and therefore the inflow angle is actually a function of circumferential position, θ.

Outflow boundaries require a specification of the exit static pressure at either the bottom or top of the exit plane. The remaining pressures along the outflow boundary are calculated by integrating the radial momentum equation:

$$\frac{\partial p}{\partial r} = \frac{\rho v_\theta^2}{r} \tag{3.78}$$

In this case, the downstream running invariant C^+ is used to update the phantom cells at the exit boundary.

Far-field boundaries also use the characteristic technique based on whether the local flow normal to the boundary passes into or out of the domain.

All solid surfaces (hub, cowl, airfoils) must satisfy either flow tangency for inviscid flow:

$$\vec{V} \cdot \vec{n} = 0 \tag{3.79}$$

or no slip for viscous flows:

$$v_z = 0, \qquad v_r = 0, \qquad v_\theta = r\omega \tag{3.80}$$

In both cases, no convective flux through the boundary (an impermeable surface) is permitted. The phantom cell velocity components are thus constructed to ensure that

the cell face average velocities used in the convective flux calculation are identically zero. The phantom cell pressure is simply extrapolated based on the boundary layer flow concept $dp/dn = 0$ (although for inviscid flows a normal momentum equation is likely to be more accurate). In the present applications, for inviscid flows, extrapolation was found to be the most effective technique based on rapid convergence and solution accuracy. The phantom cell density or temperature is imposed by assuming either an adiabatic surface $dT/dn = 0$ or a specified surface temperature, which suggests that the phantom cell temperature must be properly constructed to satisfy the appropriate average temperature along the surface.

Some final comments concerning boundaries are in order at this point. Artificial damping is applied at the block boundaries by prescribing zero dissipation flux along block boundaries to maintain the global conservative nature of the solution for each mesh block. Fourth order dissipation fluxes at near boundary cells are computed using a modified one-sided differencing scheme. Implicit residual smoothing is applied at the block boundary by imposing a zero residual gradient (i.e. $(dR/dz) = 0.0$) condition at the boundary.

3.12 Multiple-Block Coupling Boundary Conditions

For the multiple-block scheme, the solution is performed on a single grid block at a time. Special boundary conditions along block boundaries are therefore required to provide some transport of information between blocks. This transport is provided through one of four types of procedures. Each procedure applies to a different type of mesh construction and flow environment, and details of each approach are given in the paragraphs below.

For neighboring mesh blocks which have coincident mesh points along the interface separating the two blocks, a simple direct specification of the phantom cell data based on the near boundary cell data from the neighboring block has been used successfully. This concept is illustrated graphically in Figure 3.9. Each phantom cell in the block of interest has a direct correspondance with a near boundary cell in the neighboring mesh block, and the block coupling is achieved numerically by simply

Contiguous Mesh Block Interface Boundary Coupling Scheme

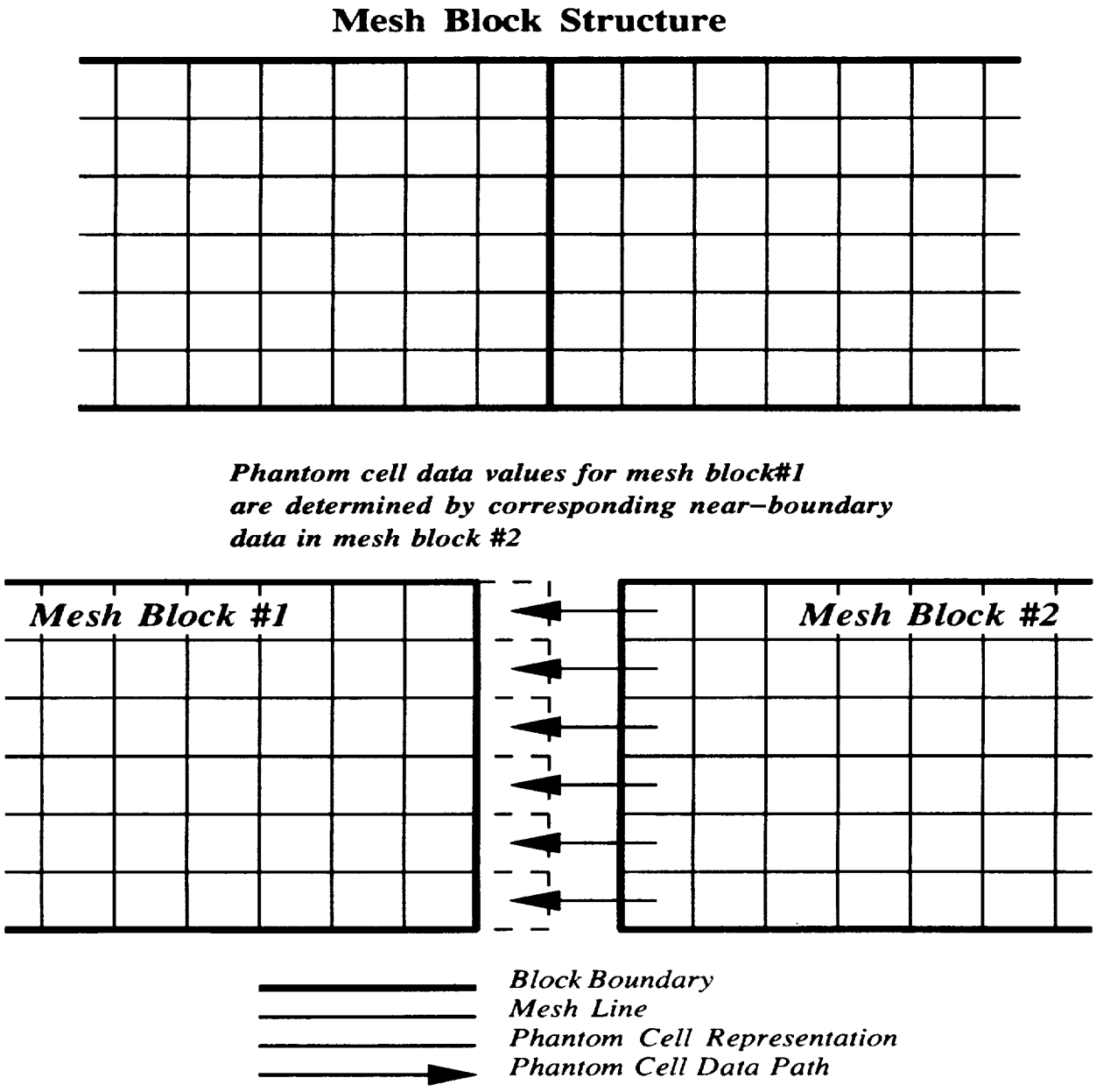

Figure 3.9: *ADPAC-AOACR* Contiguous Mesh Block Coupling Scheme

assigning the value of the corresponding cell in the neighboring block to the phantom cell of the block of interest. This procedure essentially duplicates the interior point solution scheme for the near boundary cells, and uniformly enforces the conservation principles implied by the governing equations.

For mesh block interfaces which do not have coincident points, but which define essentially the same surface, it is necessary to perform some type of interpolation to determine representative values for the block-specific phantom cells absed on the near boundary interface data from the neighboring mesh block. A relatively simple interpolation scheme based on an electrical resistance analogy was developed for this purpose, and is illustrated graphically for a non-contiguous mesh block interface as shown in Figure 3.10. To determine the phantom cell data for a non-contiguous mesh block interface, the center of the nearest cell face for the particular phantom cell is determined by averaging the coordinates of the four mesh points which determine the cell face. A search is then performed in the neighboring mesh block along the same interface to determine the cell face whose center lies closest to the phantom cell face center of interest. It is assumed that both mesh blocks share a common surface at the interface of interest, in spite of the fact that this surface is defined by different points. This assumption thus requires that the block boundaries do not overlap, and that the physical extent of the boundaries are approximately equal. Once the nearest cell in the neighboring mesh block has been located, the nearest set of four cells in the neighboring mesh is determined, and an electrical circuit analogy is used to interpolate the phantom cell boundary data from the four cells of neighboring mesh block data. The circuit analogy simply sets a resistance for each path of neighboring cell data to the phantom cell center based on the physical distance between the centers of each cell face (again, this concept is illustrated in Figure 3.10. The four neighboring cell near boundary data are then treated as voltages, and the phantom cell data are determined by calculating the appropriate "voltage" potential at the phantom cell face center based on the neighboring cell face center data and the resistance along each path. This scheme has the advantages of being simple to program, is extremely stable, and identically duplicates the contiguous mesh block interface phantom cell representation, described above, for interfaces which have contiguous mesh points. The disadvantages of this approach are that the interpolation is essentially linear,

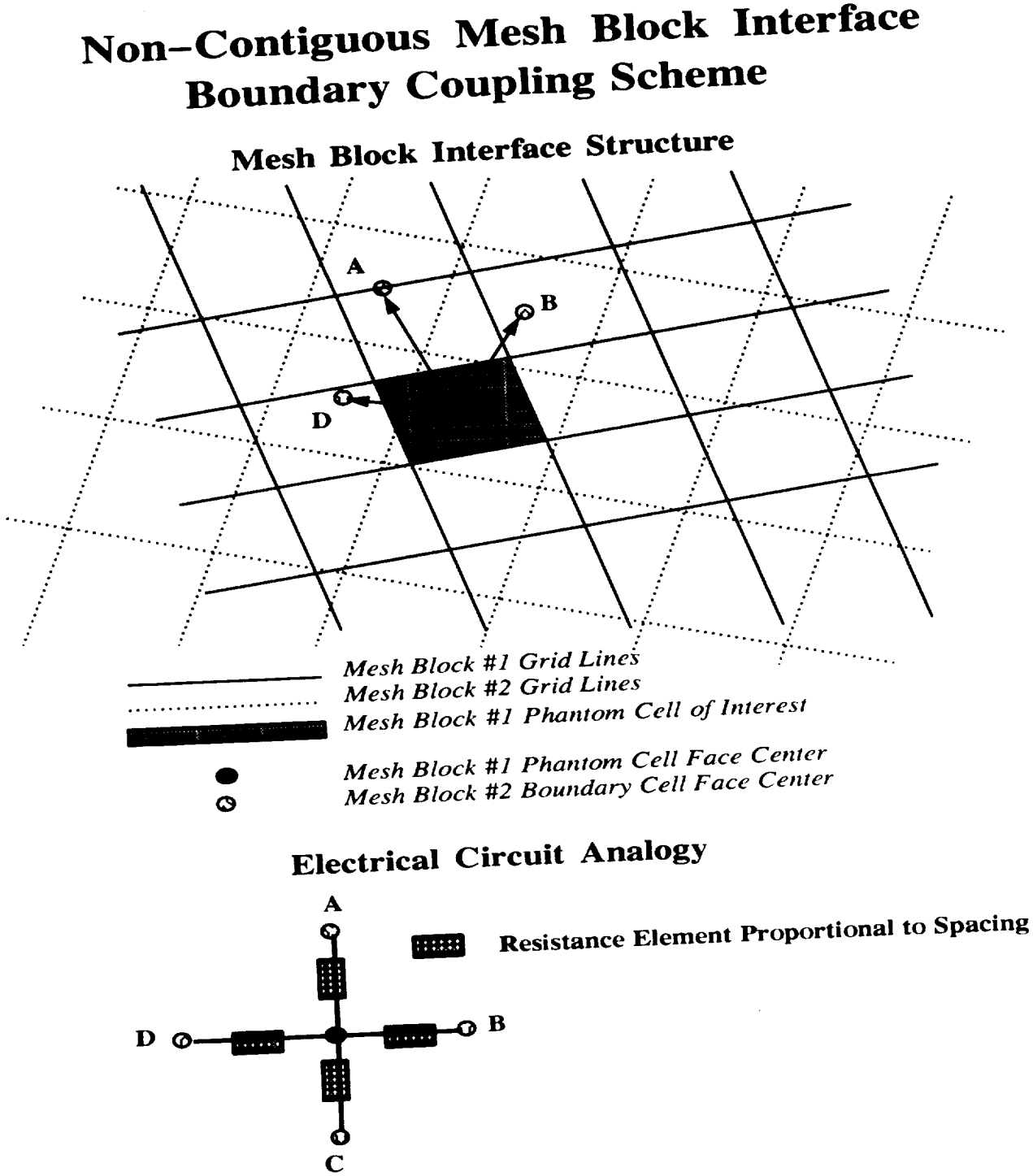

Figure 3.10: *ADPAC-AOACR* Non-Contiguous Mesh Block Coupling Scheme

and that the scheme is not uniformly conservative, and is thus subject to errors is mass, momentum, and energy conservation. These sources of error scale roughly with the mesh spacing, and therefore, the finer the mesh , the lower the impact these errors have on the overall solution.

The third type of mesh block interface boundary patching scheme relates to steady flow calculations involving turbomachinery components with multiple blade rows, or to a lesser extent, steady flow calculations involving mesh systems with differing circumferential extents. This approach is a technique for the prediction of steady flow through multistage turbomachinery based on the mixing plane concept. A mixing plane is an arbitrarily imposed boundary inserted between adjacent blade rows across which the flow is "mixed out" circumferentially. This circumferential mixing approximates the time-averaged condition at the mixing plane and allows the aerodynamic solution for each blade passage to be performed in a steady flow environment. The mixing plane concept was recently applied to realistic turbofan engine configurations by Dawes [6]. Flow variables on either side of the mixing plane are circumferentially averaged and passed to the neighboring blade row as a means of smearing out the circumferential nonuniformities resulting from dissimilar blade counts. The mixing plane concept is a cost-effective approach computationally because the flow is steady, and the individual blade passage domains are limited to a near-blade region. Unfortunately, the accuracy of this approach is clearly questionable under some circumstances because of the placement of the mixing plane and the loss of spatial information resulting from the circumferential averaging operator. Numerically, then, the mesh points in two adjacent blocks at a mixing plane interface must have identical axial and radial coordinates. This permits specifying the circumferential distribution of phantom cells in one block as the circumferential average of the near boundary cell data from the adjacent block. This concept is illustrated graphically in Figure 3.11. The individual primitive flow variables are each circumferentially averaged, and used directly in the phantom cell data specification. Attempts to use several of the more complex mixing analyses based on the circumferentially averaged flow data, or the use of characteristic-based boundary specification based on the flow data were both subject to numerical instabilities under particular circumstances, and therefore, the direct specification method is used instead.

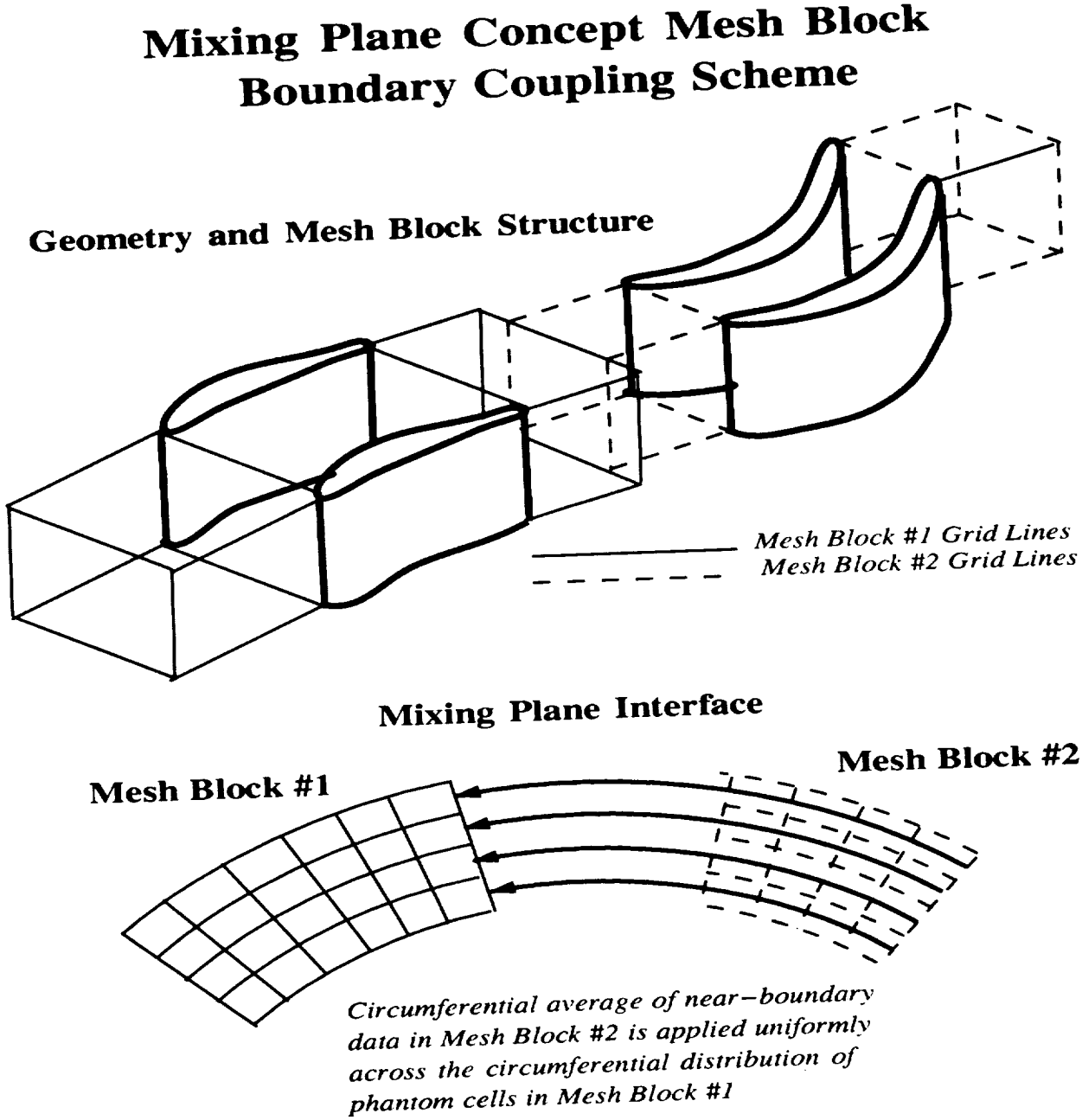

Figure 3.11: *ADPAC-AOACR* Circumferential Averaging (Mixing Plane) Mesh Block Coupling Scheme for Multiple Blade Row Calculations

The fourth type of mesh block interface boundary patching scheme relates to time-dependent calculations involving relative motion between adjacent mesh blocks. In this case, the mesh interface is essentially noncontiguous, and the relative position between mesh cells is changing in time. This type of boundary scheme is used for the prediction of rotor/stator interaction for multiple blade row turbomachines. This type of interface is complicated by the fact that the interface may be defined by different mesh blocks at different times based on the degree of motion between the adjacent mesh blocks. For example, if a calculation for a single stage compressor involves 3 passages of the upstream blade row, and four passages of the downstream blade row, then it is obvious that at some point during the calculation, each of the three mesh blocks in the upstream blade row representation will at some time have to communicate with each of the four mesh blocks in the downstream blade row representation. The specific mesh block in the communication path is determined by the degree of rotation in both the upstream and downstream blade rows, and is inherently time dependent. This task is simplified considerably by requiring that the mesh points in each block along the interface have constant axial and radial coordinates. This simplification reduces the overall problem to a time-space interpolation in the circumferential direction only (see Figure 3.12).

With this simplification, it is possible to simply define the interpolation data by resolving the relative position between the mesh blocks, extracting the near boundary data values from the neighboring mesh blocks, and interpolating for the phantom cell data value based on the current circumferential position of the phantom cell face center relative to the neighboring interpolant data arrays. Without modification, this scheme is nonconservative and can result in spurious errors in mass, momentum, and energy conservation across the mesh block interface. In order to rectify this problem, a modified interpolation scheme was tested which attempted to enforce global conservation of the interpolated data across each circumferential interpolation "slice" of the mesh. This restriction was enforced by globally summing the interpolated values for each circumferential interpolation and modifying the summation to satisfy the global conservation defined by the interpolant data. The individual interpolated phantom cell values were then uniformly modified to reflect the global conservation correction. Numerical experiments with this scheme compared to the unmodified scheme were

Time/Space Resolved Interpolation Mesh Block Boundary Coupling Scheme

Geometry and Mesh Block Structure
(Circumferential Pitch of Each Blade Row Representation is Constant)

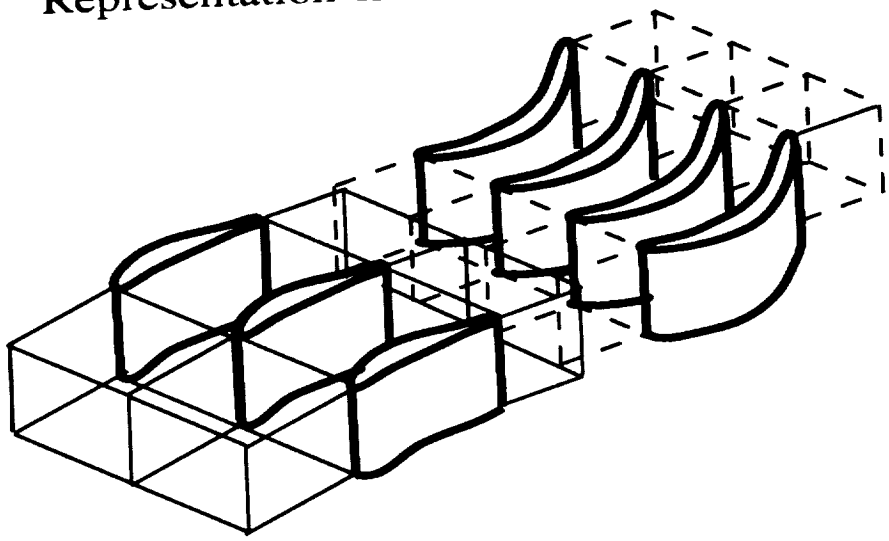

Boundary Surface Interface

Blade Row #1

Blade Row #2

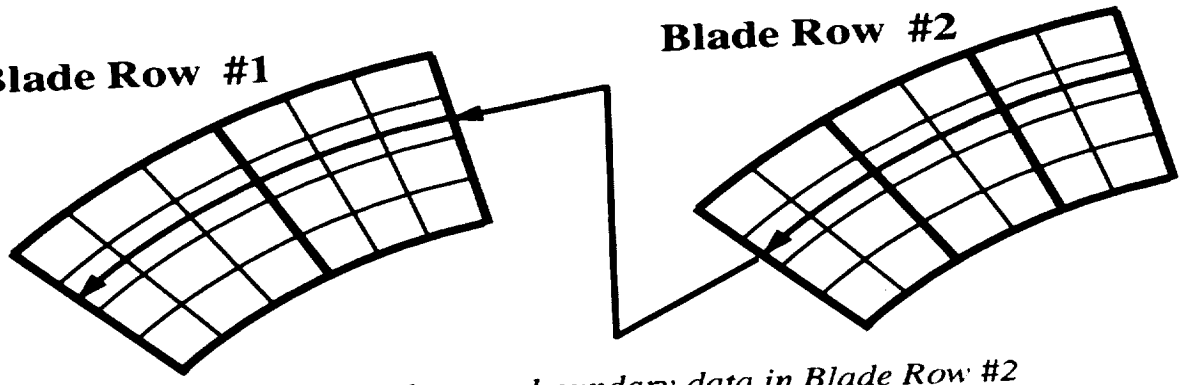

Time/space resolved near–boundary data in Blade Row #2 Mesh Blocks are utilized as an interpolation stencil for circumferential distribution of phantom cells in Blade Row #1 Mesh Blocks

Figure 3.12: *ADPAC-AOACR* Time/Space Resolved Mesh Block Coupling Scheme for Multiple Blade Row Calculations

virtually identical, and it was not possible to draw any hard conclusions regarding the advantages of one scheme over another. Following this test, the correction scheme was eliminated for simplicity. The effects of conservation across block interface boundaries is likely to be a debatable issue; however, there is considerable numerical evidence available which suggest that solution accuracy (for the types of calculations considered in this study) is not significantly influenced by non-conservative interpolation schemes ([12], [39]) and that supposed conservative interface coupling schemes [13] do not necessarily ensure conservation when used with numerical schemes which are not conservative in time.

3.13 Solution Procedure

The overall solution procedure begins by defining a set of initial data, and advancing the solution from that point forward in time until the desired solution (steady state, time-periodic, or finite time interval) has been reached. Initial data is normally specified as a uniform flow, or may be read in as a "restart" of a previous existing solution. Normally, for steady flow calculations, the "full" multigrid startup procedure is utilized to accelerate convergence by initializing the solution on a coarse mesh before incurring the expense of fine mesh iterations. Steady state solutions are deemed converged when the average residual R has been reduced by a factor of 10^{-3}, or when the residual has ceased to be reduced. It is possible that for some steady flow calculations, the solution is truly unsteady (i.e. - vortex shedding behind a circular cylinder) and in these cases the residual may not be reduced beyond a certain limit.

For time-dependent flow simulations, it has been found that it is often desirable to first initialize the solution in a steady flow manner using mixing planes or other time-averaged boundary condition procedures to define a reasonable approximation to the time-averaged flow before proceeding with the time-accurate iteration procedure. The unsteady solution may then be advanced in time with a uniformly specified time step, until a time-periodic solution is achieved. The amount of time required to reach a time-periodic solution is typically highly case dependent, and such solutions must be monitored closely to determine when the solution is satisfactory.

Some comments are in order to explain the solution procedure for high speed

rotors, many of which are illustrated in the results section in this report. It has been found that solutions for high speed compressor rotors typically require exit static pressure in excess of the inlet total pressure. As a result, it is often not possible to obtain an immediate solution under the desired operating condition because of the potential for reversed flow at an exit boundary which results from the relatively large exit static pressure. To overcome this problem, the following procedure has been implemented to obtain high speed rotor flowfield solutions. Typically, the solution is started using an exit static pressure which is lower than the inlet total pressure. For example, for a fan rotor with a design exit static to inlet total pressure ratio of 1.13, the solution may be started with an exit static to inlet total pressure ratio of 0.95. The resulting solution typically chokes the flow in the blade passage and sets up a shock system which is consistent with the choked flowfield. Once this flow is established, the exit static pressure may be raised incrementally, and the solution restarted several times until the desired exit static pressure ratio is reached. It should be emphasized that the increases in back pressure must be done conservatively to avoid prematurely stalling the blade passage.

4. RESULTS

In this chapter, numerical results from the *ADPAC-AOACR* 3D Euler/Navier-Stokes code are presented and compared with existing data to demonstrate and verify the accuracy of the analysis. The results are primarily based on applications involving ducted and unducted fans with multiple blade rows; however, several additional calculations are presented to demonstrate the versatility of the code.

Steady flow predictions involving turbomachinery geometries are presented first, followed by several calculations of time-dependent flowfields involving multiple blade row turbomachines.

4.1 2-D Compressor Cavity Flow (Steady Flow)

In light of the recent addition of the two-dimensional block solution capability in the *ADPAC-AOACR* analysis code, a two-dimensional test demonstration for a complex flow is appropriate. One such flow of interest to turbomachinery designers is the flow in a compressor hub cavity for compressors which employ inner banded stators. The exact characteristics of the leakage flow through the cavity and the resulting interplay between the leakage flow and the primary gas flow are not completely understood. As such, inner banded stator seal design is currently an area of concentrated investigation for high performance gas turbine engines.

The *ADPAC-AOACR* analysis was applied to predict the two-dimensional flow in an inner-banded stator hub cavity design considered for an advanced compressor design at Allison. This geometry, and the 149x61 mesh system used in the analysis are illustrated in Figure 4.1. This complex mesh system is actually rectangular in computational space, and the application of the appropriate boundary conditions is a trivial matter for the *ADPAC-AOACR* analysis. The time-marching calculation was

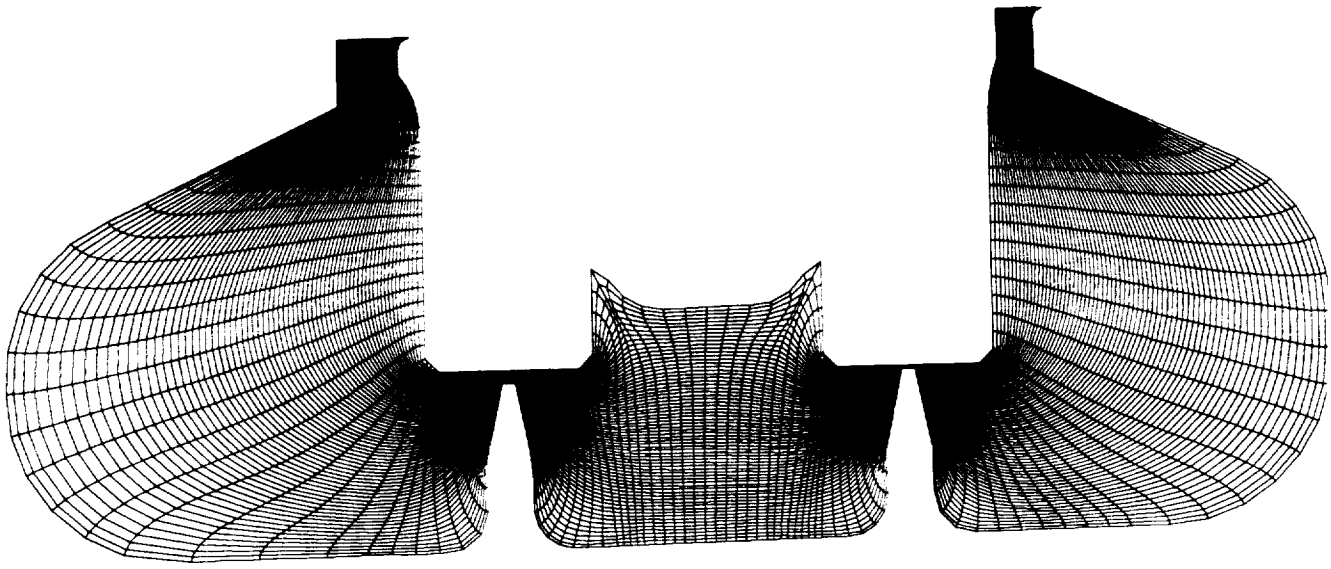

Figure 4.1: Inner Banded Stator Cavity Geometry and *ADPAC-AOACR* 2-D Mesh System

advanced with a CFL number of 5, utilized 3 levels of multigrid, and employed the full multigrid startup procedure. The residual convergence history resulting from this calculation is given in Figure 4.2. The full multigrid startup procedure consisted of 200 iterations on each of the 2 coarse mesh levels, followed by 100 fine mesh iterations. The overall convergence for this case was excellent, with the average residual reduced a full four orders of magnitude in only 100 fine mesh iterations.

The predicted steady flow velocity vector pattern for this flow is given in Figure 4.3. It should be noted that the flow in the cavity is from left to right in this orientation. The flow consists of a complex pattern of recirculating vortices, coupled with the high speed, high loss flow through the knife seals. It is particularly interesting to note the standing vortices at the inlet and exit of the cavity flowpath. Although no experimental data were available to verify these results, the predicted 2-D flow was in good agreement with a similar 3-D flow prediction from the *ADPAC-AOACR* analysis, and a similar 2-D flow predictions based on a separate 2-D Navier-Stokes code.

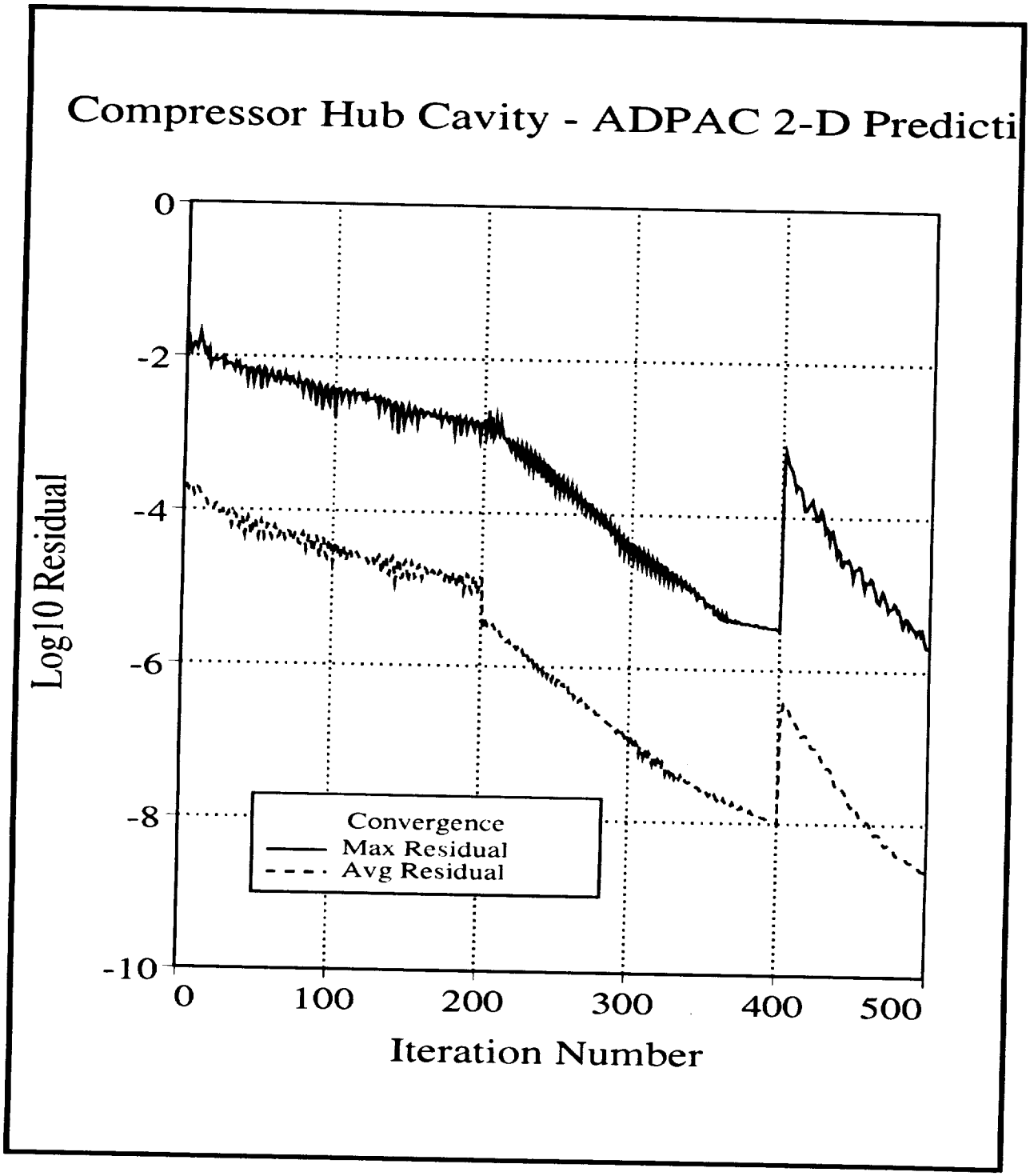

Figure 4.2: *ADPAC-AOACR* Full Multigrid Convergence History for 2-D Inner Banded Stator Cavity Flow Calculation

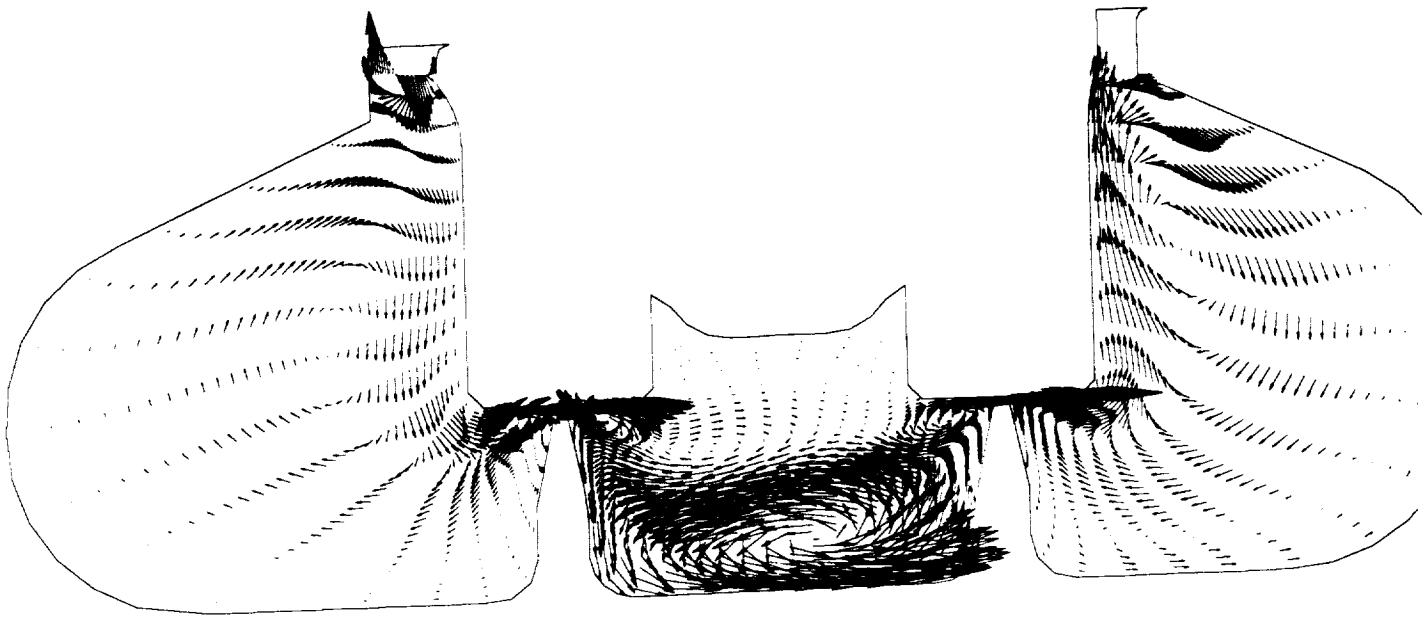

Figure 4.3: *ADPAC-AOACR* Predicted Velocity Vectors for 2-D Inner Banded Stator Cavity Flow Analysis

4.2 Model Counterrotating Propfan (Steady Flow)

The first results presented are for a model counterrotating propfan geometry. Geometric and aerodynamic design parameters for the model counterrotating propeller are given in Figure 4.4. The calculations presented here were based on a cruise condition with a flight Mach number of 0.72, and advance ratio of 3.14. The forward and rearward blade setting angles were 57.4 and 60.0 degrees, respectively. Steady flow performance predictions were obtained for this case by solving the Navier-Stokes equations with the inter-blade row mixing plane concept described in Section 3.2. The grid therefore consists of two blocks (one for each blade row), divided by the mixing plane approximately midway between the two blade rows. Our experience suggests that propfan airfoils are sufficiently flexible that in order to accurately capture aerodynamic performance, it is necessary to perform coupled structural/aerodynamic analyses to deduce the airfoil shape under the desired operating conditions. For the purposes of this demonstration, the individual mesh blocks were generated based on an assumed fixed running airfoil shape.

It should be noted that this grid system corresponds to standard configuration #7 as described in the *ADPAC-AOACR* Computer Program Users Manual [9]. The grid block sizes were 65x49x33 and 57x49x33, respectively. An illustration of the mesh system is given in Figure 4.5. The calculations presented here are essentially for demonstration purposes only. In practice, the exit boundary should probably be extended farther downstream to obtain best results.

Calculations for this geometry utilized 3 levels of multigrid, and employed the full multigrid startup procedure. A total of 100 iterations were performed on each of the coarse mesh levels during the full multigrid startup, followed by 200 iterations of the fine mesh solver. The CFL number was fixed at 5.0, and the modified four stage time-marching algorithm was employed. An illustration of the convergence history for this case is given in Figure 4.6.

The overall convergence of the multigrid procedure was observed to be quite rapid, requiring only 200 fine mesh iterations to achieve a 3 order reduction of the average solution residual (error). An illustration of the predicted surface static pressure contours and radial blade-to-blade static pressure contours are given in Figure 4.7. The blade to blade static pressure contours clearly illustrate the tip vortex flow near the suction side of each blade. No leading edge vortex was observed in the predictions for either blade row under this operating condition, which appears to be supported by experimental evidence. The overall predicted power coefficient for this case was 2.05 which is in good agreement with the design value of 2.035.

Two images are presented in Figures 4.8 and 4.9 to illustrate the effectiveness of the mixing plane boundary patching procedure for this type of flow. Figure 4.8 illustrates predicted absolute Mach number contours for the axisymmetric averaged flowfield. The blade boundaries and location of the mixing plane are outlined. The corresponding axisymmetric averaged flow static pressure contours are given in Figure 4.9. Both sets of contours display a smooth transition across the mixing plane and display no noticeable abnormalities as a result of the mixing plane assumption. Another plot, given on Figure 4.10, illustrates the circumferential blade to blade static pressure contours at midspan for the mixing plane calculation. The mesh block boundaries are outlined, and the mixing plane boundary is visible between the blade rows. Naturally, the contours do not mate at the mixing plane boundary because

Mesh Block Structure:
1 Mesh Block/Blade Row (2 Mesh Blocks Total)
Mixing Plane Approximately Midway Between Blade Rows

Number of Blades in Forward Row:	**5**
Number of Blades in Rearward Row:	**5**
Design Flight Mach Number:	**0.72**
Design Power Coefficient	**2.035**
Design Advance Ratio:	**2.94**
Design Tip Speed:	**750 ft/s**
Power Loading/D2:**	**37.15**

Other Design Information:
55%/45% Torque Split (Front/Rear)
Tractor Configuration
Swept Blade Design

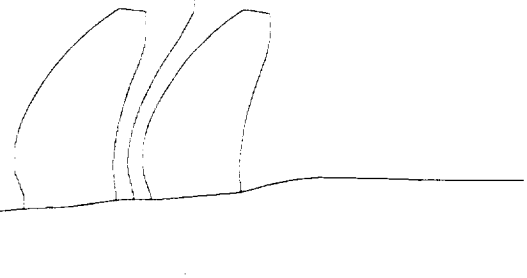

Figure 4.4: Model Counterrotating Propfan Model Geometric and Aerodynamic Design Parameters

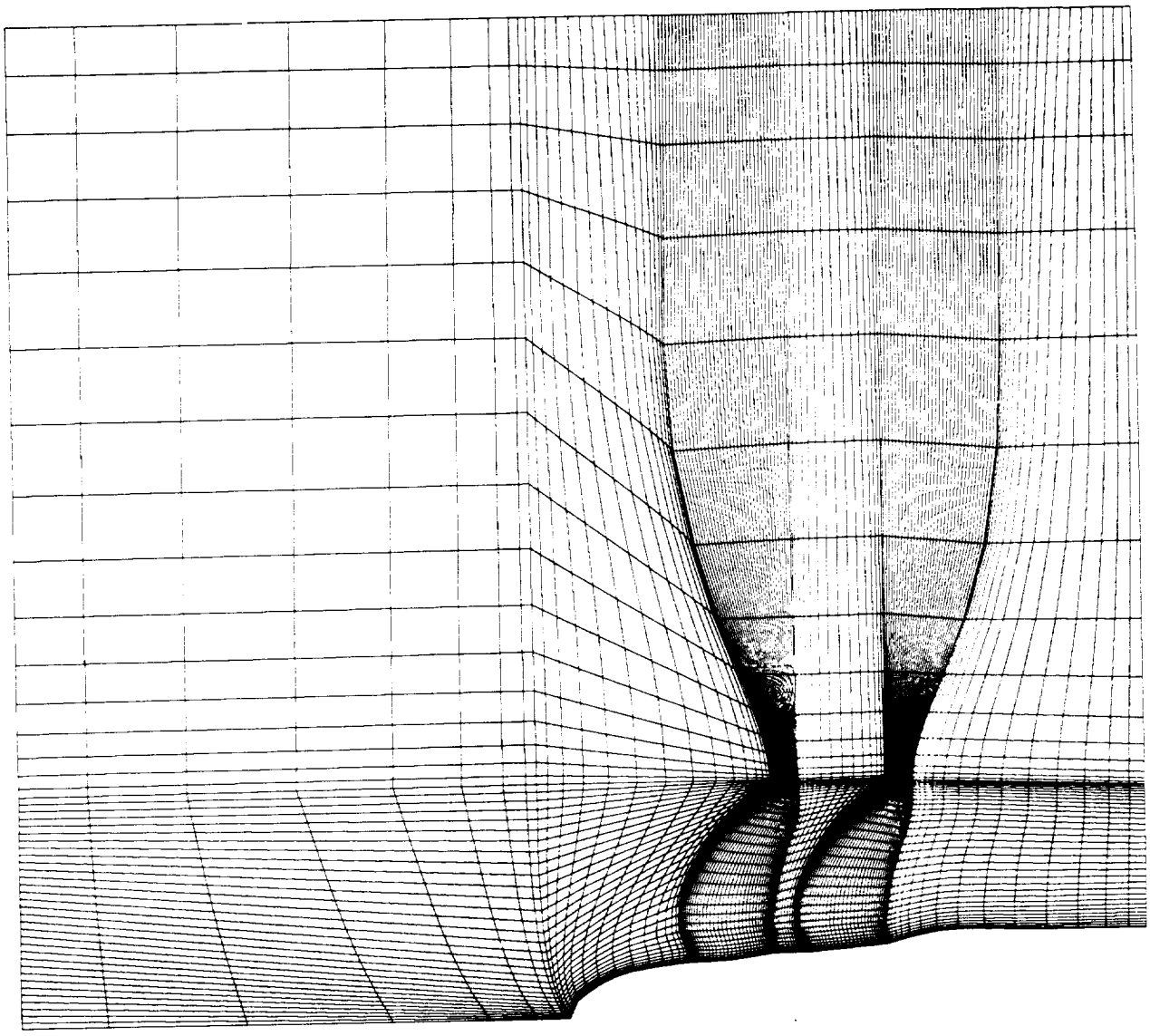

Figure 4.5: *ADPAC-AOACR* Two-Block Mesh System for Steady Flow Analysis of Model Counterrotating Propfan

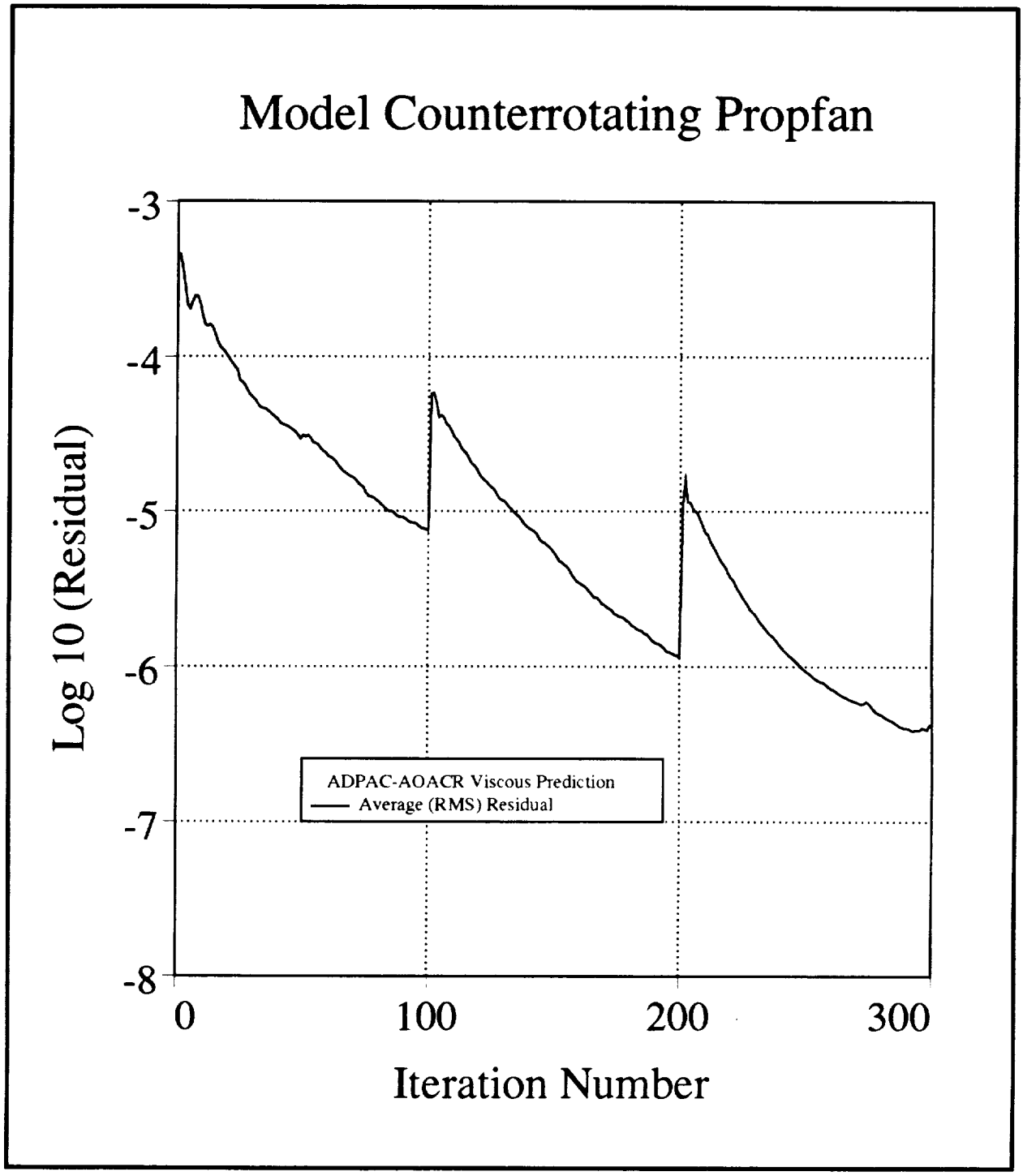

Figure 4.6: *ADPAC-AOACR* Multigrid Convergence History for Model Counterrotating Propfan Steady Flow Analysis Based on Mixing Plane Concept

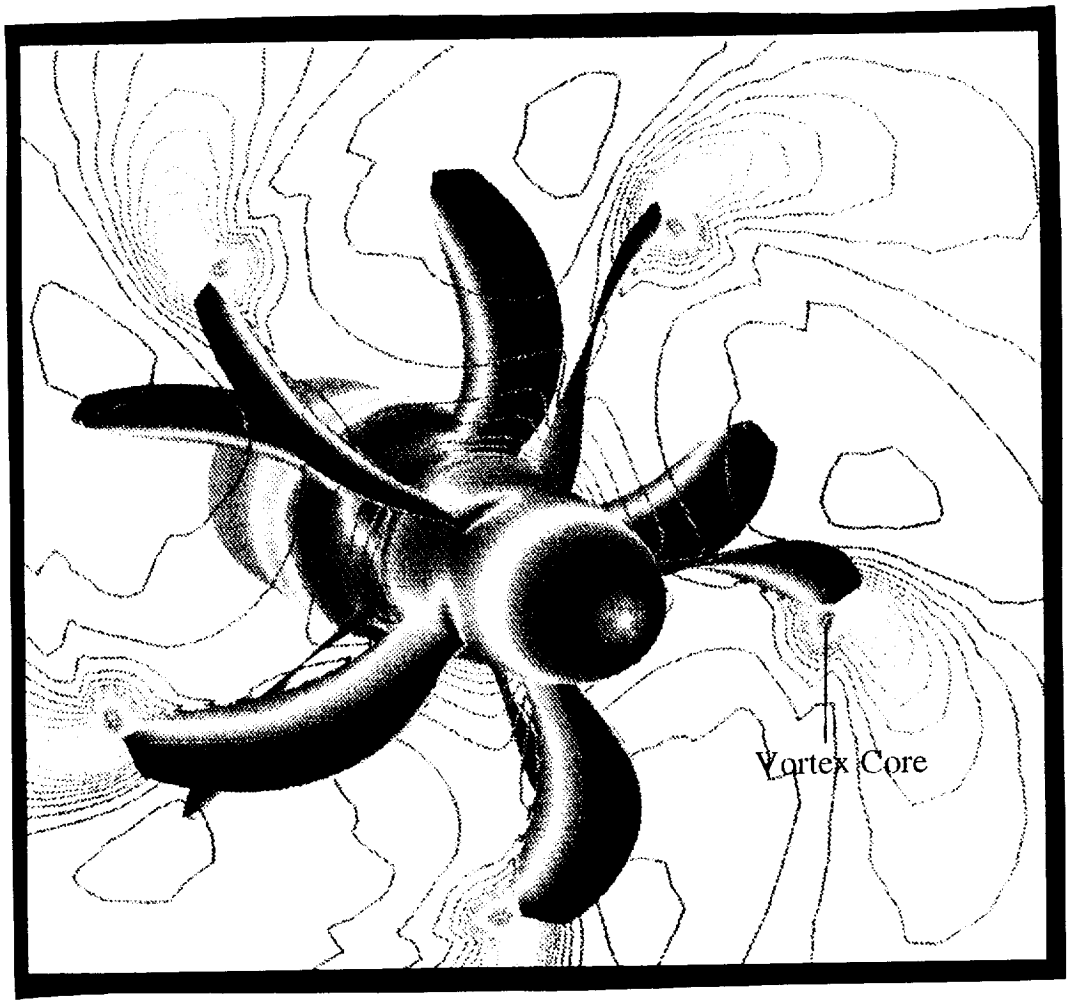

Figure 4.7: *ADPAC-AOACR* Predicted Steady Surface Static Pressure Countours and Post Rotor Static Pressure Contours for Model Counterrotating Propfan

of the circumferential averaging procedure. It is apparent, however, that the mixing plane does not unduly distort the flowfield contours in the vicinty of either blade row.

This calculation clearly demonstrates one application which can benefit from the accuracy and cost-effectiveness of the mixing plane approach. Future studies concentrating on defining the limits (in terms of interblade row spacing) would be helpful to define the geometric regime where the mixing plane assumption is valid.

4.3 NASA 1.15 Pressure Ratio Fan (Steady Flow)

In this section, calculations are presented for the viscous flow through a 1.15 pressure ratio fan stage originally tested by NASA [42]-[47] and utilized extensively under this contract for analysis [21],[7]. Descriptions of the geometry and design parameters for the NASA 1.15 pressure ratio fan are given in Fig. 4.11.

The NASA 1.15 pressure ratio fan is representative of a 25:1 bypass ratio turbofan engine fan stage, and therefore closely approximates the ducted propfan concept propulsion system. Several steady flow calculations were performed to permit a comparison of predicted results with the high speed experimental data published in Ref. [42].

A meridional view of the geometry and steady flow grid system are given in Fig. 4.12.

The steady flow calculations for this geometry were performed using the mixing plane inter-blade row model between the fan rotor and stator. It should be noted that this grid system corresponds to standard configuration #8 described in the *ADPAC-AOACR* Computer Program Users Manual (see [9]). The mesh system, illustrated in Figure 4.12, consists of 4 mesh blocks, two each associated with the rotor and the stator, respectively. The overall mesh block sizes were 89x37x33, 89x25x33, 81x37x33, and 81x25x33. The rotor was represented by 33 points in the radial direction, resulting in 5 points to define the clearance region above the rotor tip. Calculations are presented here for a flight Mach number of 0.75, and a fan rotational speed of 9167 rpm (100% speed). The calculation utilized 3 levels of multigrid and employed the full multigrid startup procedure. A total of 100 iterations were performed on each of

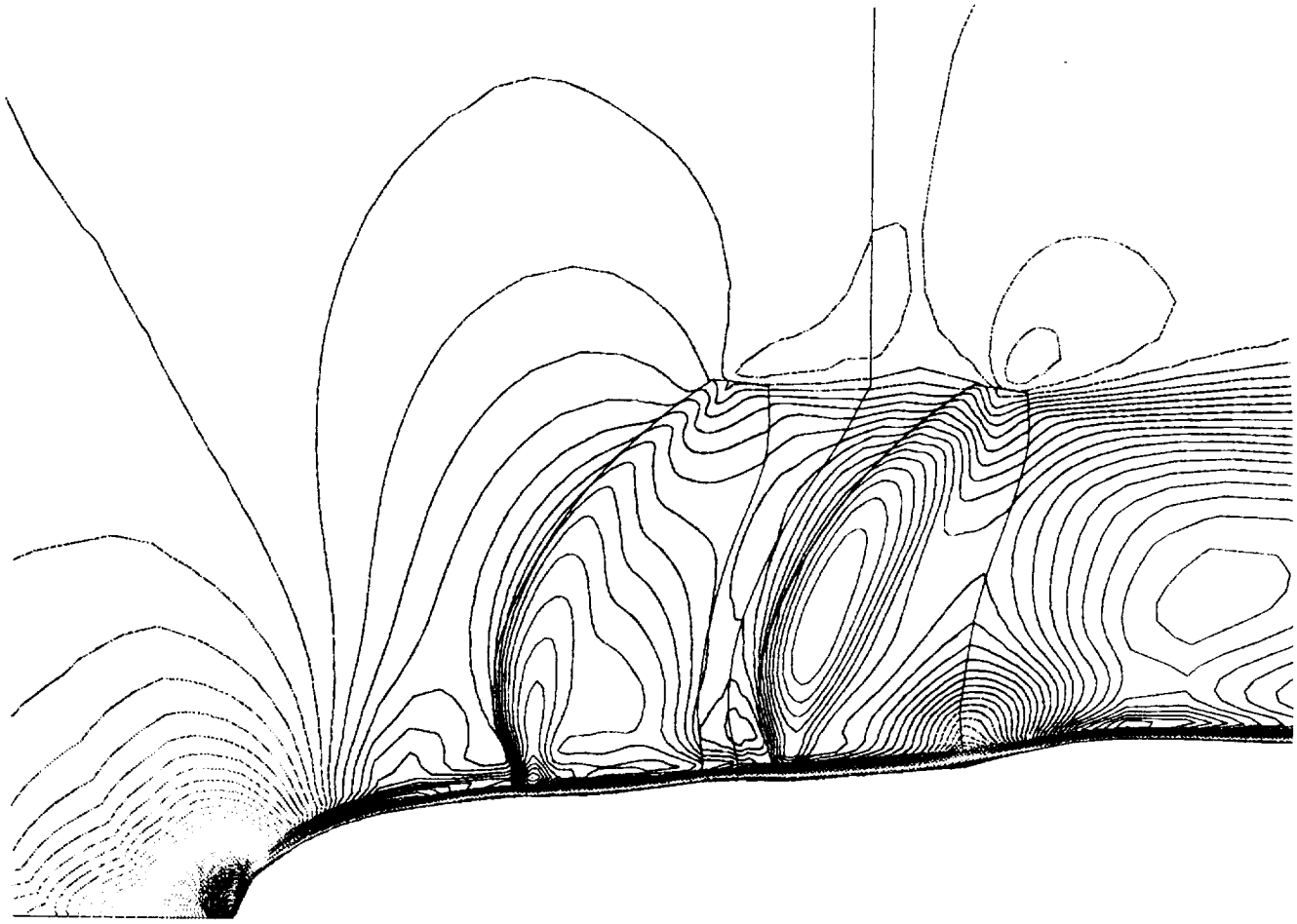

Figure 4.8: *ADPAC-AOACR* Predicted Steady Axisymmetric Averaged Mach Number Contours for Model Counterrotating Propfan

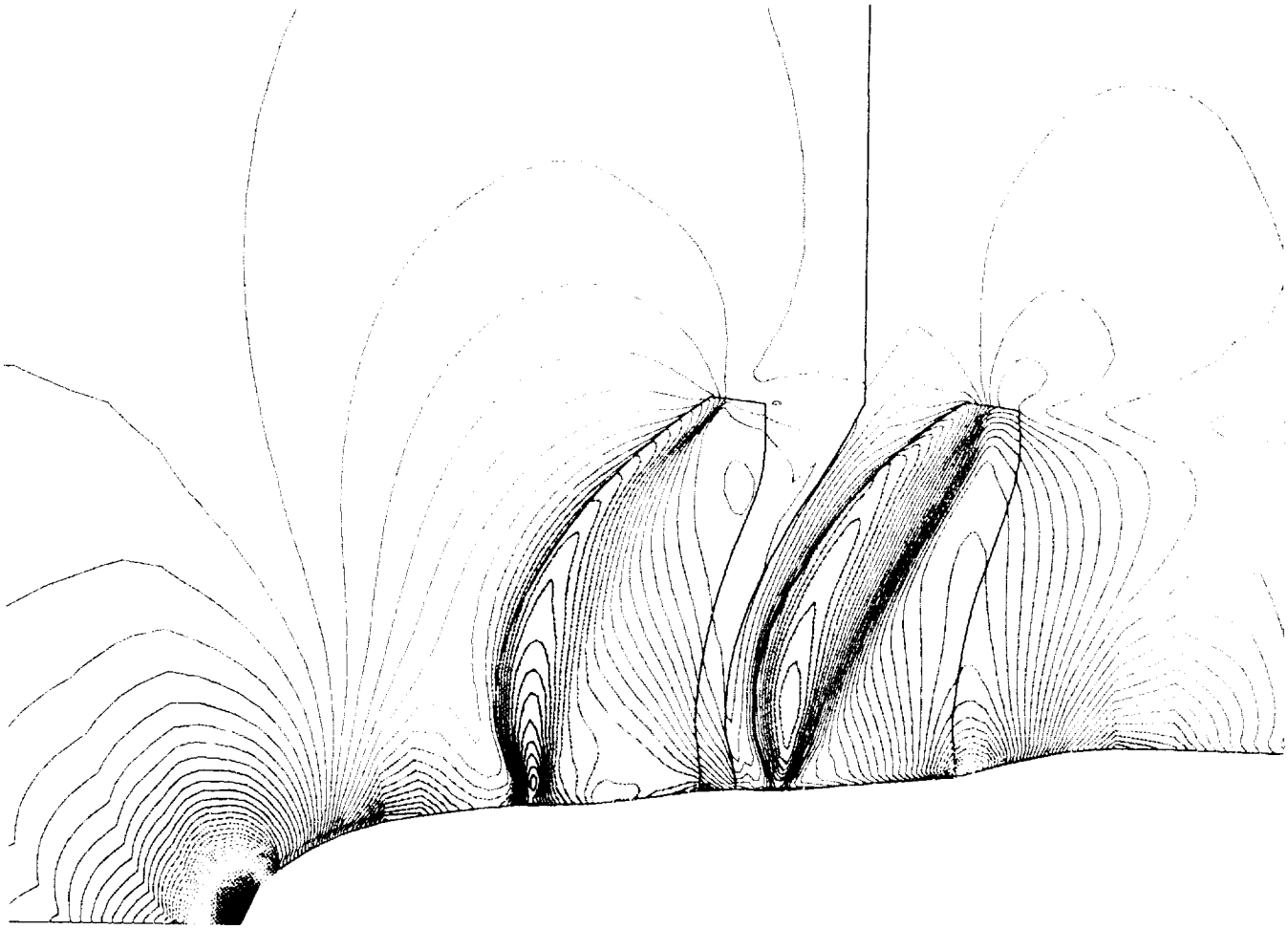

Figure 4.9: *ADPAC-AOACR* Predicted Steady Axisymmetric Averaged Static Pressure Contours for Model Counterrotating Propfan

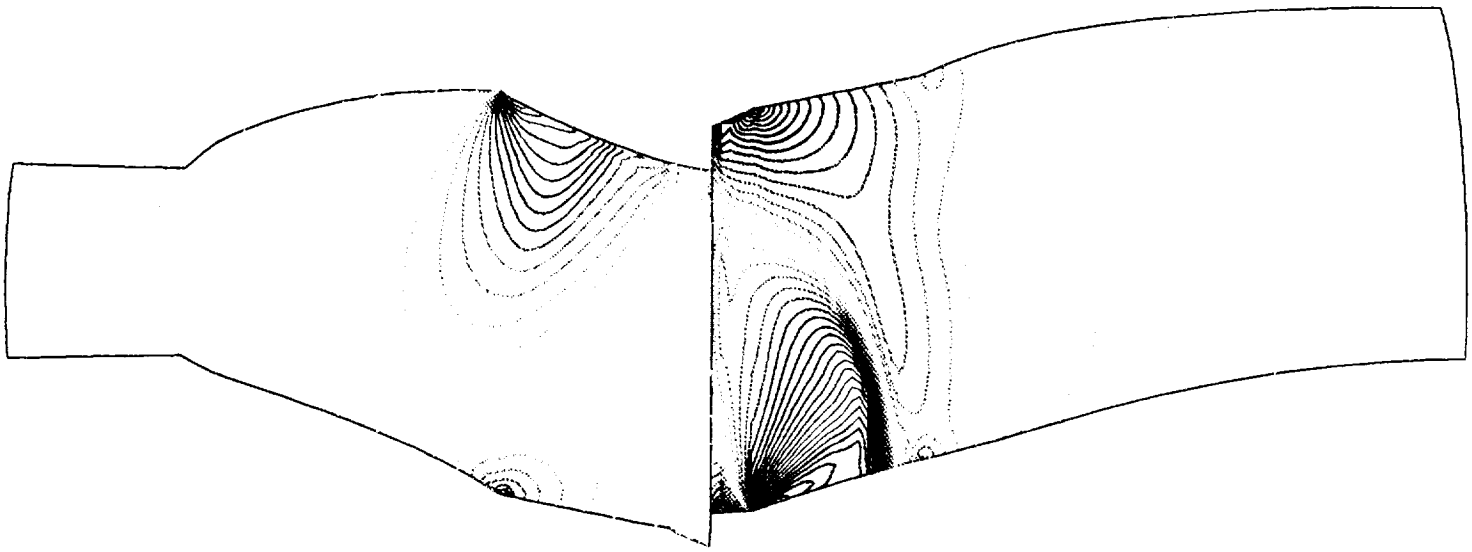

Figure 4.10: *ADPAC-AOACR* Predicted Steady Circumferential Blade-to-Blade Static Pressure Contours for Model Counterrotating Propfan

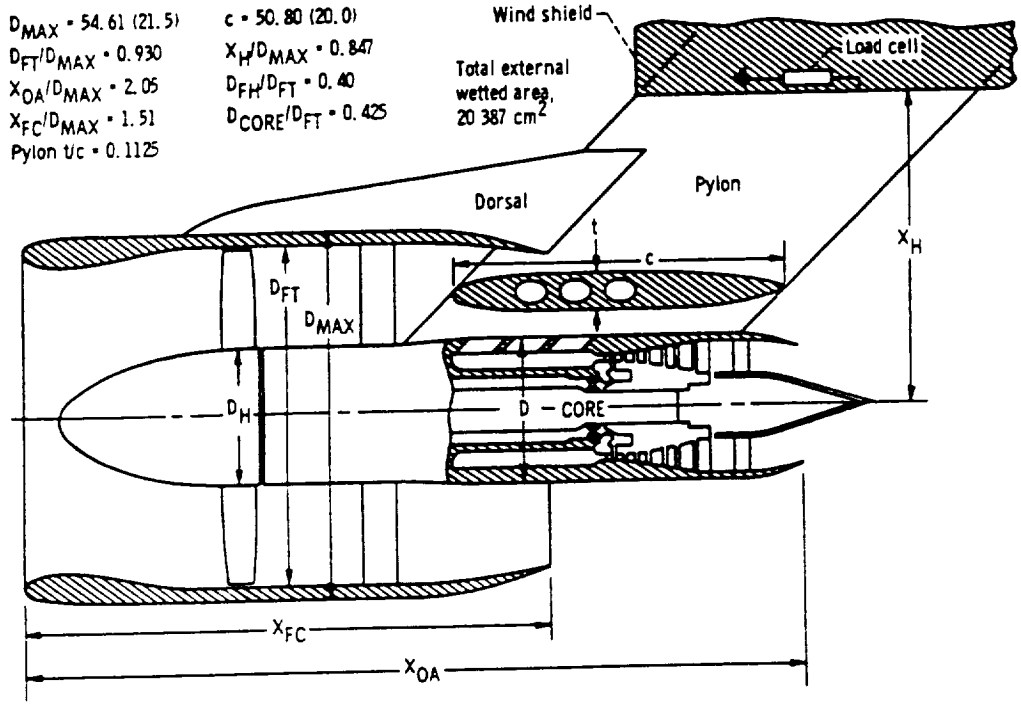

(dimensions in cm)

Figure 4.11: NASA 1.15 Pressure Ratio Fan Geometry and Design Parameters

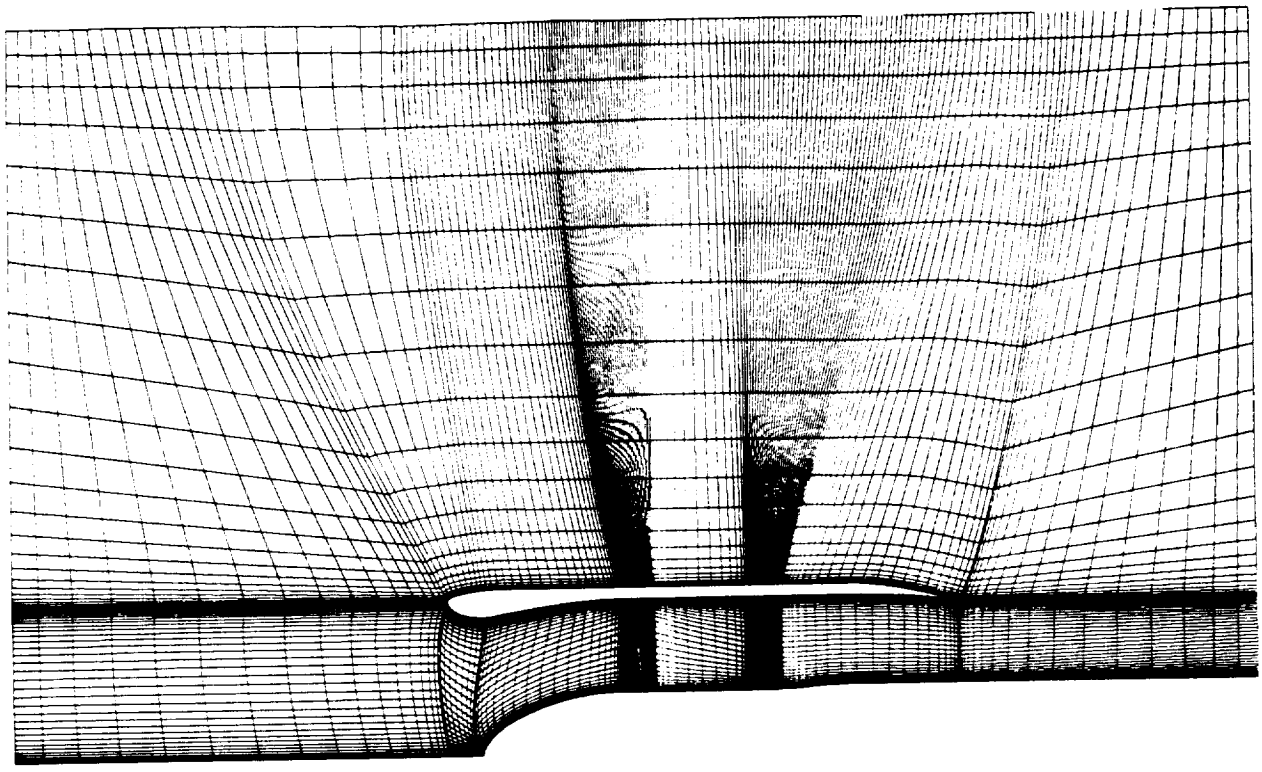

Figure 4.12: *ADPAC-AOACR* Four Block Mesh System for NASA 1.15 Pressure Ratio Fan

the coarse mesh levels during the full multigrid startup, followed by 300 iterations of the fine mesh solver.

The overall convergence of the multigrid procedure was very good for this calculation, in spite of the added complexity of the multiple block discretization and the mixing plane coupling scheme. Predicted axisymmetric averaged flow contours for absolute Mach number and static pressure are illustrated on Figures 4.13 and 4.14, respectively.

The cowl, spinner, blades, and mixing planes are outlined on both figures. The axisymmetric flow displays a smooth transition across the mixing plane, although this feature was certainly not unexpected considering the axial separation between the blade rows for this case.

A comparison of the predicted stator exit radial total pressure distribution with experimental data and numerical data obtained with the average-passage formulation developed under Task I of this contract [21] is presented in Figure 4.15. The inviscid prediction using the *HPRO3D* developed under Task 1 clearly overpredicts the total pressure ratio at the nozzle entrance as a result of the lack of viscous losses. The present prediction shows good agreement across the radial span excepet near the hub, where the *ADPAC-AOACR* results clearly underpredict the total pressure rise through the machine. This discrepency is thought to be due to numerically generated losses as a result of poor grid refinement near the spinner leading edge. These losses are ultimately convected downstream and end up showing up along the hub at the nozzle entrance. An illustration of the three-dimensional flowfield for this case is given in Figure 4.16. This figure displays predicted surface static pressure contours for a 3-D representation of the entire fan geometry, with a portion of the fan cowl cut away to expose the inner fan detail.

Additional calculations for this geometry were performed under various flow conditions (although the results will not be reported in detail here) including a supersonic flight test case at a freestream Mach number of 2.5. (In this case, the supersonic flow condition was generated by specifying an initial freestream Mach number of 2.5, and simply neglecting the application of any boundary condition at the mesh inlet, implying that the initial values are never modified, which provides a physically realistic supersonic inflow boundary treatment.) This case is mentioned only as an example

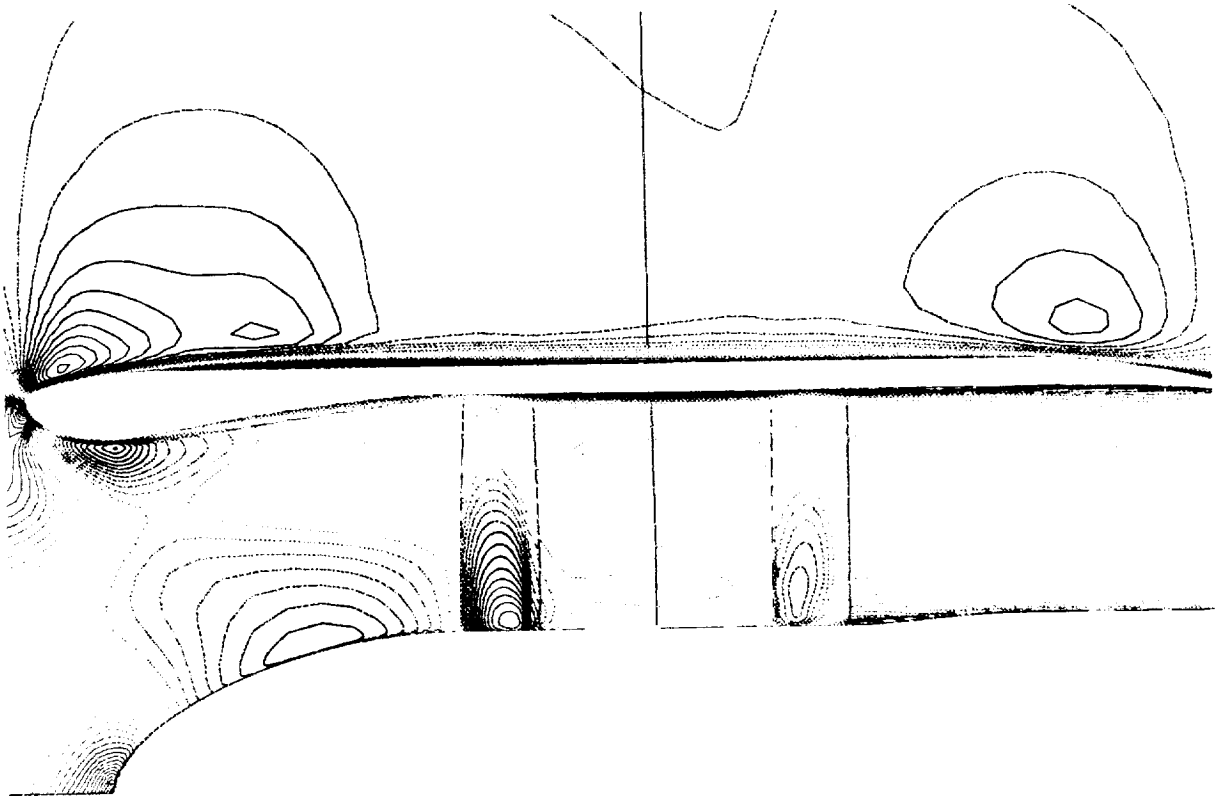

Figure 4.13: *ADPAC-AOACR* Predicted Axisymmetric Averaged Flow Absolute Mach Number Contours for NASA 1.15 Presure Ratio Fan

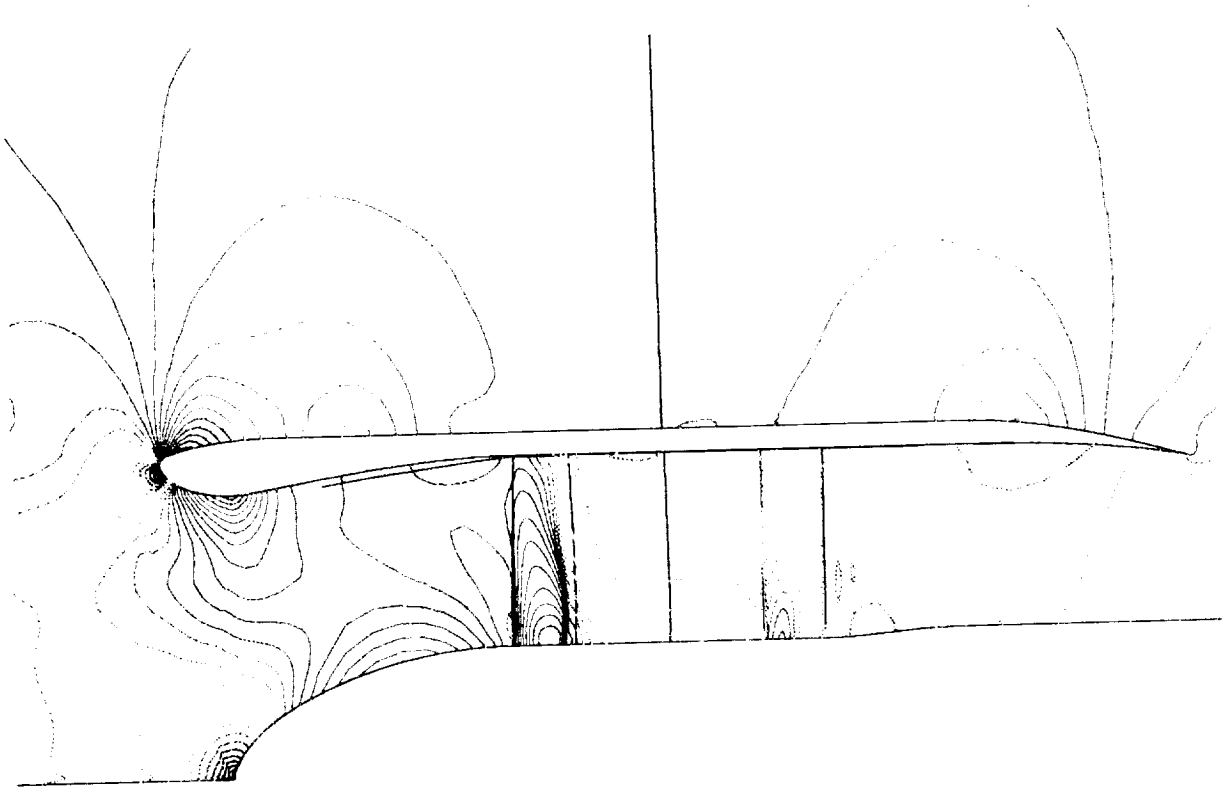

Figure 4.14: *ADPAC-AOACR* Predicted Axisymmetric Averaged Flow Static Pressure Contours for NASA 1.15 Presure Ratio Fan

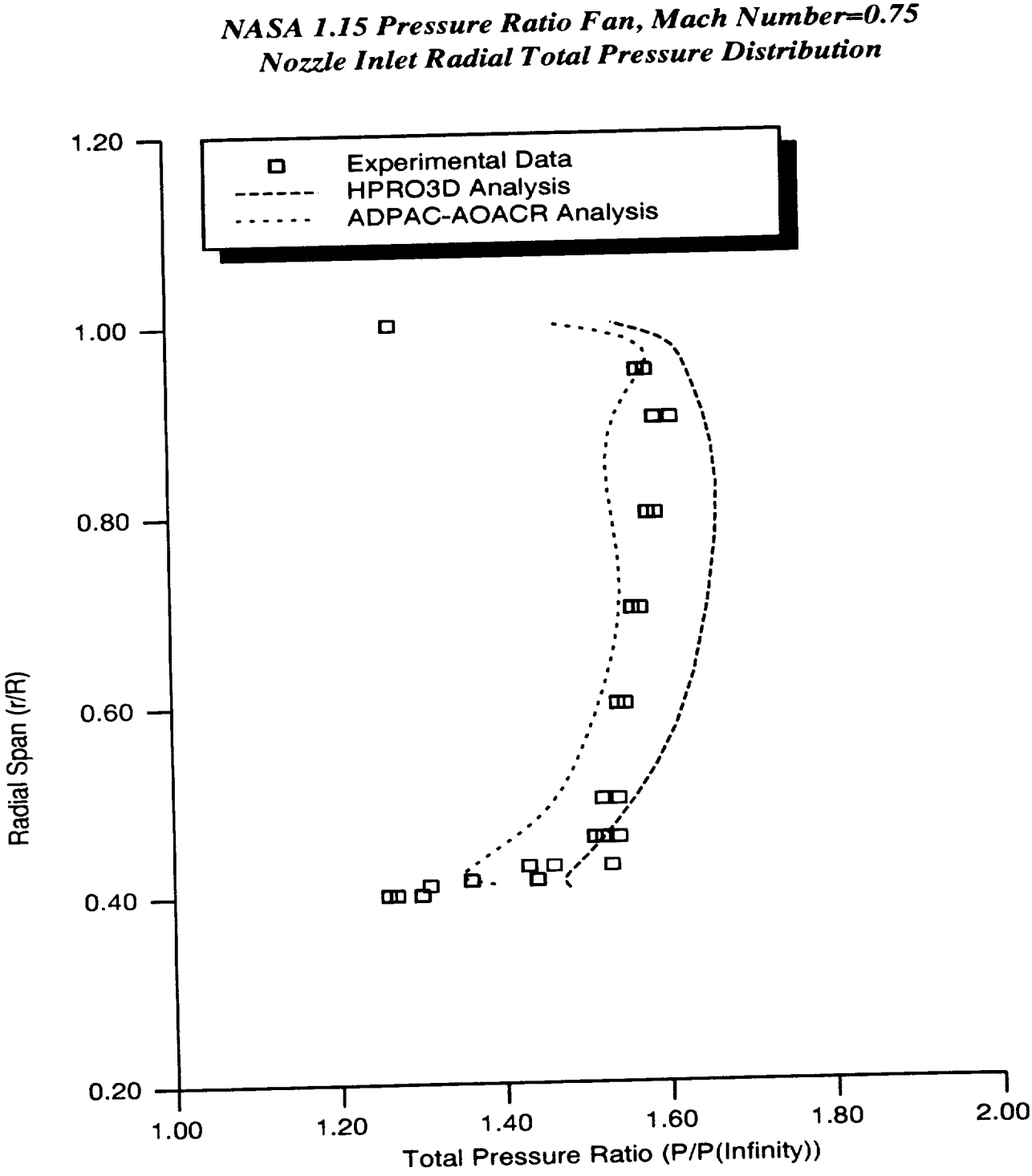

Figure 4.15: Comparison of Predicted and Experimental Stator Exit Radial Total Pressure Ratio Distribution for NASA 1.15 Pressure Ratio Fan (M=0.75)

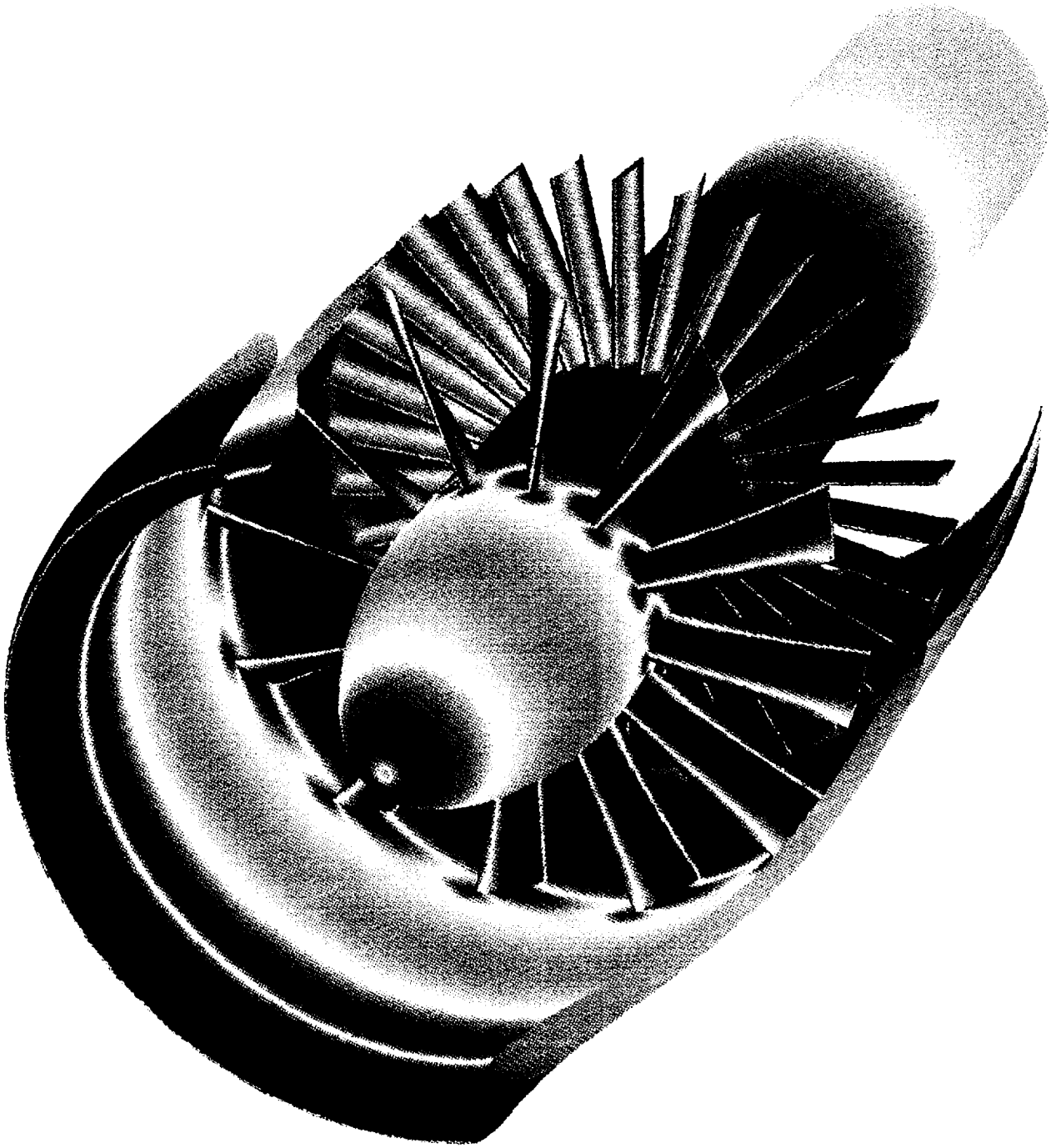

Figure 4.16: *ADPAC-AOACR* Predicted 3-D Surface Static Pressure Contours for NASA 1.15 Pressure Ratio Fan (M=0.75)

of the flexibility of the code for solving a wide variety of flow problems. In most cases tested, the multigrid procedure rapidly converged to a steady state solution (3 order of magnitude reduction in the average fine mesh residual) in less than 300 fine mesh iterations.

4.4 GMA3007 Fan Section (Steady Flow)

Steady flow verification of the *ADPAC-AOACR* code was also performed for an advanced turbofan engine fan rotor geometry taken from the Allison GMA3007 turbofan engine. The Allison GMA3007 is a 5:1 bypass ratio turbofan engine which produces 7,000 pounds of thrust. The fan section geometry considered consists of three blade rows including the fan rotor, bypass stator, and core stator. The flow is complicated by the presence of the core flow splitter, and the fact that there are multiple exits (bypass flow, core flow) for which proper boundary data must be specified. An outline of the GMA3007 fan section geometry is given in Figure 4.17. This domain was arbitrarily decomposed into three mesh blocks, as shown in Figure 4.17.

The individual mesh blocks correspond to one of the three blade rows in the fan section. For steady flow analysis, the mixing plane concept described in Section 3.2 was invoked, and therefore the circumferential pitch of each mesh block corresponds to the periodic spacing of the included blade row. In addition to the axial placement of the mixing planes between blade rows, the mesh system was designed to illustrate a radial mixing plane which separates the mesh blocks for the bypass stator (#2) and the core stator (#3) just upstream of the core flow splitter. Obviously, proper placement of the mesh block boundaries could have removed the need for this interface, but a demonstration of the radial mixing plane was thought to be justified in light of future tasks under the current contract which will utilize this type of boundary in more detail.

The actual mesh system is detailed in Figures 4.18 and 4.19. The grid block sizes were 85x73x29, 101x33x29, and 101x41x29, respectively. The grid was constructed by using the program *TIGG3D*, and special care was taken to maintain a reasonable clustering of mesh points near solid boundaries to resolve the viscous shear layers, and

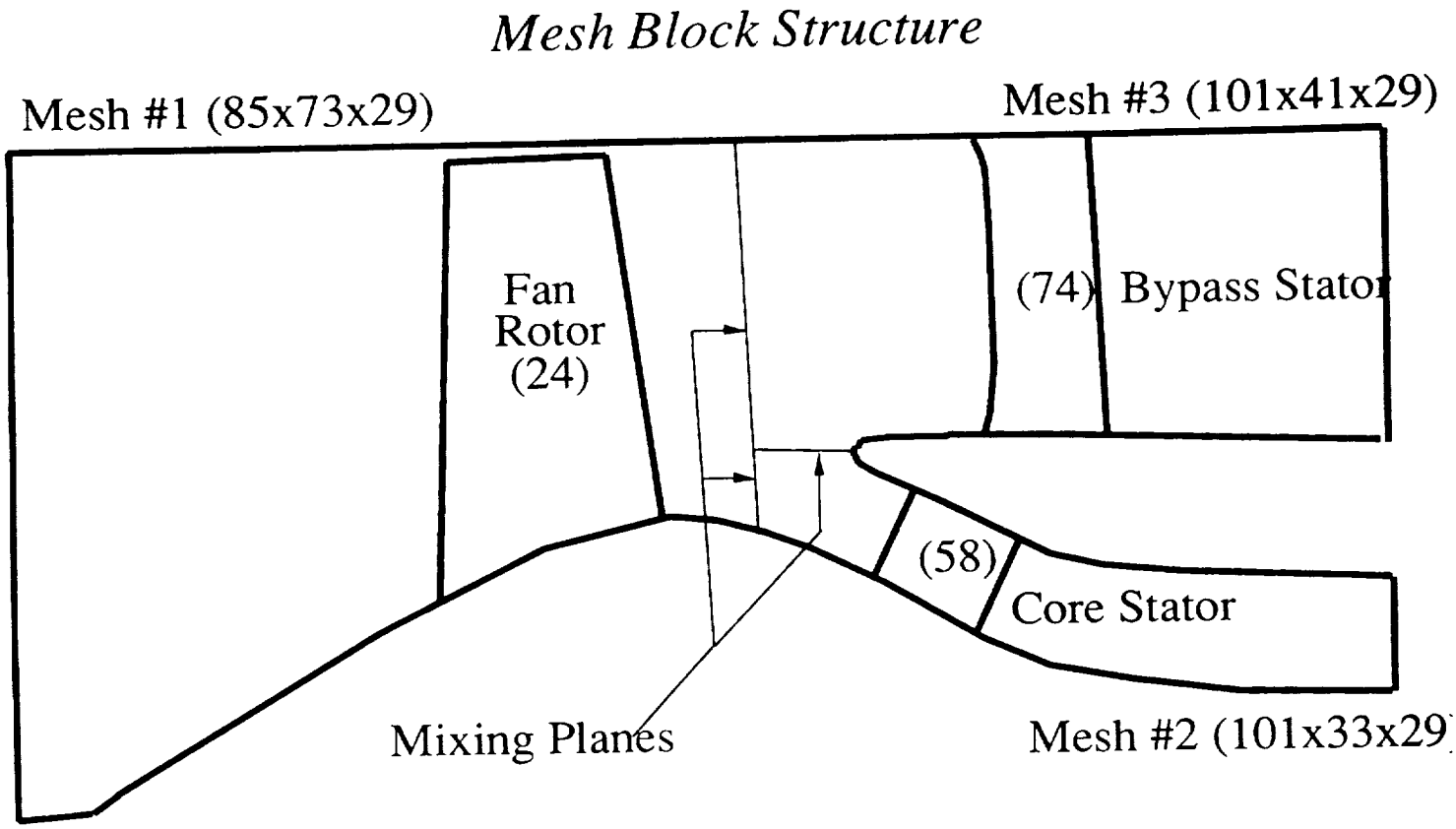

Figure 4.17: Allison GMA3007 Fan Section Geometry

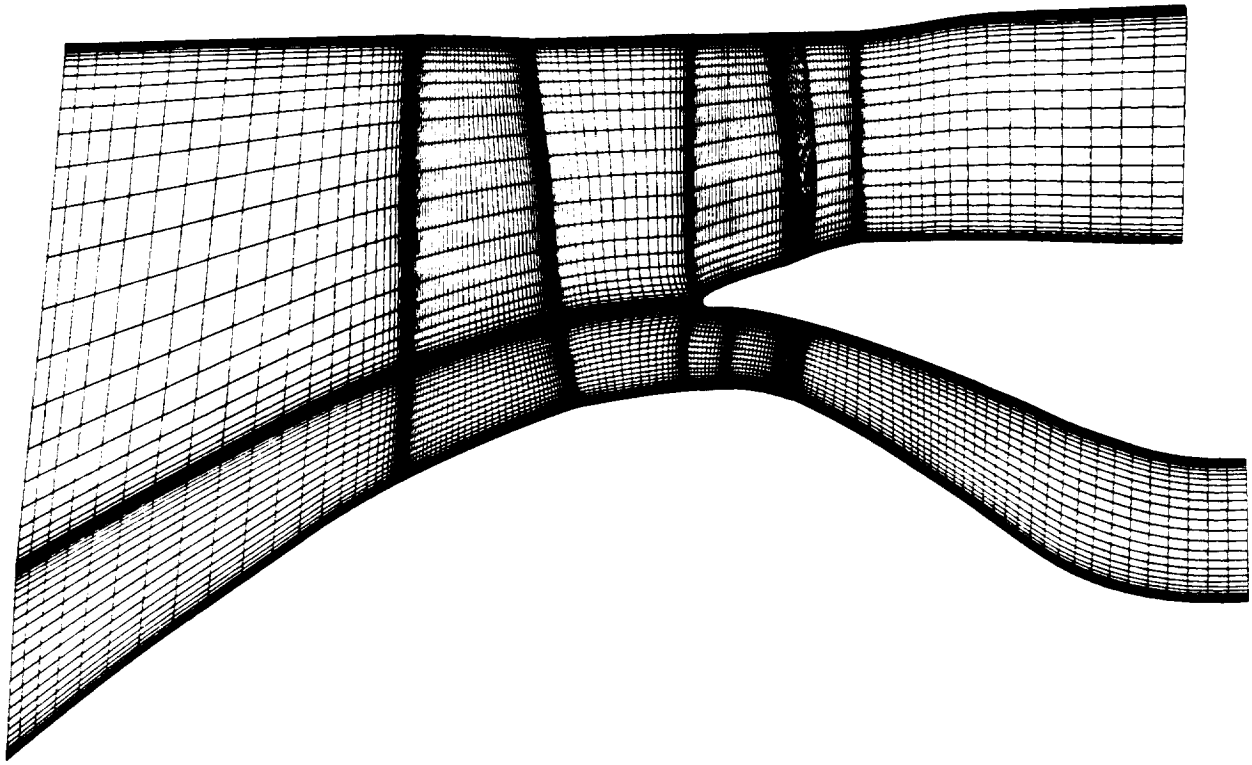

Figure 4.18: Axisymmetric Detail of *ADPAC-AOACR* Three-Block Mesh System for Allison GMA3007 Fan Section

to maintain grid indices which were compatible with the multigrid solution technique. The fan rotor includes a tip clearance region which was discretized with 9 points radially to resolve the tip clearance flow.

The numerical solution was performed using 3 levels for multigrid and was initiated with the full multigrid startup procedure. As is typical for high speed rotor flowfield calculations, the solution must be initiated at a back pressure which is lower than the intended solution back pressure. The usual procedure is to slowly raise the back pressure to the desired setting by restarting the calculation a number of times from a previous run. This procedure prevents excessive shock motion while setting up the flowfield which can prematurely cause the flowfield to stall. In this case, since there are multiple domain exit regions, following the recommended startup procedure is even more important to eliminate large oscillations in the flow split between the core and bypass ducts.

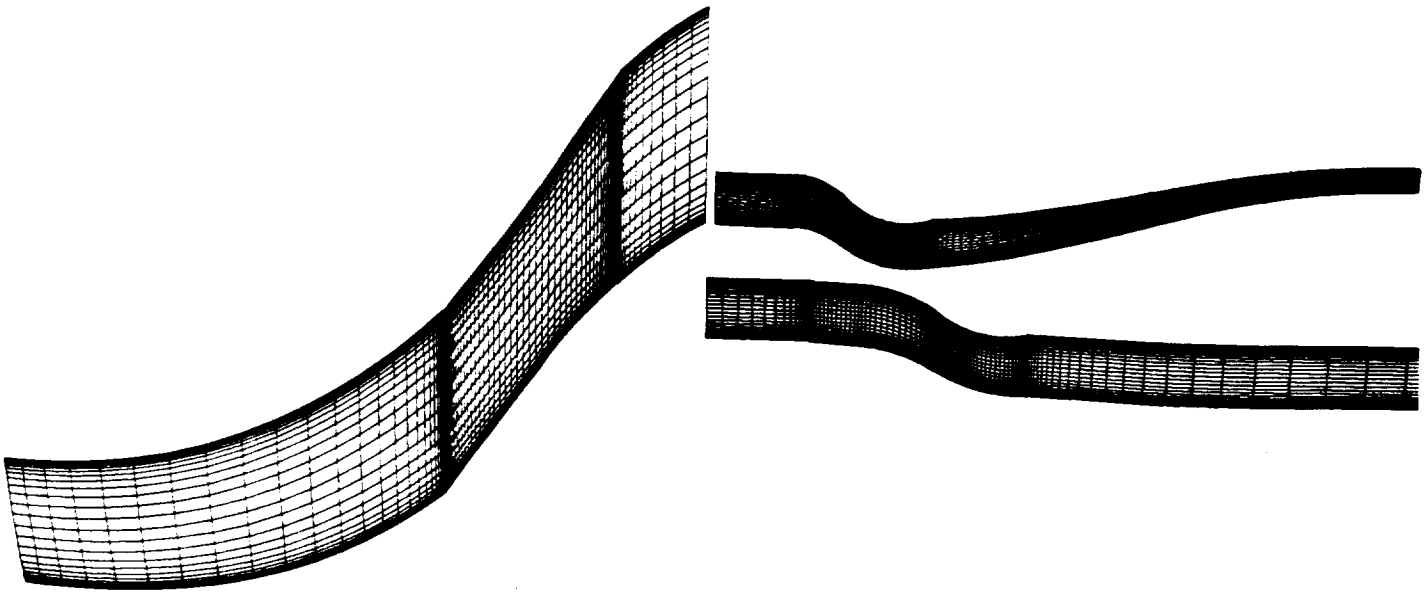

Figure 4.19: Circumferential Detail of *ADPAC-AOACR* Three-Block Mesh System for Allison GMA3007 Fan Section

Following the startup procedure described above, a design point (100% speed) solution was achieved in approximately 1500 fine mesh iterations. Experimental data were available at several points throughout this flow.

Figure 4.20 illustrates a comparison of the predicted and experimental fan rotor exit radial total pressure ratio distribution taken approximately one half chord downstream of the rotor. Predicted results from several other calculations for this geometry are also included on this Figure to illustrate the accuracy of the *ADPAC-AOACR* code compared with other analyses. It should be mentioned that some slight differences in operating condition (mass flow rate, etc.) existed between the various predictions displayed on this figure, which is at least partially responsible for the differences in the results. The *ADPAC-AOACR* results are clearly in good agreement with the experimental data at this point, and is at least as accurate as any other analysis which has been tested for this geometry to date. An interesting observation from this result is that the *ADPAC-AOACR* prediction is in good agreement with the *ADPAC-APES* code, which was also developed under this contract, and which utilizes the more complicated average-passage solution scheme for multiple blade row

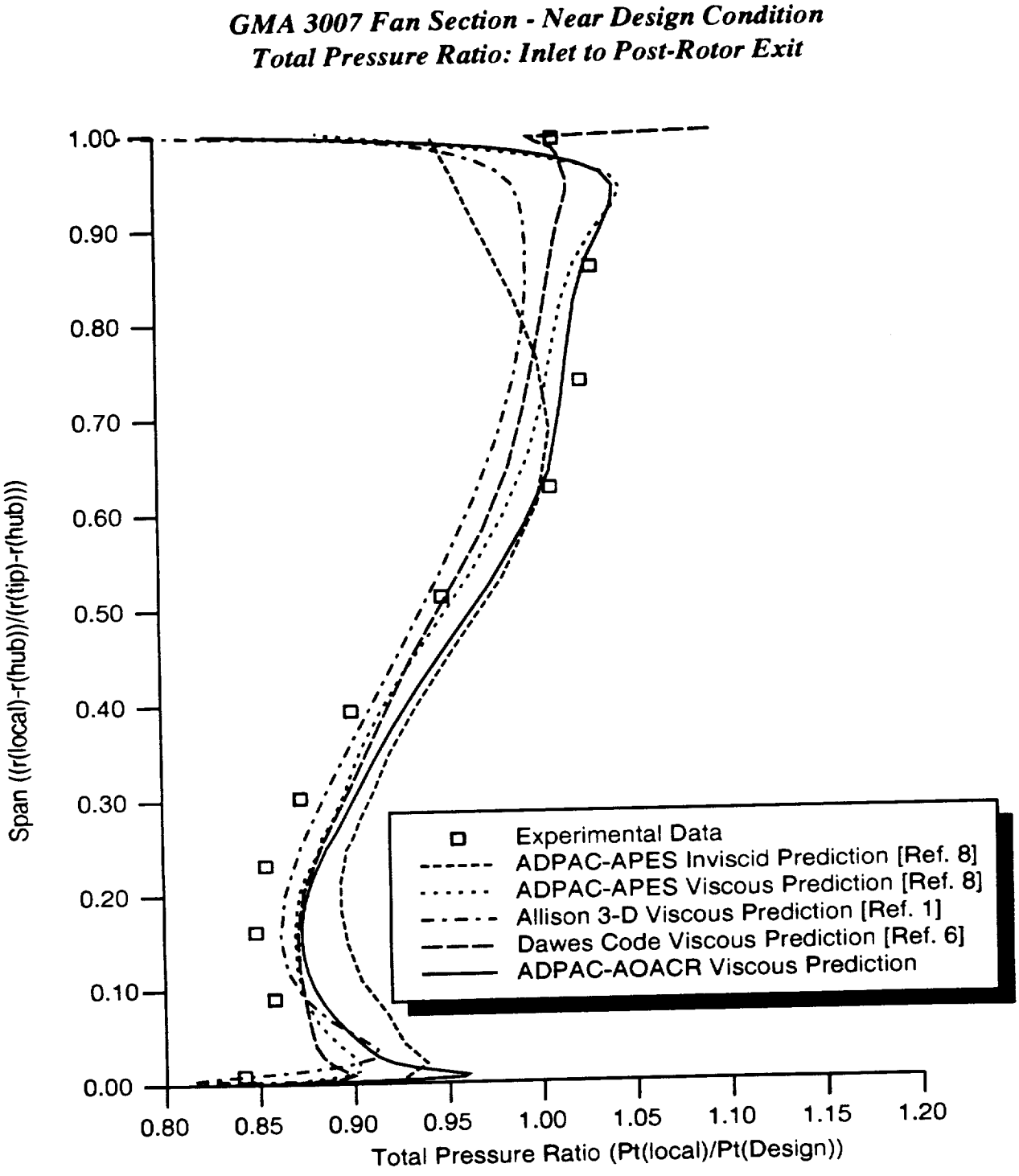

Figure 4.20: Comparison of Predicted and Experimental Radial Total Pressure Ratio Distributions Downstream of Fan Rotor for Allison GMA3007 Fan Section

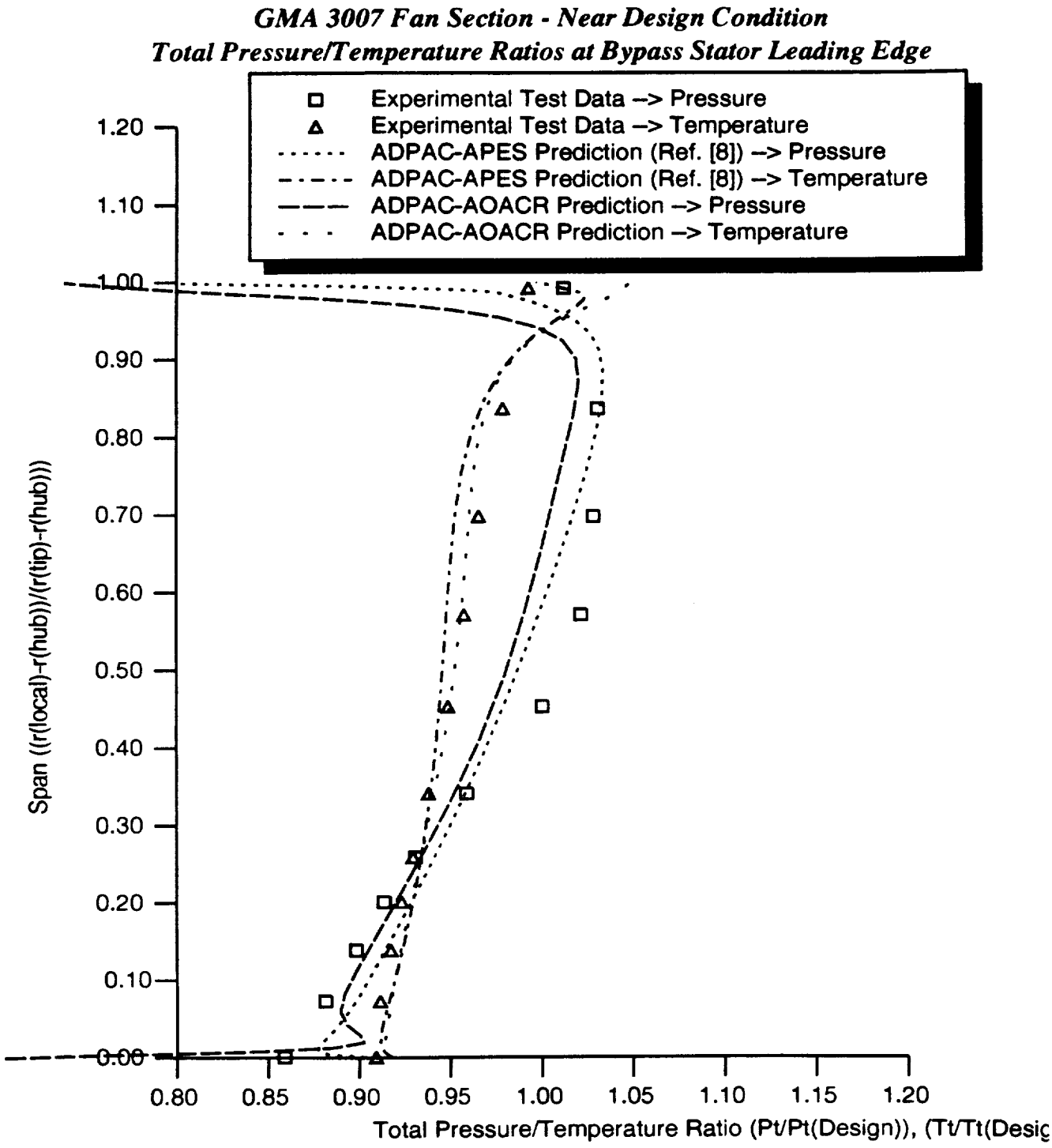

Figure 4.21: Comparison of Predicted and Experimental Radial Total Pressure and Total Temperature Ratio Distributions at Bypass Vane Leading Edge for Allison GMA3007 Fan Section

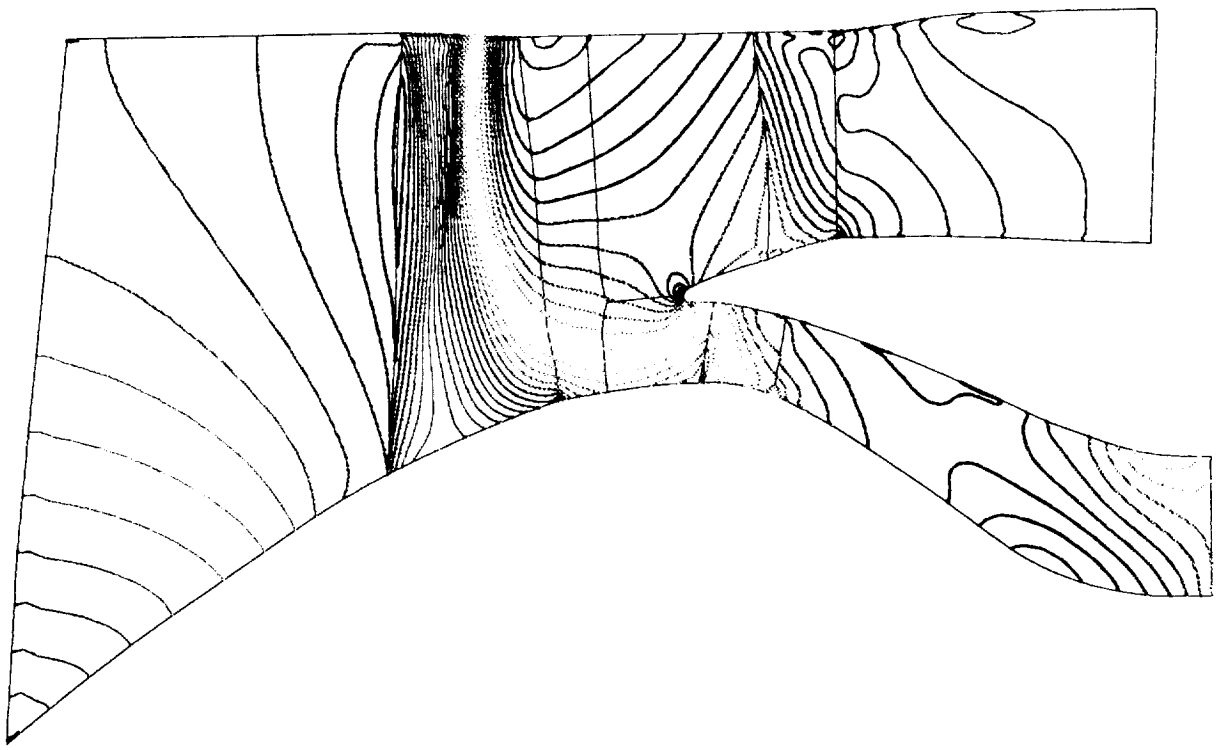

Figure 4.22: Predicted Axisymmetric-Averaged Static Pressure Contours for Allison GMA3007 Fan Section

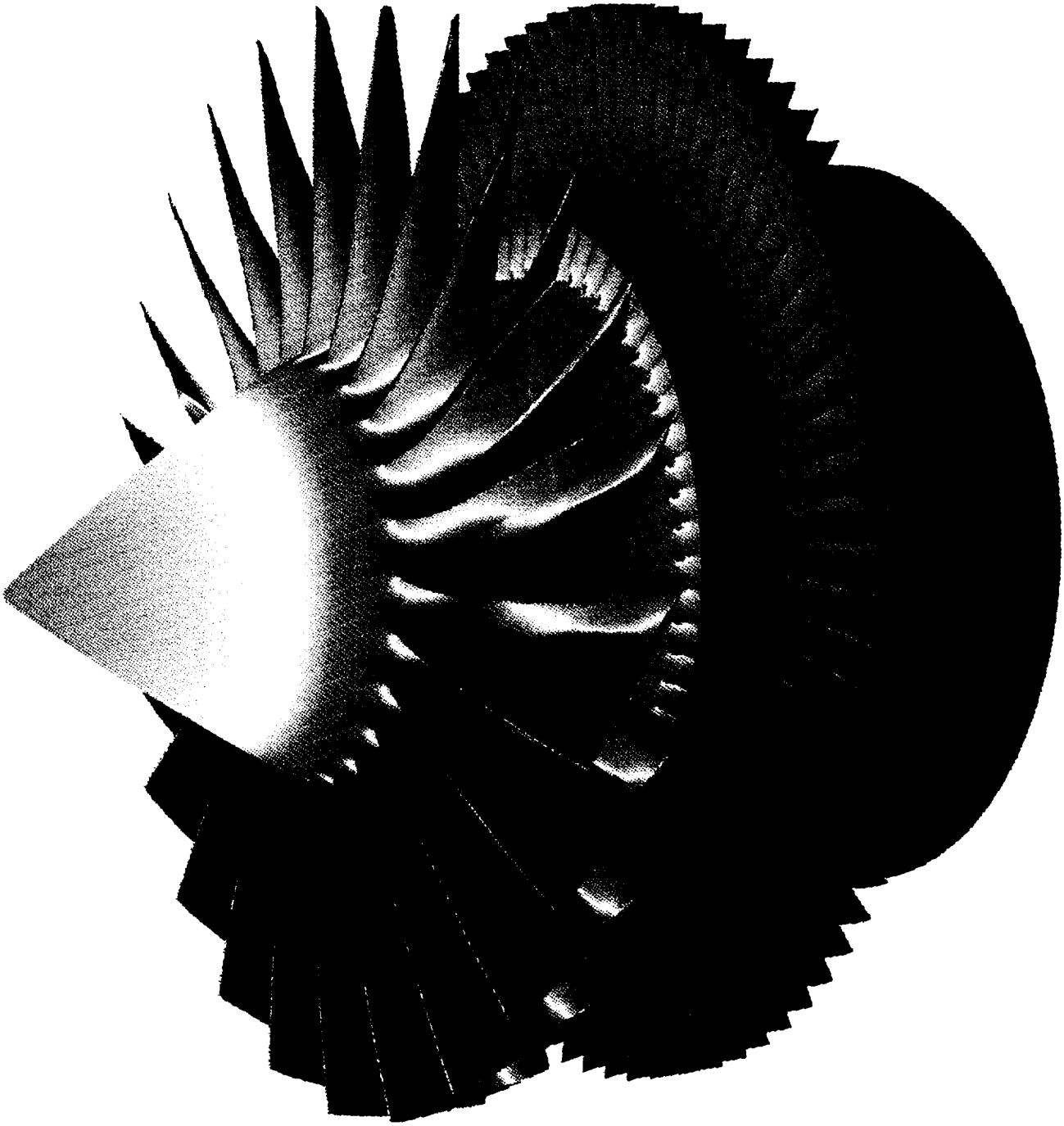

Figure 4.23: Predicted Surface Static Pressure Contours for Allison GMA3007 Fan Section

turbomachines. One would expect that the average-passage equation system provides a more accurate model for steady flow analysis of interblade row interactions than the simpler mixing plane concept; however, the large axial spacing between blade rows in this turbomachinery geometry suggests that this advantage is likely to be less influential, and the good agreement between predictions supports this observation. A similar comparison of the predicted and experimental bypass stator leading edge radial total pressure and total temperature distributions is given on Figure 4.21. Once again, the *ADPAC-AOACR* results are in good agreement with the average passage prediction for this geometry.

An illustration of the predicted axisymmetric-averaged static pressure contours for this calculation are presented in Figure 4.22. The stagnation region around the core flow splitter is clearly defined, and it is clear that there is some slight negative incidence in the vicinity of the splitter leading edge. This incidence is clearly dependent on the exit pressure chosen for both the core flow and bypass flow domains, and our experience has been that the solution is relatively sensitive to small changes in either specification.

Finally, to illustrate the three-dimensional nature of this flowfield, an illustration of the predicted static pressure contours for a complete representation of the GMA3007 fan section is given in Figure 4.23. The contours clearly display the rotor shock location, and the flowfields associated with the core and bypass stators. The complexity of this figure demonstrates the capability of the *ADPAC-AOACR* code to analyze complex, realistic turbofan engine flowfields.

4.5 Oscillating Flat Plate Cascade (Unsteady Flow)

Before proceeding with a discussion of time-dependent predictions for multiple blade row turbomachines, a demonstration of the time-accuracy of the *ADPAC-AOACR* solution procedure seems appropriate. A numerical study was performed involving the time-dependent flowfield about an oscillating flat plate cascade. This calculation serves to further verify the time accuracy of the *ADPAC-AOACR* code, and can provide some insight into the possibility of utilizing nonlinear time-marching numerical solution techniques for the prediction of blade motion induced acoustic

phenomena in turbomachinery components. A detailed discussion of calculations of this type was recently presented by Huff [45], and these results were used to guide the present calculations.

The calculation was based on a zero stagger flat plate cascade with a pitch to chord ratio of 1.0. The cascade motion was represented by a pitchwise plunging harmonic oscillation. This configuration is illustrated in Figure 4.24. The cascade motion was programmed into the *ADPAC-AOACR* code by temporarily incorporating a time-varying blade rotation term. The solution was initiated from a steady, uniform flowfield, and advanced in time under the influence of the harmonic blade motion, until a time-periodic solution was achieved. Calculations were performed on both a fine and coarse mesh system for a reduced frequency of 4.0 (defined as

$$k = \frac{\omega c}{(2V_1)} \tag{4.1}$$

where k is the reduced frequency, ω is the harmonic oscillation frequency, c is the flat plate chord, and V_1 is the freestream velocity. The freestream flow Mach number was 0.5. The amplitude of the cascade vibration was 0.1% of the blade chord. The mesh systems were actually based on a 2-D grid system generated by personnel at the NASA-Lewis Research Center, which was stacked radially to construct a 3-D mesh system. The 3-D mesh system was constructed with a hub to tip ratio of 0.996 and a radius to chord ratio of 100.0, which were believed to be sufficient to minimize radial flow gradients and non-planar flow features resulting from the use of a cylindrical coordinate system.. The coarse grid was decomposed from the fine grid by eliminating every other grid line. An illustration of the blade-to-blade component of both mesh systems is given in Figure 4.25.

The fine mesh size was 121x5x41, while the coarse mesh was 61x5x21 (the radial distribution of mesh nodes is kept low (5) since the flow is essentially two-dimensional (no radial flow gradients)). The calculations were advanced over approximately 25 cycles of the plunging cascade oscillation using a constant CFL number of 1.0. The calculation was performed on an IBM RS6000 Model 540 workstation and required approximately 28 hours (estimated) to complete the fine mesh solution. The time-periodicity of the solution at this point was verified by comparing local static pressure time-histories at several points along the cascade surface and verifying that the local

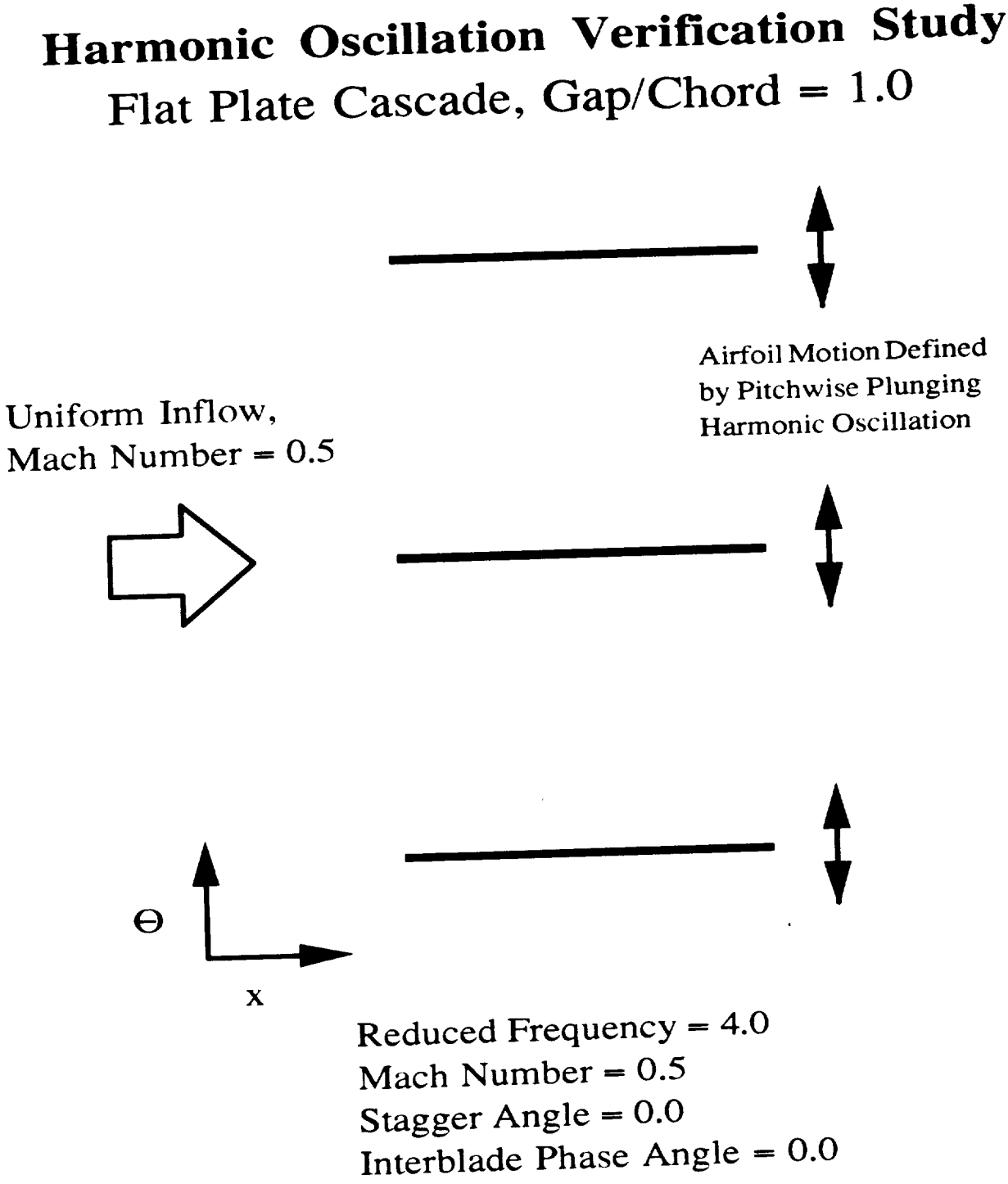

Figure 4.24: Oscillating Flat Plate Cascade Geometry

GEOMETRY

Flat Plate Cascade Harmonic Oscillation Study

Coarse Mesh (61x5x21 --> axial, radial, circumferential)

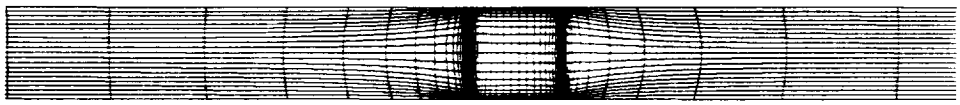

Fine Mesh (121x5x41 --> axial, radial, circumferential)

Inflow

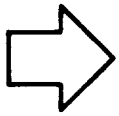

Outflow

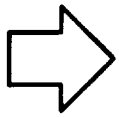

- 2–D Grids Stacked to Form 3–D Grid
- 1 Grid Forms Cascade
  (Zero Interblade Phase Angle Only)

Figure 4.25: Oscillating Flat Plate Cascade Blade to Blade Mesh Systems

pressure was periodic with respect to the known oscillation frequency. During the calculation, time histories of the local circumferential static pressure differential across the flat plate airfoils were stored. This static pressure differential, defined as

$$\Delta p(x,r) = p(x,r,\theta) - p(x,r,\theta + \Delta\theta) \tag{4.2}$$

where $\Delta\theta$ is the cascade pitch, is representative of the instantaneous local aerodynamic loading on the plate surface. The final cycle of these time histories was decomposed into a Fourier series, and the first harmonic component of the Fourier series was then plotted as real and imaginary components of the plate pressure differential response to the cascade motion. The predicted real and imaginary components of the flat plate pressure differential response are illustrated in Figures 4.26and 4.27. Note that the response is illustrated in terms of a pressure coefficient as:

$$\Delta C_p = \frac{\Delta p}{\rho v_1^2 hk} \tag{4.3}$$

where h is the amplitude of oscillation.

The predicted results were compared with results from the linear theory presented by Smith [44]. The comparison of the real and imaginary components for the plate pressure differential response given in Figures 4.26 and 4.27 includes both coarse and fine mesh *ADPAC-AOACR* Euler predictions and the Smith results. This comparison clearly suggests reasonable agreement with the linear theory, except in the vicinity of the leading edge, where nonlinear effects could be more important, in which case the linear theory is likely to be less accurate. Due to a lack of time, no specific measures were taken (such as reducing the amplitude of oscillation) to evaluate the magnitude of this apparent nonlinear behavior. The predicted results demonstrated a marked improvement in the correlation with the Smith results with increased grid resolution. One benefit of the present mesh system is that the results are likely to be fairly insensitive to inlet or exit boundary conditions It should be observed that the present calculations are likely to be relatively insensitive to the inflow/outflow boundary conditions as a result of the coarsening of the axial mesh spacing away from the flat plate cascade. This coarsening effectively damps out the unsteady waves in the farfield and minimizes nonphysical reflections from the far field boundaries.

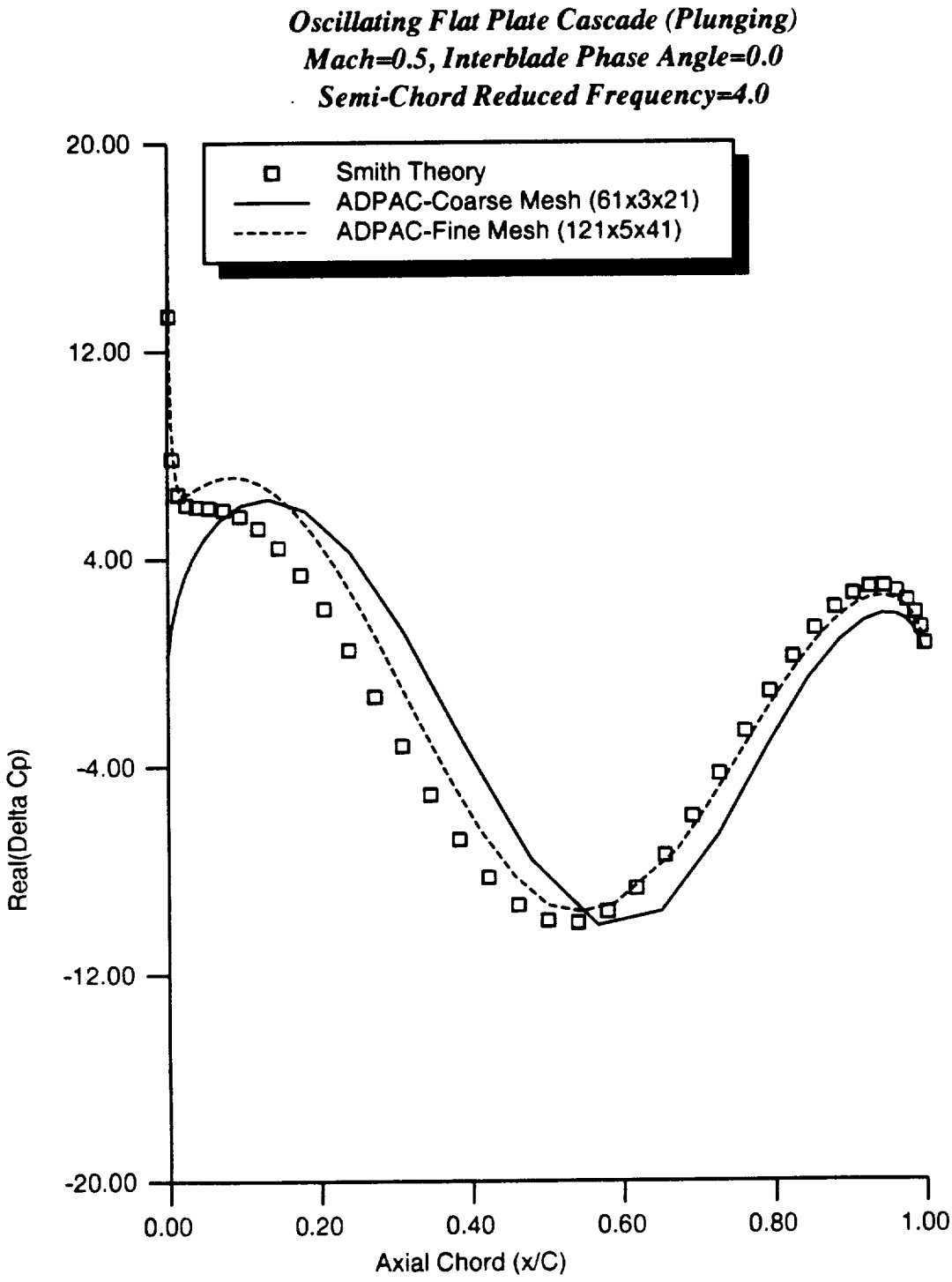

Figure 4.26: Comparison of *ADPAC-AOACR* Prediction and Smith Linear Theory for Real Component of Airfoil Surface Pressure Response for the Oscillating Flat Plate Cascade Test Case

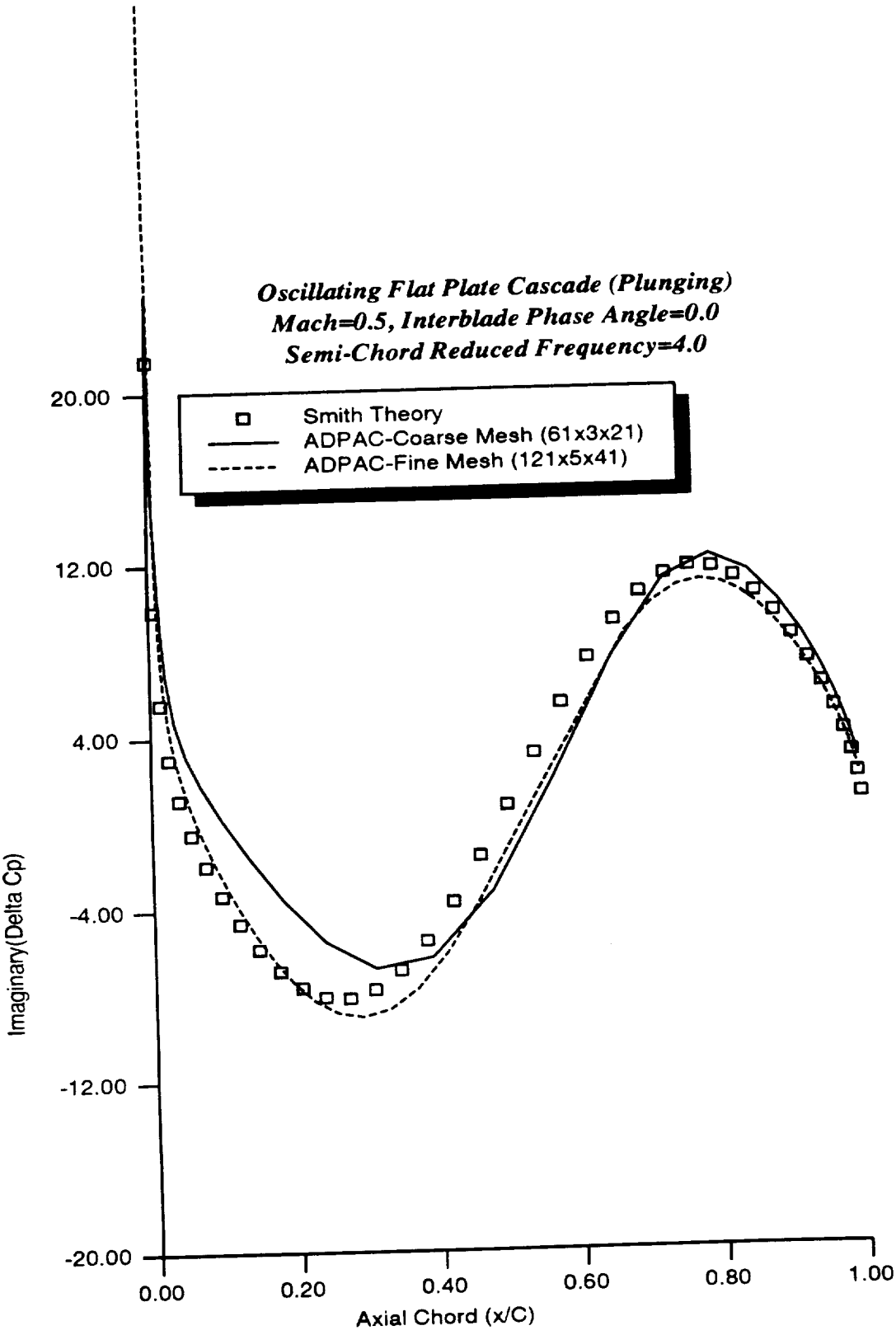

Figure 4.27: Comparison of *ADPAC-AOACR* Prediction and Smith Linear Theory for Imaginary Component of Airfoil Surface Pressure Response for the Oscillating Flat Plate Cascade Test Case

C-2

Additional details on the effects of mesh coarsening and inflow/outflow boundary treatments are detailed in Ref. [45].

It is recommended that additional calculations of this type be performed in the future for more complicated flow cases, and mesh systems involving multiple blocks to analyze the influence of the interblock communication boundary conditions on the unsteady flow results.

4.6 SR7 Unducted Propfan - Cylindrical Post Interaction Study (Unsteady Flow)

In this section, an application of the *ADPAC-AOACR* program to predict the time-dependent flowfield resulting from the aerodynamic interaction between a stationary cylindrical post and a rotating unducted propfan is described. These results represent the first presentation of the time-dependent multiple blade row flow analysis capability of the *ADPAC-AOACR* program. The flow conditions for this case were based on results from the experimental study described by Bushnell et al. [40]. Bushnell presents wind tunnel measurements of a single rotation propfan mounted behind a stationary cylindrical post. The purpose behind this study was to determine the effect of the interaction between the wake from the cylindrical post and the rotating propfan airfoil. The experimental configuration is shown diagramatically in Figure 4.28. The propfan design utilized in this study was based on the SR7 propfan. Geometric and aerodynamic design parameters for the original SR7 propfan are given in Figure 4.29.

The experimental measurements included steady state airfoil static pressure data, and time-dependent airfoil static pressure data resulting from both angle of attack, and the unsteady interaction with the cylindrical post. The steady state and experimental pressure data locations are given in Figure 4.30.

Because of wind tunnel power limitations, the number of propfan blades used in the experimental study was reduced from 8 (the original SR7 design blade count) to 2. This reduction in blade count resulted in a fortuitous simplification in the numerical analysis of the unsteady interaction between the post and the rotating propfan. Since the effective blade count for the propfan and the cylindrical post are identical (in this

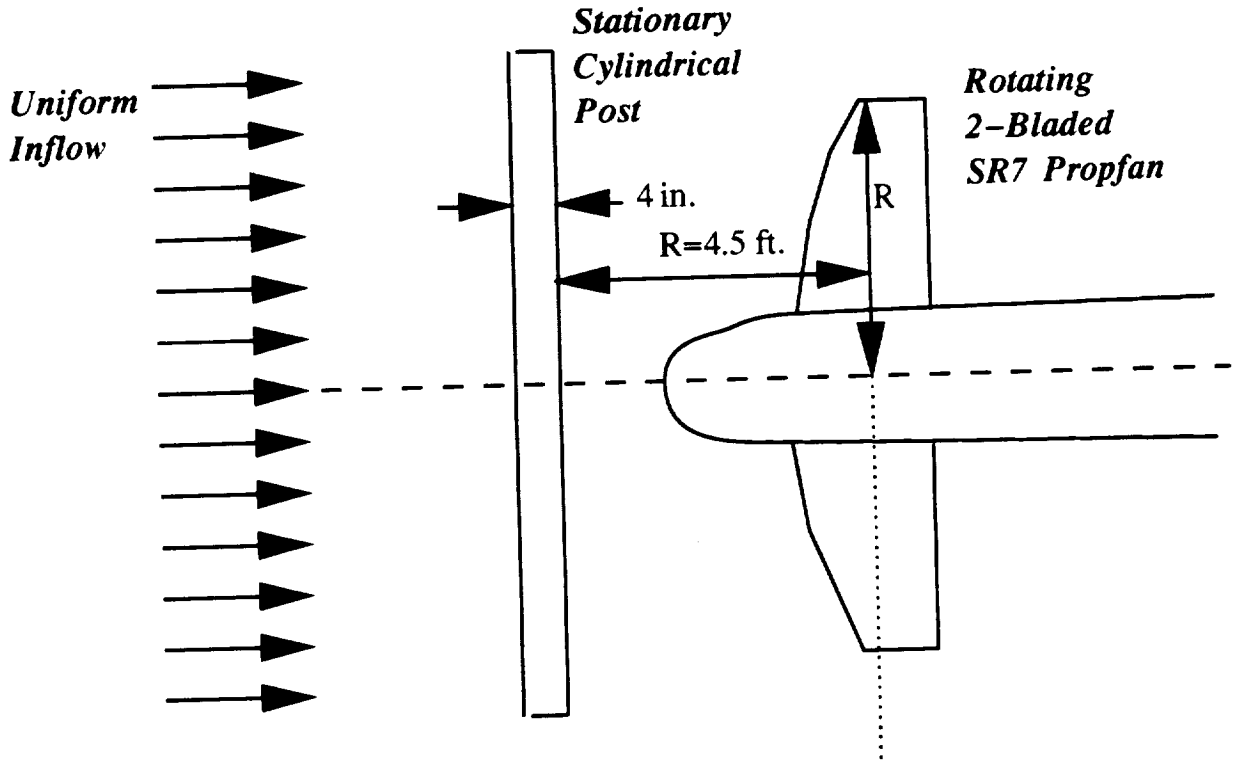

Figure 4.28: SR7 Propfan - Cylindrical Post Interaction Study Experimental Configuration

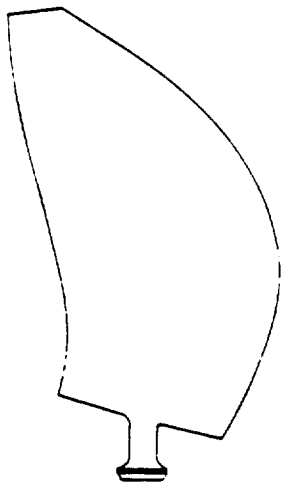

Characteristic		SR-7A
Number of blades		8
Tip sweep angle,[a] deg		41
Model diameter, cm (in.)		62.23 (24.5)
Tip speed, m/sec (ft/sec)	at 10.669 m(35 000 ft) I.S.A. altitude	243.8 (800)
Power loading, kW/m^2 (shp/ft^2)		256.85 (32)
Activity factor, AF		227
Integrated design lift coefficient, c_{Li}		0.202
Airfoils		NASA 16 and 65/CA
Ratio of nacelle maximum diameter to propeller diameter		0.35
Cruise design Mach number		0.80
Cruise design advance ratio		3.06
Cruise design power coefficient		1.45

[a]Geometric measurement from planform.

Figure 4.29: Geometric and Aerodynamic Design Parameters for the Original SR7 Propfan

case the

stationary cylindrical post is modeled as a blade row with 2 blades), the resulting mesh system requires only one mesh block per blade row. An illustration of the mesh block structure for this case is given in Figure 4.31. It should be mentioned that this mesh structure corresponds to Standard Configuration #7 described in the *ADPAC-AOACR* Computer Program Users Manual [9].

During the course of this numerical study, several mesh systems were tested with the *ADPAC-AOACR* code to predict the time-dependent static pressure on the propfan airfoil as it interacts with the wake from the cylindrical post. Grid resolution was immediately identified as a problem with most mesh systems tested. In order to adequately convect the wake from the cylinder, a large number of circumferential mesh points were required in both grid systems. This was predominantly evident in the propfan mesh block. As the wake is convected into the downstream mesh block, the circumferential spacing of the mesh typically varies dramatically based on the relative position of the profan blades as they rotate during the time-accurate solution process. Due to computational costs, it was not feasible to maintain the required circumferential spacing in the propfan mesh block required to accurately convect the wake throughout the blade rotation. The best compromise appeared to be to move the interface between the two mesh blocks as close to the propfan as possible, and to allow the stationary mesh block to convect the wake as far downstream as possible. This suggests that the influence of the wake on the propfan airfoil is only important when the airfoil and the wake are in close proximity, as the wake is effectively lost in the propfan mesh when the airfoil is rotated away from the plane of the wake.

An axisymmetric view of the final mesh system used to provide the numerical results is given in Figure 4.31. This mesh system provided a reasonable compromise between solution accuracy, and computational cost for the prediction of this complicated unsteady flow.

The time-dependent calculation was initiated from a steady state solution on the same grid using the mixing plane concept described in Section 3.2 to couple the adjacent, relatively rotating blade rows. Once the steady flow solution was reached, the time-dependent calculation was initiated using the space/time resolved interblade row coupling procedure described in Section 3.3. The solution was advanced in time

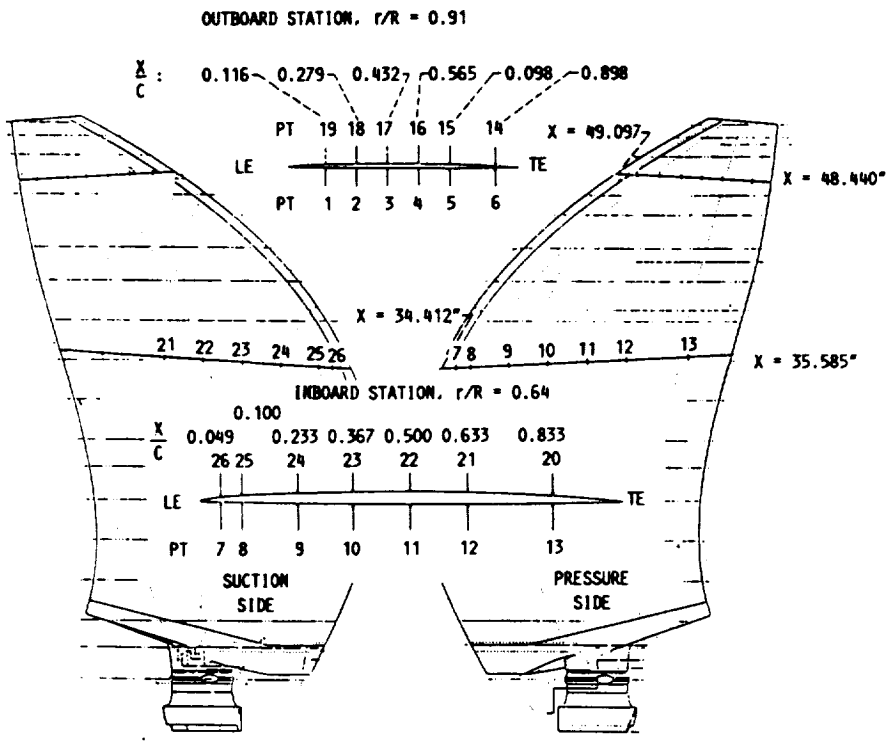

Figure 4.30: SR7 Propfan - Cylindrical Post Aerodynamic Interaction Experimental Airfoil Surface Data Locations

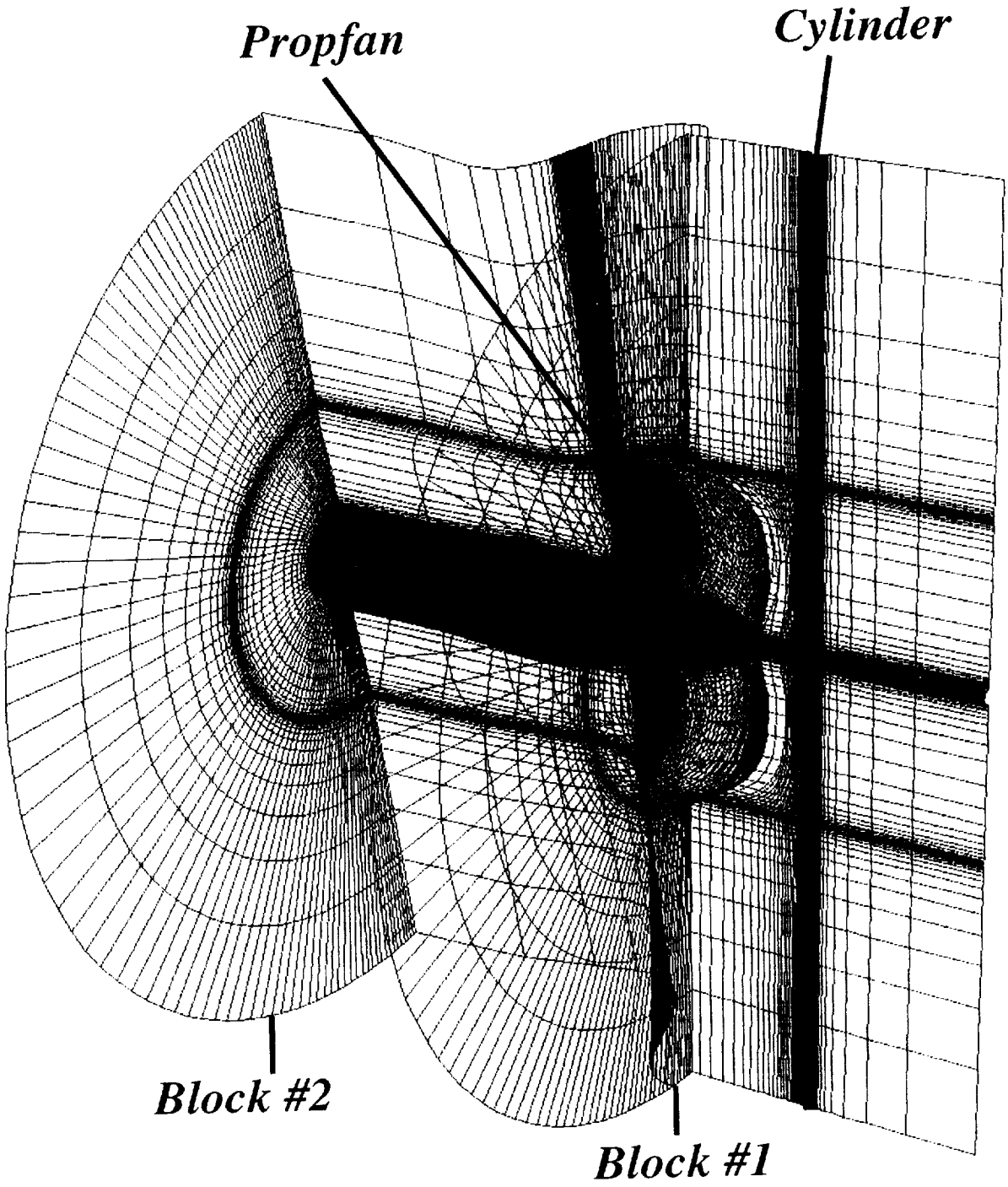

Figure 4.31: *ADPAC-AOACR* Two-Block Mesh System for SR7 Propfan - Cylindrical Post Time-Dependent Aerodynamic Interaction Analysis

for 3 complete revolutions of the propfan rotor. It was observed that for all practical purposes, a time-periodic solution had been achieved after the first revolution. This is most likely a result of the fact that the cylinder and propfan airfoil count is so low, and the airfoils actually behave as if they are isolated, rather than cascaded. The time-periodic results presented here pertain to the final revolution of the rotor.

Predicted propfan surface pressure histories given as the unsteady deviation from the steady state static pressure divided by the steady state static pressure are compared with time-resolved experimental data in Figures 4.32-4.35.

The predicted aerodynamic response is in good agreement with the experimental traces over all of the measurement locations surveyed. In most cases, the peak pressure differential resulting from the interaction between the propfan and the wake is slightly underpredicted by the *ADPAC-AOACR* code. It is also evident from the predicted time-interval over which the airfoil static pressure history is disturbed that the wake width has been overpredicted. It is believed that both of these effects could be improved by increasing the overall mesh resolution (although at the expense of increasing the overall computational cost).

An illustration of the predicted instantaneous total pressure contours at the midspan of the propfan airfoil is given in Figure 4.36. This figure clearly depicts the propfan airfoil slicing through the cylinder wake, and the resulting effects on the propfan airfoil pressure field. An interesting side note for this case is that the experimental Reynolds number for the cylinder was within the range ($50 < Re_D < 400000$) where Karman vortex streets occur. Graphical visualization of the instantaneous flow behind the cylinder at several times did not depict any vortex shedding from the cylinder. It is unlikely that the numerical grid used in this calculation is truly dense enough to accurately support any physical vortex shedding phenomena.

4.7 Model Counterrotating Propfan (Unsteady Flow)

In this section, numerical results are presented for a time-dependent calculation of the flow through the model counter rotation propeller described in Section 4.2. Steady flow predictions for this geometry based on the mixing plane concept were

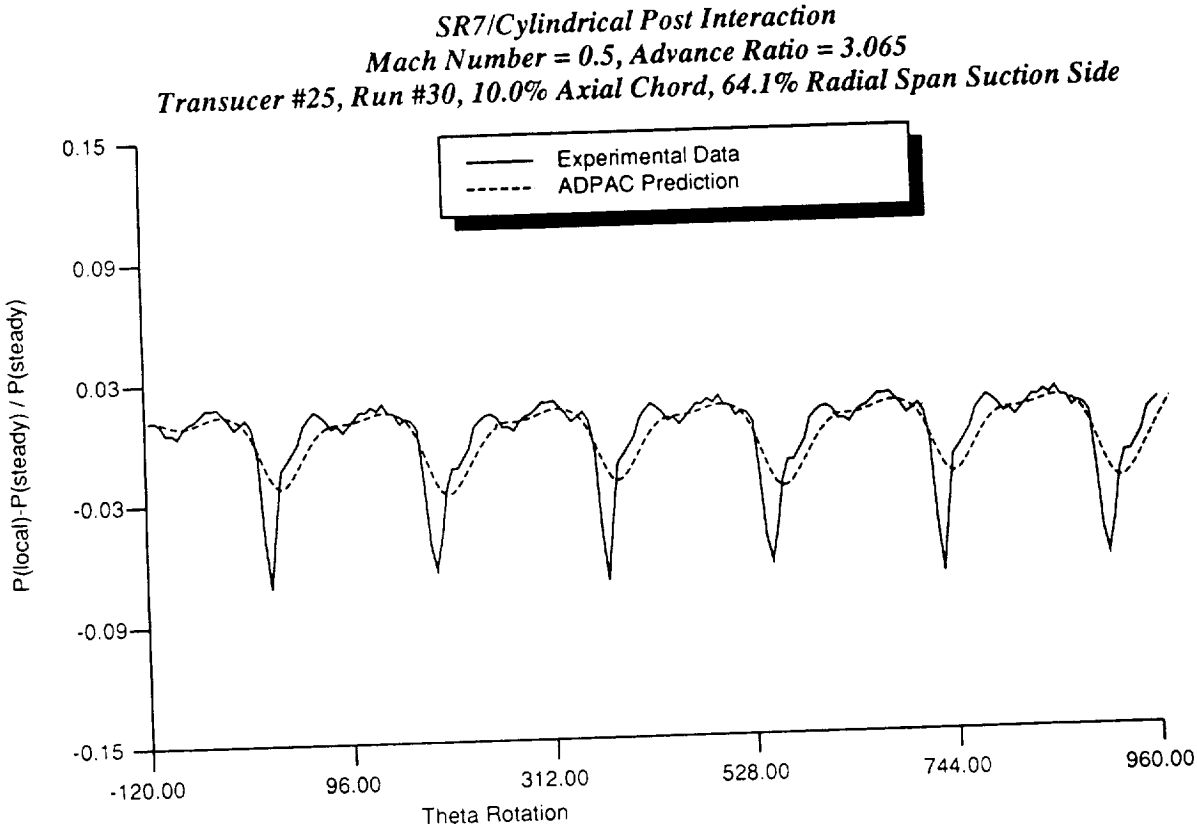

Figure 4.32: Comparison of Time-Resolved Predicted and Experimental Propfan Surface Static Pressure Histories for SR7 Propfan - Cylindrical Post Aerodynamic Interaction Study (10.0% Axial Chord, 64.1% Radial Span,Suction Side)

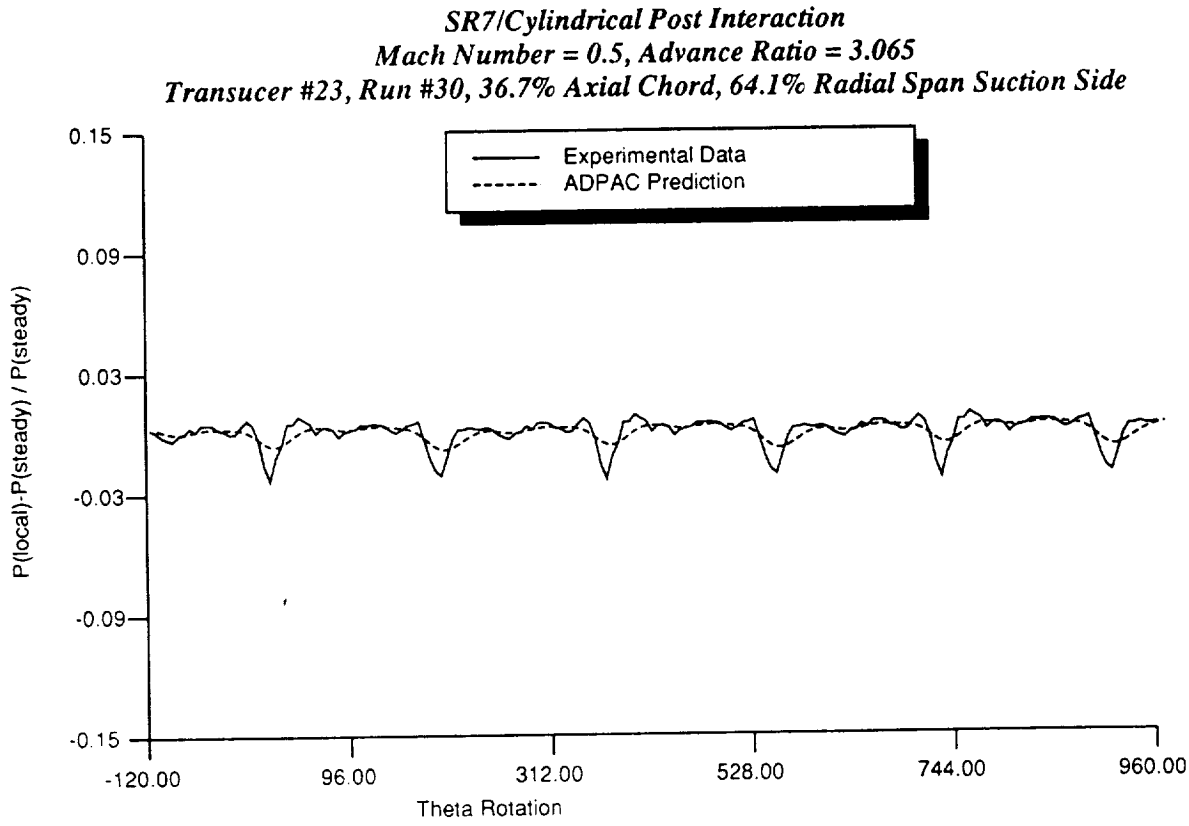

Figure 4.33: Comparison of Time-Resolved Predicted and Experimental Propfan Surface Static Pressure Histories for SR7 Propfan - Cylindrical Post Aerodynamic Interaction Study (36.7% Axial Chord, 64.1% Radial Span, Suction Side) 94

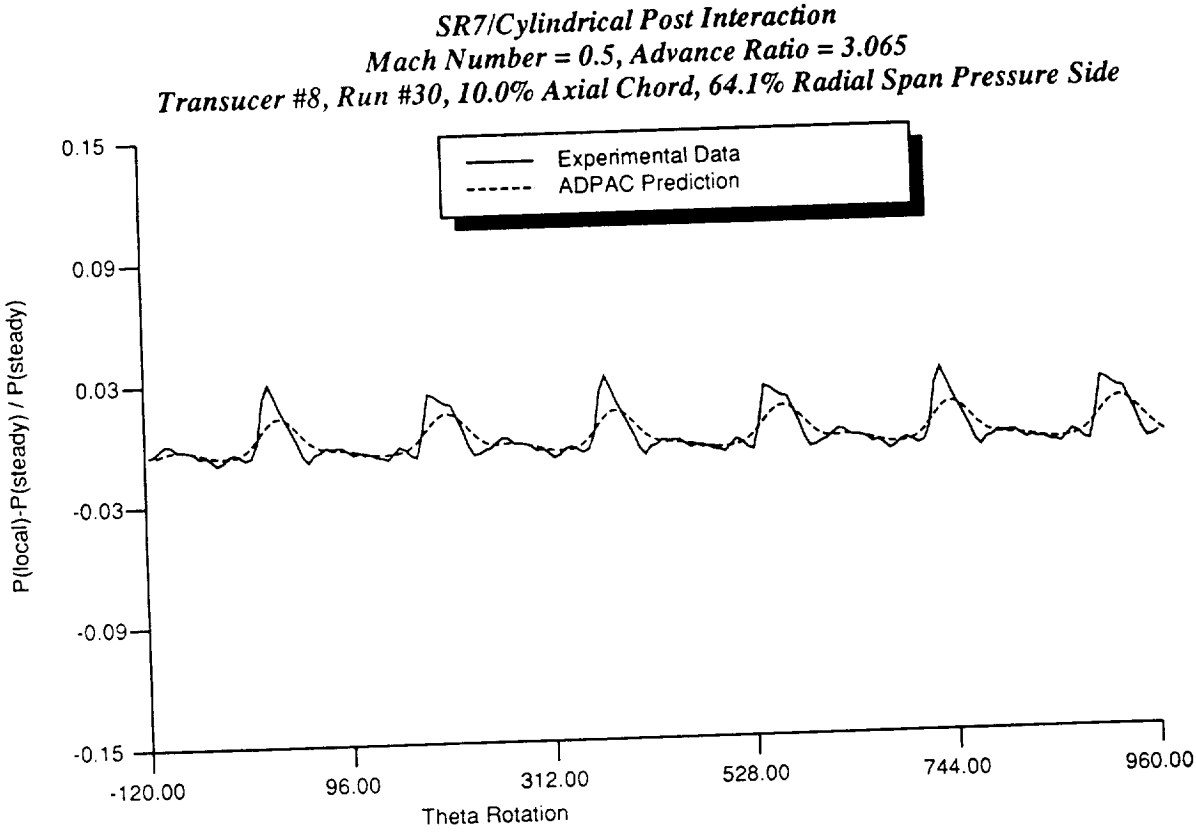

Figure 4.34: Comparison of Time-Resolved Predicted and Experimental Propfan Surface Static Pressure Histories for SR7 Propfan - Cylindrical Post Aerodynamic Interaction Study (10.0% Axial Chord, 64.1% Radial Span, Pressure Side)

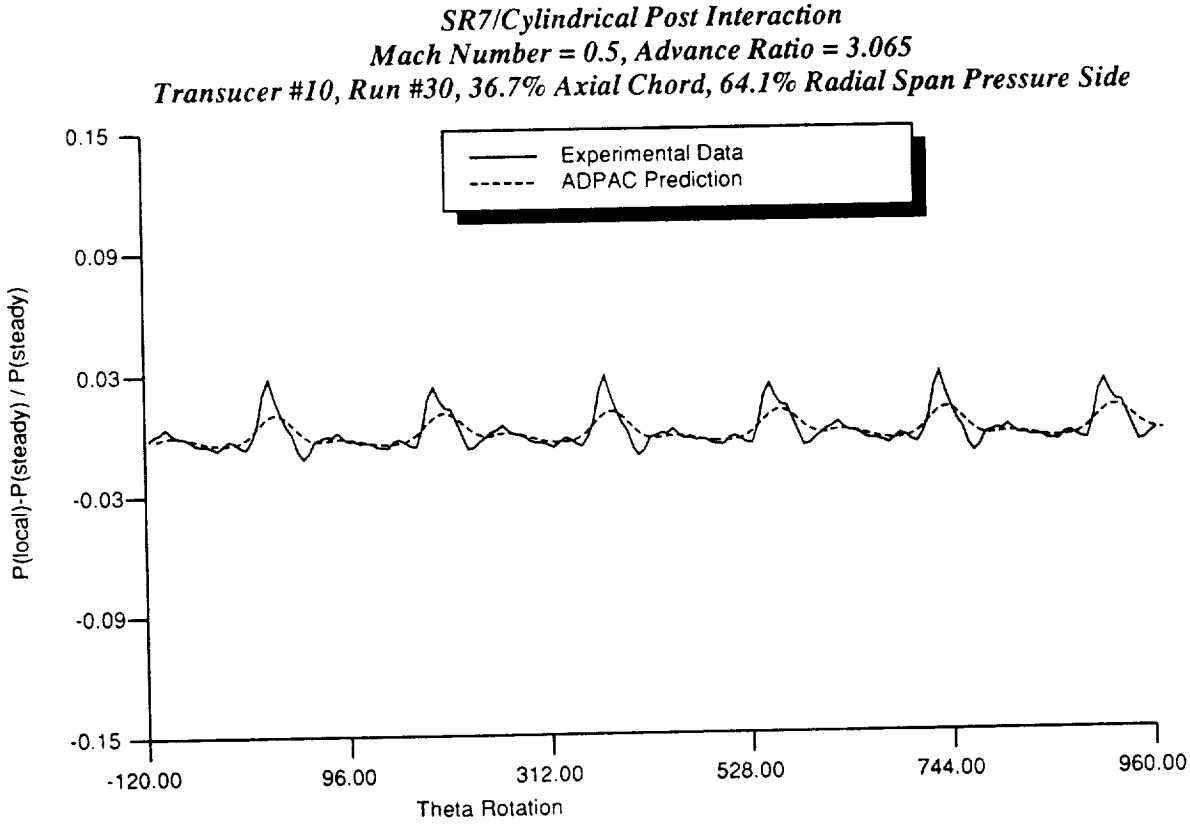

Figure 4.35: Comparison of Time-Resolved Predicted and Experimental Propfan Surface Static Pressure Histories for SR7 Propfan - Cylindrical Post Aerodynamic Interaction Study (36.7% Axial Chord, 64.1% Radial Span, Pressure Side) 96

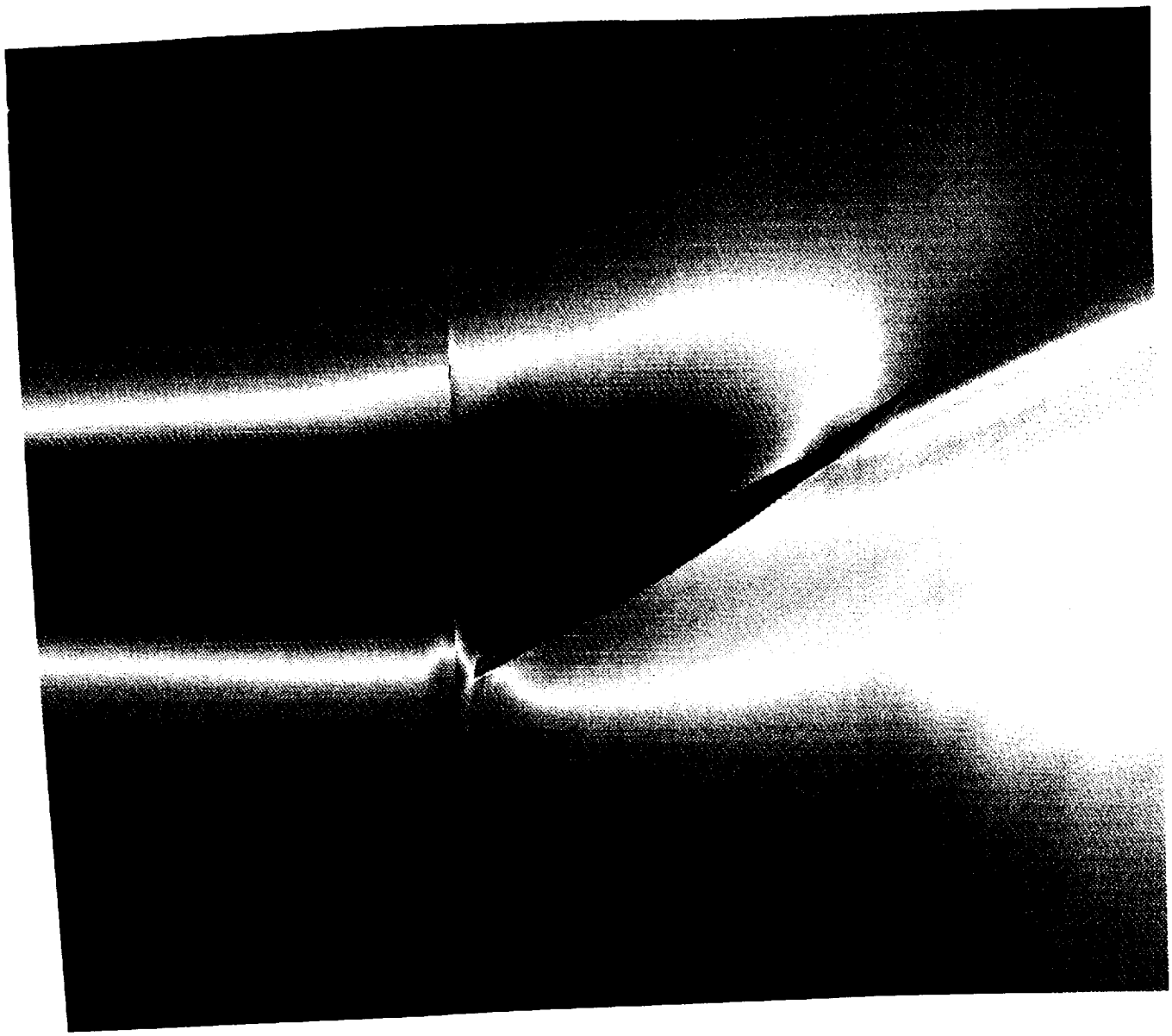

Figure 4.36: Predicted Instantaneous Propfan Airfoil Midspan Total Pressure Contours for Cylinder/Propfan Interaction Study

also described in Section 4.2. Geometric and aerodynamic design parameters for the model propeller are given in Figure 4.4. The calculations presented here were based on a cruise condition with a flight Mach number of 0.72, and advance ratio of 3.14, and forward and rearward blade setting angles of 57.4 and 60.0 degrees, respectively. This time-dependent flow calculation is the unsteady equivalent of the steady flow mixing plane calculations described in Section 4.2.

Time-dependent flow performance predictions for the CRP-X1 propfan were obtained by using the time-dependent inter-blade row interpolation concept described in Section 3.6. The grid therefore consists of two blocks (one for each blade row) as a result of the simple blade count ratio (1:1). It should be noted that this grid system corresponds to standard configuration #7 as described in the *ADPAC-AOACR* Computer Program Users Manual [9]. The grid block sizes were 65x49x33 and 57x49x33, respectively. An illustration of the mesh system is given in Figure 4.5. The time-dependent calculation was initiated from the steady flow predictions obtained using the mixing plane concept. In this case, because of the simple blade count ratio, the same grid system may be used for either calculation. Once initiated, the time dependent solution updates the data between the blade row mesh blocks based on a time-space resolved interpolation procedure to accurately maintain the interblade row aerodynamic interactions. The solution eventually becomes time-periodic, as shown in the residual history given in Figure 4.37. An illustration of the time-dependent aerodynamic interactions which occur between the counterrotating propfan airfoils is illustrated in the instantaneous midspan static pressure contour plots given in Figure 4.38. This series of instantaneous plots illustrates the relative motion between the propfan blade rows and the resulting static pressure field interactions which result from this motion over one cycle of the interaction period at the blade midspan. The interaction is obviously most intense at the point where the adjacent propfan airfoils are lined up circumferentially. The interaction appears to have a more significant effect on the downstream blade row, which is not unexpected since the downstream blade row is subject to both potential and vortical disturbances while the upstream blade row is only subject to potential disturbances.. In the absence of time-dependent experimental data, these results can only be interpreted philosophically; however, the overall indications are that the time-dependent flowfield has at least been captured

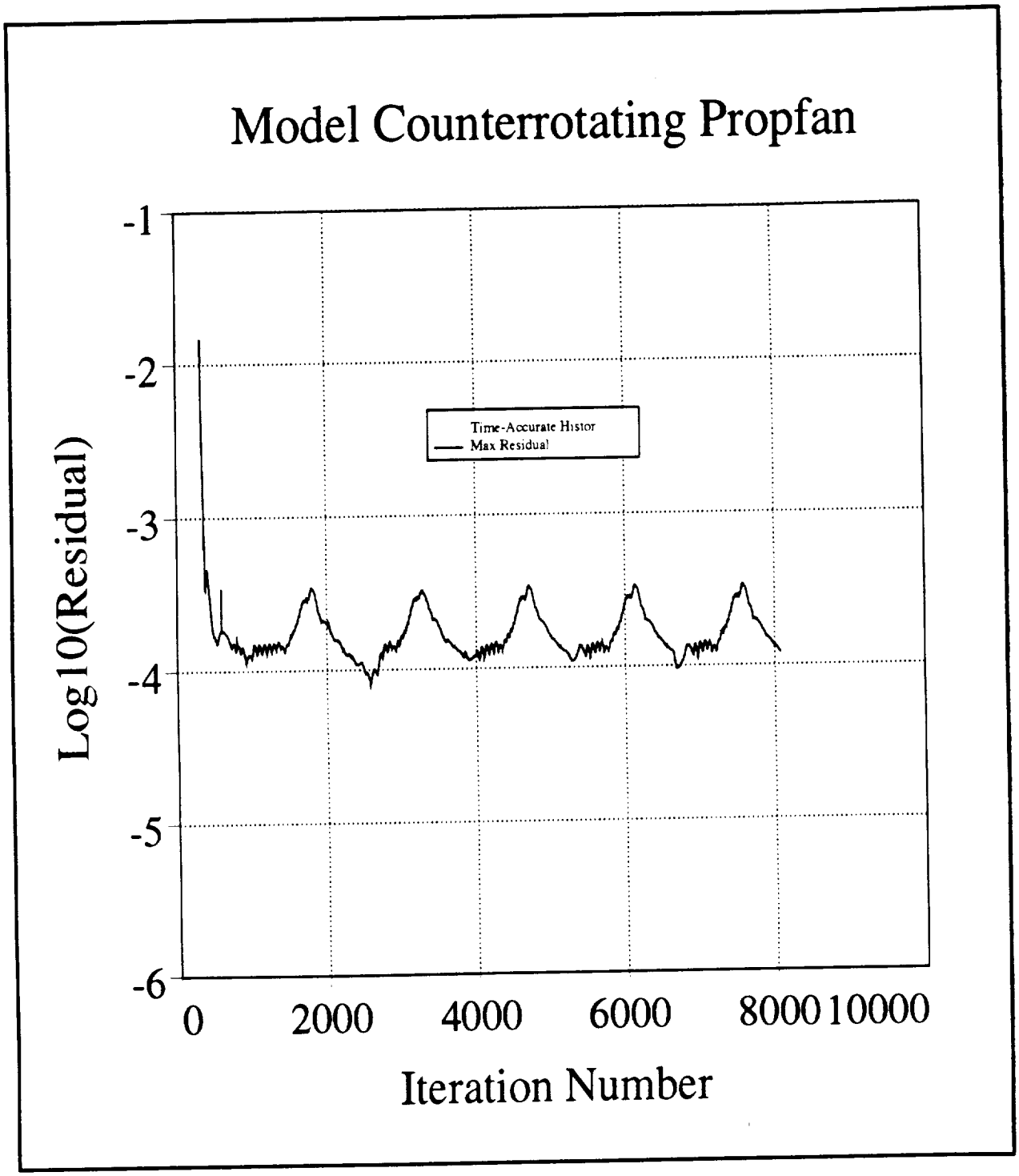

Figure 4.37: *ADPAC-AOACR* Time-Accurate Residual History for Model Counter-Rotating Propfan Aerodynamic Interaction Analysis

in a reasonable manner, and has been done relatively efficiently by taking advantage of the capabilities of the *ADPAC-AOACR* code.

4.8 GMA3007 Fan Section Distortion Study (Unsteady Flow)

The final calculation to be presented is a prediction of the unsteady flow which results from a circumferential inlet distortion in a modern turbofan engine fan section. This calculation serves the dual purpose of analyzing a complex aerodynamic phenomena associated with turbofan engine operation, as well as displaying the coupled 2-D/3-D mesh block capabilities of the *ADPAC-AOACR* code. The geometry selected for this study is the fan section of the Allison GMA3007 turbofan engine. The Allison GMA3007 is a 5:1 bypass ratio turbofan engine which produces 7,000 pounds of thrust. The fan section geometry considered consists of three blade rows including the fan rotor, bypass stator, and core stator. The flow is complicated by the presence of the core flow splitter, and the fact that there are multiple exits (bypass flow, core flow) for which proper boundary data must be specified. An outline of the GMA3007 fane section geometry is given in Figure 4.17.

The simulation selected involves a 6 per revolution circumferential distortion. The distortion is represented by a stationary total pressure deficit in the incoming flow. Each area of distortion occupies a 30 degree arc circumferentially, and is located between 60% and 100% span radially. This particular distortion pattern was chosen because the resulting mesh block structure can be simplified considerably compared to other (1,2, or 3 per revolution) distortion patterns. The radial distribution of the distortion was chosen based on experience which suggests that most fan designs are "tip critical", suggesting that distortion effects are most critical near the fan tip. The distortion pattern is illustrated graphically in Figure 4.39.

This calculation required a rather unique mesh block arrangement as shown in Figure 4.40. The fan section consists of three blade rows (fan rotor, fan bypass stator, and the core stator). The axial separation between blade rows suggest that it is possible to solve for the rotor only in this calculation; however, previous experience suggests that the presence of the downstream geometry, and particularly the core flow splitter may have some influence on the time-averaged aerodynamic loading

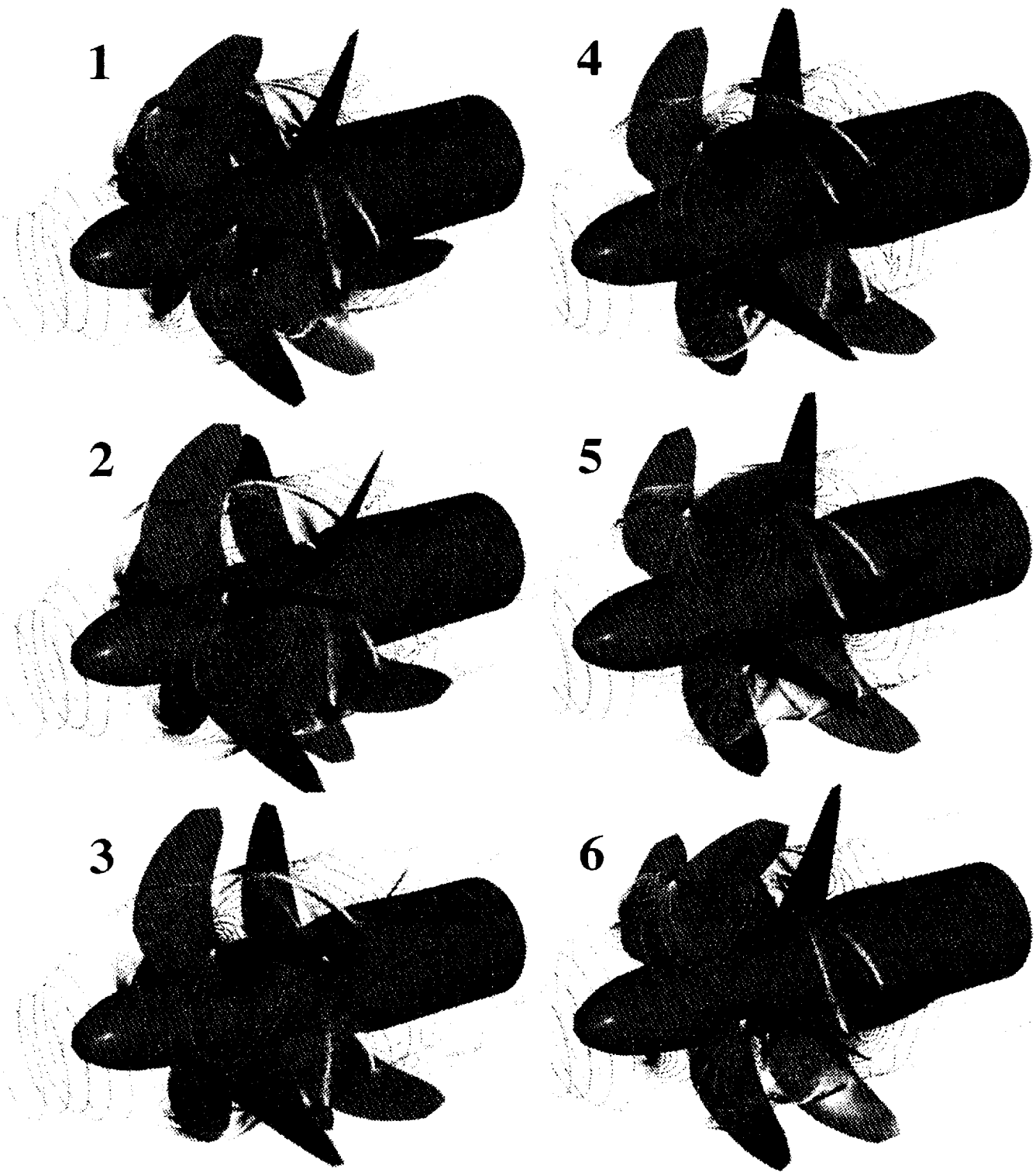

Figure 4.38: *ADPAC-AOACR* Predicted Instantaneous Static Pressure Contours at Midspan (1 cycle of time-periodic solution)

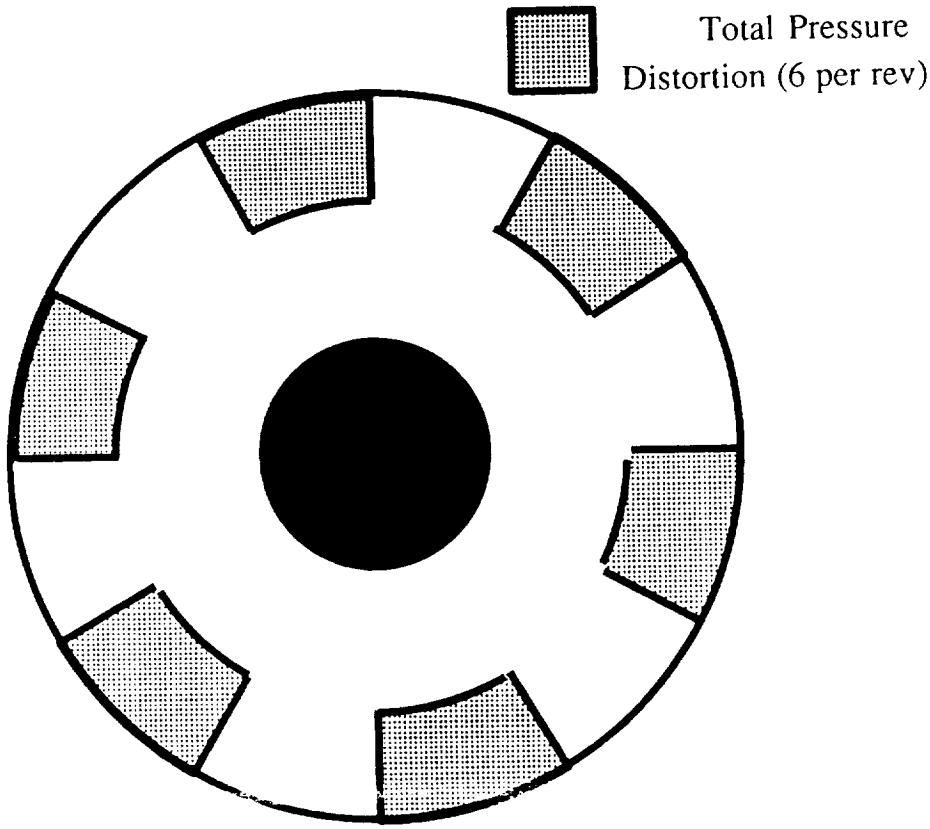

Figure 4.39: Total Pressure Deficit Pattern for Allison GMA3007 Engine Fan Section Distortion Study

of the upstream rotor. Four stationary mesh blocks located upstream of the fan rotor are utilized to impose the desired circumferential and radial distortion pattern. The distortion is defined as a nonuniform inlet boundary condition on two of the stationary mesh blocks, resulting in the distortion pattern previously described. The fan rotor is represented by a mesh system discretizing four blade passages. This is the minimum portion of the rotor which must be represented under the present distortion pattern. The use of four blade passages permits an application of periodicity across the rotor blade representation which is consistent with the imposed 6 per revolution distortion pattern. It was assumed that the bypass stator and core stator did not require more than a single blade passage representation, and therefore the bypass stator is represented by a single 3-D blade passage mesh, and the core stator is represented through a 2-D mesh system with embedded blade element blockage and body forces to simulate the axisymmetric effects of the stator. This representation was chosen to demonstrate the combined 2-D/3-D solution coupling capabilities of the *ADPAC-AOACR* code. The single passage mesh blocks for the bypass stator and the 2-D representation of the core stator are numerically coupled with the mesh blocks for the fan rotor by using a circumferential averaging procedure. Due to time constraints and computational limitations, a relatively sparse mesh was utilized in this calculation, and the results should therefore be interpreted only as a demonstration of this capability, and not conclusively representative of the truie flow.

The time-dependent calculation was initialized from a steady flow calculation utilizing the mixing plane concept between blade rows. The time-dependent calculation was performed over approximately 4 cycles of the distortion pattern, beyond which point a time-periodic solution was observed.

During the course of this calculation, the distortion pattern was observed to become less well defined with axial distance from the inlet. This phenomenon was a result of the relatively coarse mesh used in this demonstration which unrealistically smeared the distortion pattern due to numerical dissipation. As a result, the impact of the distortion on the rotating fan was minimized by the resulting smoothing of the distortion as it approached the fan. This implies that for practical calculations involving inlet distortions, a significant number of grid points must be utilized just on the basis of distortion convection alone.

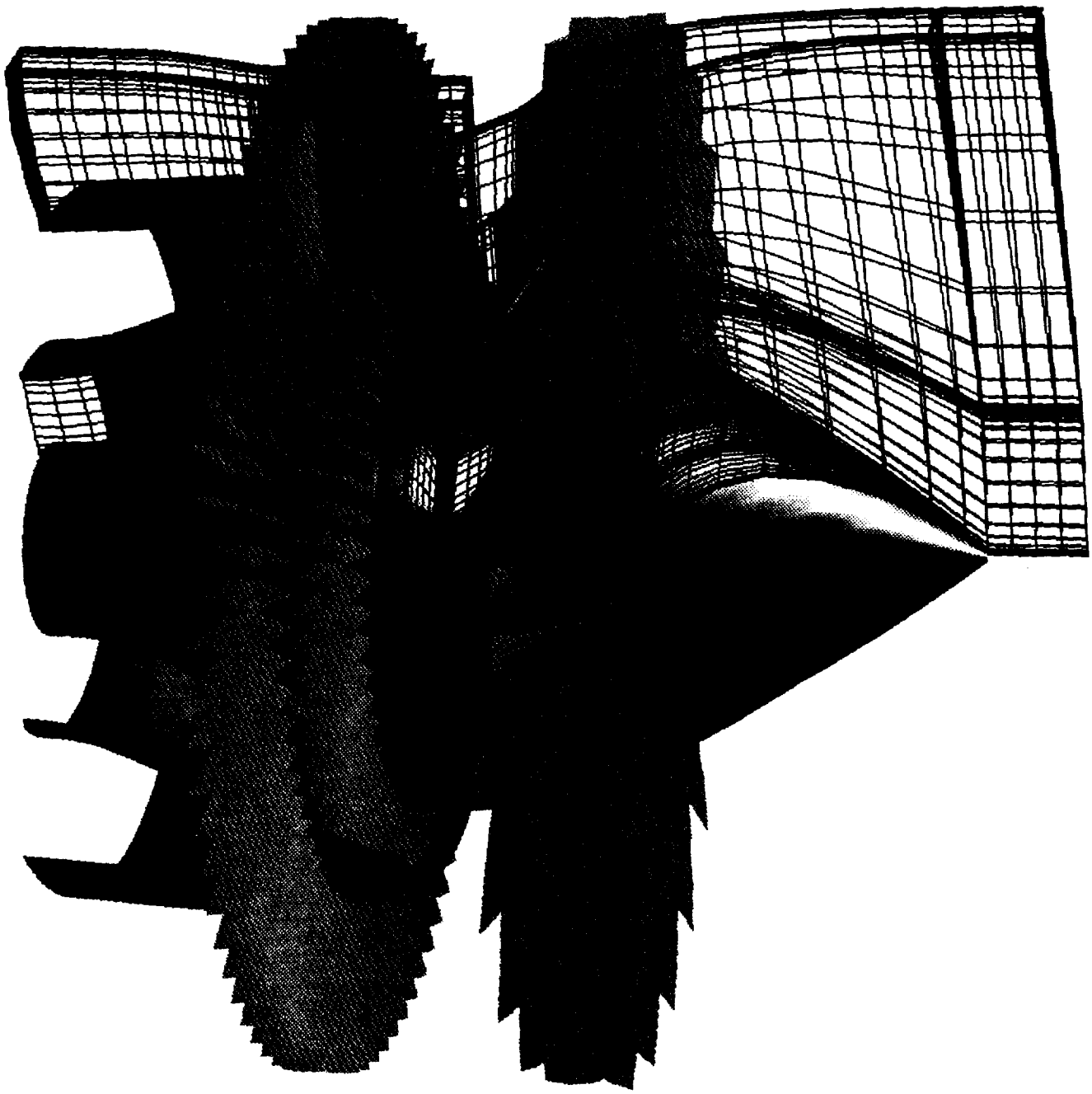

Figure 4.40: *ADPAC-AOACR* 10-Block Mesh System for Allison GMA3007 Engine Fan Section Inlet Distortion Study

An illustration of the effects of the inlet distortion on the fan rotor are displayed on the surface static pressure contour plot given in Figure 4.41. The effects of the distortion are displayed clearly in the repeating pattern near the tip of the fan rotor blades. Total pressure contours on a mesh plane downstream of the fan leading edge at approximately 30% axial chord illustrated in Figure 4.42. This figure illustrates the resulting total pressure distortion pattern after entering the rotor passage. Again, the distortion continues to become less noticable with axial distance as a result of artifical dissipation. The influence of secondary flow and aerodynamic loading on the airfoils transform the shape of the distortion, but the overall extent of the distortion appears to be relatively unchanged. Without experimental data to verify the results of the analysis, no concrete conclusions can be drawn from this analysis; however, the potential for the capability to analyze complex turbomachinery flows resulting from inlet flow distortion has been demonstrated.

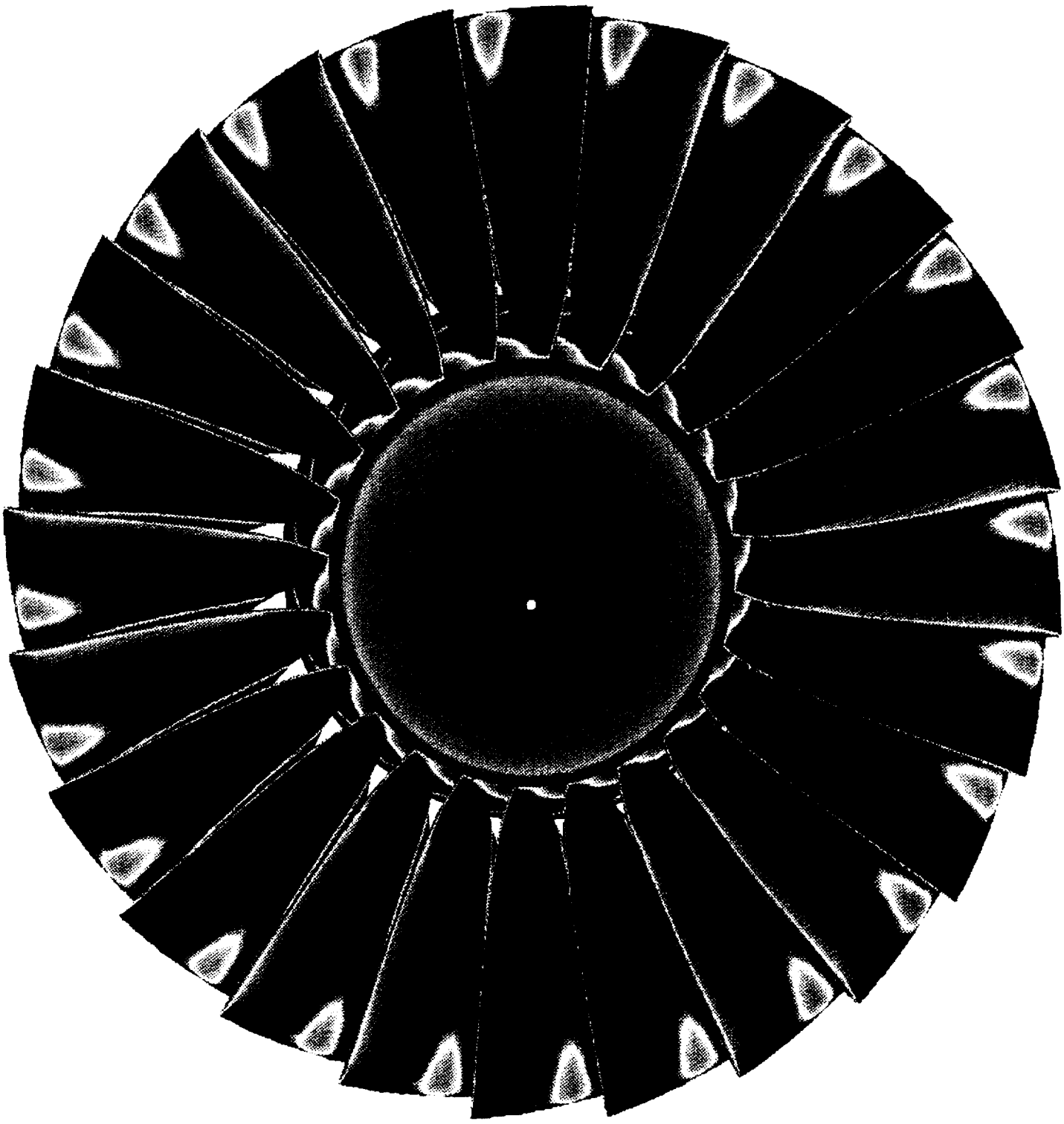

Figure 4.41: *ADPAC-AOACR* Instantaneous Predicted Rotor Surface Static Pressure Contours for GMA3007 Fan Operating Under Inlet Distortion

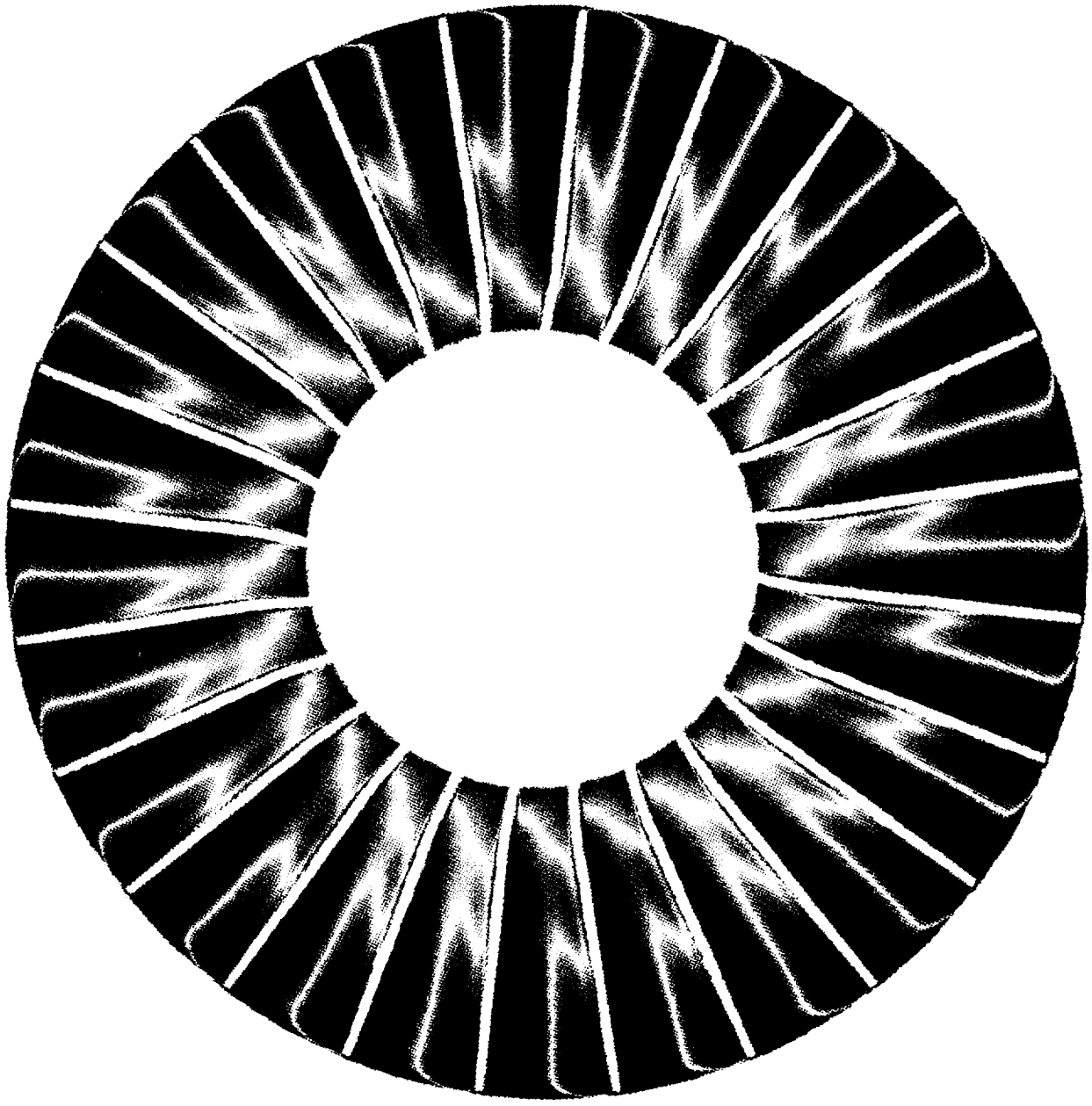

Figure 4.42: *ADPAC-AOACR* Predicted Instantaneous Total Pressure Contours at 30% Axial Chord for the GMA3007 Fan Operating Under Inlet Distortion

5. CONCLUSIONS

A time-dependent, three-dimensional Euler/Navier-Stokes aerodynamic analysis has been developed for the numerical analysis of ducted and unducted fan flowfields involving multiple blade rows. The underlying multi-block discretization scheme provides a convenient basis upon which detailed aerodynamic analyses for complicated counterrotating geometries may be performed. Multiple blade row calculations were demonstrated utilizing both the steady flow mixing plane concept and the time-resolved interpolation procedure for rotor/stator interaction calculations. Aerodynamic predictions generated from the analysis were verified through comparisons with both steady state and time-dependent experimental data. The capability of accurately simulating the time-dependent aerodynamics in an advanced turbofan engine fan section with inlet distortion has been demonstrated.

Several comments are in order concerning the various numerical techniques applied in this study. It is apparent that the algebraic turbulence model may not be well suited for the complex vortical flows which can occur for modern turbomachinery blade designs. Future efforts may benefit from more detailed turbulence models developed for complex 3-D flows. The time-accurate implicit residual smoothing algorithm is also a known source of error for unsteady flow predictions. Although these errors are suspected to be local in nature, additional studies dedicated to understanding the impact and limitations of this algorithm may be warranted. The overall accuracy of the analysis can be swayed by additional factors, including the unknown deflected shape of the propfan blade, errors introduced through poor grid resolution, turbulence modeling, and artificial dissipation. In spite of the known algorithmic deficiencies, the analysis has successfully predicted several complex time-dependent flows with interacting geometries, and has demonstrated good agreement with available experimental data.

REFERENCES

[1] Weber, K. F., and Delaney, R. A., "Viscous Analysis of Three-Dimensional Turbomachinery Flows on Body Conforming Grids Using an Implicit Solver", ASME Paper 91-GT-205, 1991.

[2] Chima, R. V., "Inviscid and Viscous Flows in Cascades with an Explicit Multiple-Grid Algorithm", AIAA Journal Vol. 23, pp. 1156-1563, 1985.

[3] Wainusky, H. S., and Vaczy, C. M., "Aerodynamic Performance of a Counter Rotating Prop-Fan", AIAA Paper 86-1550, 1986.

[4] Rai, M. M., "Unsteady Three-Dimensional Navier-Stokes Simulation of Rotor-Stator Interactions", AIAA Paper 87-2058, 1987. 1985.

[5] Adamczyk, J. J., "Model Equations for Simulating Flows in Multistage Turbomachinery", ASME Paper 85-GT-226.

[6] Goyal, R. K., and Dawes, W. N.,"A Comparison of the Measured and Predicted Flowfield in a Modern Fan-Bypass Configuration", ASME Paper 92-GT-298, 1992.

[7] Hall, E. J. and Delaney, R. A., "Investigation of Advanced Counterrotation Blade Configuration Concepts for High Speed Turboprop Systems: Task II - Unsteady Ducted Propfan Analysis - Final Report", NASA CR 187106, NASA Contract NAS3-25270, 1992.

[8] Crook, A. J. and Delaney, R. A., "Investigation of Advanced Counterrotation Blade Configuration Concepts for High Speed Turboprop Systems: Task IV - Advanced Fan Section Analysis, Final Report", NASA CR 187128, NASA Contract NAS3-25270, 1992.

[9] Hall, E. J. and Delaney, R. A., "Investigation of Advanced Counterrotation Blade Configuration Concepts for High Speed Turboprop Systems: Task V - Counterrotation Ducted Propfan Analysis, Computer Program Users Manual", NASA CR 187125, NASA Contract NAS3-25270, 1992.

[10] Martinelli, L., "Calculation of Viscous Flows with a Multigrid Method", Ph. D. Dissertation, MAE Department, Princeton University, 1987.

[11] Barton, J. M., Yamamoto, O., and Bober, L. J., "Euler Analysis of Transonic Propeller Flows," *AIAA Journal*, Vol. 3, June 1987, pp. 277-282.

[12] Saxer, A., "A Numerical Analysis of 3-D Inviscid Stator/Rotor Interaction Using Non-Reflecting Boundary Conditions", MIT Gas Turbine Laboratory Report #209, 1992.

[13] Janus, M., Personal communication, June, 1992.

[14] Usab, W. J., Lee, A. K., and Sullivan, J. P., "A Comparison of Numerical Simulation and Experimental Measurements of Flow through Propellers," AIAA Paper 88-0367, 1988.

[15] Saito, S., Kobayashi, H., Nakamura, Y., and Matsuo, Y., "Predicted Flow Field Around the Advanced Propeller at Take-Off," AIAA Paper 88-3151, 1988.

[16] Matsuo, Y., Arakawa, C., Saito, S., and Kobayashi, H., "Navier-Stokes Computations for Flowfield of an Advanced Turboprop," AIAA Paper 88-3094, 1988.

[17] Kobayawa, M., and Hatano, I., "Flow Field around a Propeller by Navier-Stokes Equation Analysis," AIAA Paper 88-3150, 1988.

[18] Celestina, M. L., Mulac, R. A., and Adamczyk, J. J., "A Numerical Simulation of the Inviscid Flow Through a Counterrotating Propeller," ASME Paper 86-GT-136, 1986.

[19] Whitfield, D. L., Swafford, T. W., Janus, J. M., Mulac, R. A., and Belk, D. M., "Three-Dimensional Unsteady Euler Solutions for Propfans and Counter-Rotating Propfans in Transonic Flow," AIAA Paper 87-1197, 1987.

[20] Hall, E. J., and Delaney, R. A., "3D Euler Analysis of Ducted Propfan Flowfields", AIAA Paper 90-3034-CP, 1990.

[21] Hall, E. J., Delaney, R. A., and Bettner, J. L., "Investigation of Advanced Counterrotation Blade Configuration Concepts for High Speed Turboprop Systems: Task I - Ducted Propfan Analysis", NASA CR 185217, NASA Contract NAS3-25270, 1990.

[22] Williams, M. H., Cho, J., and Dalton, W. N., "Unsteady Aerodynamic Analysis of Ducted Fans," (to appear in the *AIAA Journal of Propulsion and Power*).

[23] Nallasamy, M., and Groeneweg, J. F., "Unsteady Euler Analysis of the Flow Field of a Propfan at an Angle of Attack", AIAA Paper 90-0339, 1990.

[24] Whipple, D., "BDX-Binary Data Exchange Preliminary Information", NASA-Lewis Research Center, 1989.

[25] Walatka, P. P., and Buning, P. G., "PLOT3D User's Manual,", rough draft for NASA TM, 1988.

[26] Plessel, Todd, "SURF User's Guide,", NASA Ames Research Center, 1988.

[27] Walatka, P. P., and Buning, P. G., "FAST", NASA Ames Research Center, 1990.

[28] Mulac, R. A., "A Multistage Mesh Generator for Solving the Average-Passage Equation System," NASA CR 179539, 1988.

[29] Adamczyk, J. J., Celestina, M. L., Beach, T. A., and Barnett, M., "Simulation of Three-Dimensional Viscous Flow Within a Multistage Turbine," ASME Paper 89-GT-152, 1989.

[30] Brackbill, J. B., and Saltzman, J. S., "Adaptive Zoning for Singular Problems in Two Dimensions," *Journal of Computational Physics*, 46, 342-368, 1982.

[31] Thompson, J. F., "Elliptic Grid Generation," *Numerical Grid Generation* (Edited by Joe Thompson), Elsevier Science Publishing Co., 1982.

[32] Anderson, D. A., Tannehill, J. C., and Pletcher, R. H. , "Computational Fluid Mechanics and Heat Transfer", McGraw-Hill, New York, New York, 1984.

[33] Hung, C. M., and Kordulla, W., "A Time-Split Finite Volume Algorithm for Three-Dimensional Flow-Field Simulation," AIAA Paper 83-1957, 1983.

[34] Baldwin, B. S., and Lomax, H., "Thin-Layer Approximation and Algebraic Model for Separated Turbulent FLows", AIAA Paper 78-257, 1978.

[35] Jameson, A., Schmidt, W., and Turkel, E., "Numerical Solutions of the Euler Equations by Finite Volume Methods Using Runge-Kutta Time-Stepping Schemes," AIAA Paper 81-1259, 1981.

[36] Radespiel, R., Rossow, C., and Swanson, R. C., "Efficient Cell Vertex Multigrid Scheme for the Three-Dimensional Navier-Stokes Equations", AIAA Journal, Vol. 28, No. 8, pp. 1464-1472, 1990.

[37] Hollanders, H., Lerat, A., and Peyret, R., "Three-Dimensional Calculation of Transonic Viscous Flows by an Implicit Method," *AIAA Journal*, 23, pp. 1670-1678, 1985.

[38] Jorgensen, P. C. E., and Chima, R. V., "An Unconditionally Stable Runge-Kutta Method for Unsteady Flows," NASA TM 101347, 1989.

[39] Rao, K. V., and Delaney, R. A., 1990, "Investigation of Unsteady Flow Through a Transonic Turbine Stage: Part I- Analysis", AIAA Paper 90-2408.

[40] Bushnell, P., "Measurement of the Steady Surface Pressure on a Single Rotation Large Scale Advanced Prop-Fan Blade at Mach Numbers from 0.03 to 0.78," NASA CR 182124, 1988.

[41] Bushnell, P., Gruber, M., and Parzych, D., "Measurement of Unsteady Blade Surface Pressure on a Single Rotation Large Scale Advanced Prop-Fan with Angular and Wake Inflow at Mach Numbers from 0.02 to 0.70", NASA CR-182123, NASA Contract NAS3-23051, 1988.

[42] Steffen, F. W., "Cruise Performance of an Isolated 1.15 Pressure Ratio Turbofan Propulsion Simulator at Mach Numbers from 0.6 to 0.85," NASA TM X-3064, 1974.

[43] Wesoky, H. L., Abbott, J. M., Albers, J. A., and Dietrich, D. A., "Low-Speed Wind Tunnel Tests of a 50.8 Centimeter (20-in.) 1.15 Pressure Ratio Fan Engine Model," NASA TM X-3062, 1974.

[44] Smith, S. M., "Discrete Frequency Sound Generation in Axial Flow Turbomachines", University of Cambridge, Department of Engineering Report CUED/A-Turbo/TR 29, 1971.

[45] Huff, D. L., "Pressure Wave Propagation Studies for for Oscillating Cascades", AIAA Paper 92-0145, 1992.

[46] Wesoky, F. L., and Steffen, F. W., "Wind Tunnel Tests of a 20 in. Diameter 1.15 Pressure Ratio Fan Engine Model," NASA TM X-71445, 1973.

[47] Osborn, W. M., and Steinke, R. J., "Performance of a 1.15 Pressure-Ratio Axial-Flow Fan Stage with a Blade Tip Solidity of 0.5," NASA TM X-3052, 1974.

APPENDIX A. *ADPAC* DISTRIBUTION LIST

ADPAC DISTRIBUTION LIST

NASA Contract NAS3-25270
Task Order #2
User's Manual CR-187125
Final Report CR-187126

GOVERNMENT AGENCIES:

NASA Headquarters
600 Independence Avenue, SW
Washington, DC 20546

Attn: RJ/C. C. Rosen
RP/S. Wander
RP/J. R. Facey

NASA Lewis Research Center
21000 Brookpark Road
Cleveland, OH 44135

Attn:	J. J. Adamczyk	M.S. 5-9	(2 copies)
	C. L. Ball	M.S. 86-1	
	L. J. Bober	M.S. 77-6	
	D. R. Boldman	M.S. 86-7	
	B. Clark	M.S. 77-6	
	R. W. Claus	M.S. 142-5	
	J. H. Dittmar	M.S. 77-6	
	J. F. Groeneweg	M.S. 77-6	(2 copies)
	C. E. Hughes	M.S. 77-6	
	R. J. Jeracki	M.S. 77-6	
	C. M. Kim	M.S. 77-6	
	J. Lytle	M.S. AAC-1	

A. J. Mahajan	M.S. 23-3	
C. J. Miller	M.S. 77-6	(15 copies)
D. P. Miller	M.S. 77-6	
R. D. Moore	M.S. 77-6	
L. D. Nichols	M.S. 142-5	
C. W. Putt	M.S. 142-2	(2 copies)
D. R. Reddy	M.S. 5-11	
T. S. Reddy	M.S. 23-3	
R. Srivastava	M.S. 23-3	
G. L. Stefko	M.S. 23-3	
R. P. Woodward	M.S. 77-6	
J. A. Ziemianski	M.S. 86-1	
Report Control Office	M.S. 60-1	(4 copies)
Tech. Utilization Office	M.S. 7-3	
AFSC Liaison Office	M.S. 501-3	

NASA Ames Research Center
Moffett Field, CA 94035

Attn:	Library	M.S. 202-3

NASA Langley Research Center
Hampton, VA 23665

Attn:	F. Farassat	M.S. 461
	M. H. Dunn	M.S. 904
	Library	M.S. 185

NASA Scientific and Technical Information Facility
P.O. Box 8757
BWI Airport, MD 21240

Attn: Accession Dept. (6 copies and the FF427 form)

Sverdrup Technology, Inc.
2001 Aerospace Parkway
Brookpark, OH 44142

Attn:	J. Bridges	M.S. 77-6
	E. Envia	SVR-3
	R. M. Nallasamy	SVR-3
	S. M. Ramachandra	SVR-3
	O. Yamamoto	SVR-3

ENGINE MANUFACTURERS

Allison Gas Turbine Division, GMC Corp.
P.O. Box 420
Indianapolis, IN 46206-0420

Attn:	P. Mail Stop T-144	
	R. F. Alverson	Mail Stop T-14A
	D. W. Burns	Mail Stop T-14A
	R. A. Delaney	Mail Stop T-14A
	J. R. Rathman	Mail Stop T-14A
	D. J. Helton	Mail Stop T-14A
	A. J. Crook	Mail Stop T-14A
	K. P. Nardini	Mail Stop T-14A

General Electric Company
Aircraft Engine Group
1 Neumann Way
Evendale, OH 45215

Attn:	P. Gliebe	Mail Drop A-304
	C. Lenhardt	Mail Drop A-330
	M. Majjigi	Mail Drop A-319
	M. Pearson	Mail Drop A-317
	L. Smith	Mail Drop H-4
	C. Whitfield	Mail Drop A-304

Hamilton Standard Division - UTC
Windsor Locks, CT 06096

Attn:	D. B. Hanson	M.S. 1A-3-6
	F. B. Metzger	M.S. 1A-3-6

Pratt & Whitney Aircraft - UTC
Commercial Products Division
400 Main Street
East Hartford, CT 06108

Attn:	D. Hopwood	M.S. 162-07 (3 copies)
	D. Mathews	M.S. 165-11
	W. Lord	M.S. 169-23
	T. Wynosky	M.S. 169-23

United Technologies Corporation Research Center
Silver Lane
E. Hartford, CT 06108

Attn:	M. Barnett	M.S. 20
	R. Davis	M.S. 20
	D. Dorney	M.S. 20

AIRFRAME MANUFACTURERS

Boeing Commercial Airplane Company (BCAC)
P.O. Box 3707
Seattle, WA 98124-2207

Attn:	B. W. Farquhar	M.S. 0L-22
	W-H. Jou	M.S. 7H-96
	R. Cuthbertson	M.S. 79-84

Douglas Aircraft Company Division
McDonnell Douglas Corporation
3855 Lakewood Blvd.
Long Beach, CA 90846

Attn:	M. Joshi	M.S. 36-60
	F. Lynch	M.S. 36-60
	G. Page	M.S. 35-86
	W. Siegele	M.S. 202-15

General Dynamics Convair
P.O. Box 80844
San Diego, CA 92138

Attn:	B. Bergman	M.Z. 36-1240
	S. Strande	M.Z. 55-6950
	K. Taylor	M.Z. 54-6890

UNIVERSITIES

Georgia Institute of Technology
School of Aerospace Engineering
Atlanta, GA 30332-0800

Attn: Dr. L. N. Sankar

Lockheed-California Company
P.O. Box 551
Burbank, CA 91520

Attn: Library

Ohio State University
Department of Aeronautical
and Astronautical Engineering
Columbus, OH 43220

Attn: Prof. G. M. Gregorek

Pennsylvania State University
Department of Aerospace Engineering
233 Hammond Building
University Park, PA 16802

Attn: Dr. B. Lakshminarayana

Purdue University
School of Aeronautics and Astronautics
W. Lafayette, IN 47907

Attn: Dr. J. P. Sullivan
Dr. M. Williams

Purdue University
School of Mechanical Engineering
W. Lafayette, IN 47907

Attn: Dr. S. Fleeter

Rohr Industries, Inc.
P.O. Box 878
Chula Vista, CA 92012-0878

Attn: Library

Texas A&M University
Aerospace Engineering Department
College Station, TX 77843-3141

Attn: Dr. K. D. Korkan

University of Arizona
Aerospace and Mechanical Engineering Department
Aero Building #16
Tucson, AZ 85721

Attn: Dr. E. J. Kerschen

University of Missouri-Rolla
Mechanical Engineering Department
Rolla, MO 65401-0249

Attn: Dr. Walter Eversman

Mississippi State University
Department of Aerospace Engineering
P.O. Box A
Mississippi State, MS 39762

Attn: Dr. D. Whitfield
Dr. M. Janus

NASA
National Aeronautics and Space Administration

Report Documentation Page

1. Report No.	2. Government Accession No.	3. Recipient's Catalog No.
NASA CR 187126		

4. Title and Subtitle	5. Report Date
Investigation of Advanced Counterrotating Blade Configuration Concepts for High SPeed Turboprop Systems, Task 5 - Unsteady Counterrotation Ducted Propfan Analysis, Final Report	January 1993
	6. Performing Organization Code
7. Author(s)	8. Performing Organization Report No.
Edward J. Hall and Robert A. Delaney	
	10. Work Unit No. 535-03-10
9. Performing Organization Name and Address	11. Contract or Grant No.
Allison Gas Turbine Division General Motors Corporation P.O. Box 420, Speed Code T14A Indianapolis, IN 46206-0420	NAS3-25270
	13. Type of Report and Period Covered
12. Sponsoring Agency Name and Address	Contract Report, Final
National Aeronautics and Space Administration Lewis Research Center 21000 Brookpark Road Cleveland, OH 44135-3191	14. Sponsoring Agency Code

15. Supplementary Notes

Prepared in cooperation with NASA Project Manager, Christopher J. Miller, NASA Lewis Research Center, Cleveland, OH

16. Abstract The primary objective of this study was the development of a time-marching three-dimensional Euler/Navier-Stokes aerodynamic analysis to predict steady and unsteady compressible transonic flows about ducted and unducted propfan propulsion systems employing multiple blade rows. The computer codes resulting from this study are referred to as ADPAC-AOACR (Advanced Ducted Propfan Analysis Codes-Angle of Attack Coupled Row).

This document is the Final Report describing the theoretical basis and analytical results from the ADPAC-AOACR codes developed under Task 5 of NASA Contract NAS3-25270, Unsteady Counterrotating Ducted Propfan Analysis.

The ADPAC-AOACR program is based on a flexible multiple blocked grid discretization scheme permitting coupled 2-D/3-D mesh block solutions with application to a wide variety of geometries. For convenience, several standard mesh block structures are described for turbomachinery applications. Aerodynamic calculations are based on a four-stage Runge-Kutta time-marching finite volume solution technique with added numerical dissipation. Steady flow predictions are accelerated by a multigrid procedure. Numerical calculations are compared with experimental data for several test cases to demonstrate the utility of this approach for predicting the aerodynamics of modern turbomachinery configurations employing multiple blade rows.

17. Key Words (Suggested by Author(s))		18. Distribution Statement
Navier-Stokes	Turbomachinery	Unclassified-Unlimited
Fan	Multiple Block	
Ducted	ADPAC	

19. Security Classif. (of this report)	20. Security Classif. (of this page)	21. No. of pages	22. Price
Unclassified	Unclassified		A06

NASA FORM 1626 OCT 86